

AD _____

Award Number: DAMD17-99-1-9007

TITLE: Combining Clinical, Sonographic, and Elastigraphic
Features to Improve the Detection of Prostate Cancer

PRINCIPAL INVESTIGATOR: Brian Garra, M.D.

CONTRACTING ORGANIZATION: The University of Vermont and State
Agricultural College
Burlington, Vermont 05401

REPORT DATE: December 2001

TYPE OF REPORT: Annual

PREPARED FOR: U.S. Army Medical Research and Materiel Command
Fort Detrick, Maryland 21702-5012

DISTRIBUTION STATEMENT: Approved for Public Release;
Distribution Unlimited

The views, opinions and/or findings contained in this report are
those of the author(s) and should not be construed as an official
Department of the Army position, policy or decision unless so
designated by other documentation.

20020913 050

REPORT DOCUMENTATION PAGEForm Approved
OMB No. 074-0188

Public reporting burden for this collection of information is estimated to average 1 hour per response, including the time for reviewing instructions, searching existing data sources, gathering and maintaining the data needed, and completing and reviewing this collection of information. Send comments regarding this burden estimate or any other aspect of this collection of information, including suggestions for reducing this burden to Washington Headquarters Services, Directorate for Information Operations and Reports, 1215 Jefferson Davis Highway, Suite 1204, Arlington, VA 22202-4302, and to the Office of Management and Budget, Paperwork Reduction Project (0704-0188), Washington, DC 20503

1. AGENCY USE ONLY (Leave blank)**2. REPORT DATE**

December 2001

3. REPORT TYPE AND DATES COVERED

Annual (16 Nov 00 - 15 Nov 01)

4. TITLE AND SUBTITLECombining Clinical, Sonographic, and Elastographic
Features to Improve the Detection of Prostate Cancer**5. FUNDING NUMBERS**

DAMD17-99-1-9007

6. AUTHOR(S)

Brian Garra, M.D.

7. PERFORMING ORGANIZATION NAME(S) AND ADDRESS(ES)The University of Vermont and State Agricultural College
Burlington, Vermont 05401

E-Mail: bgarra@zoo.uvm.edu

**8. PERFORMING ORGANIZATION
REPORT NUMBER****9. SPONSORING / MONITORING AGENCY NAME(S) AND ADDRESS(ES)**U.S. Army Medical Research and Materiel Command
Fort Detrick, Maryland 21702-5012**10. SPONSORING / MONITORING
AGENCY REPORT NUMBER****11. SUPPLEMENTARY NOTES****12a. DISTRIBUTION / AVAILABILITY STATEMENT**

Approved for Public Release; Distribution Unlimited

12b. DISTRIBUTION CODE**13. ABSTRACT (Maximum 200 Words)**

The goal of this project is to combine features derived from ultrasound (US) images, US radio frequency (RF) data, tissue elasticity imaging, and clinical data such as PSA into a computerized system for displaying prostate images that indicate probable location(s) of cancer. This project began by gathering RF from in-vitro prostatectomy specimens in cross sectional planes 2mm apart. These data are used to calculate RF features such as backscatter coefficient at each location in the gland. The data are also used to generate images and elastograms from which image texture and tissue hardness features are computed. The features are correlated with histology from the same location in the prostate to determine which feature combinations accurately predict the presence of cancer.

Despite the failure of Univ. of Texas to provide new elastography software and the abrupt departure of the laboratory assistant in June, significant progress in software development was made in the past year resulting in software that allows one to mark a region on a digital microscopic image of the prostate with automatic computation of RF and texture features for that region. Using this software, 55 benign and cancerous regions were studied. For this set of regions, RF slope and Co Occurrence Matrix Entropy (ENT) were the best features for distinguishing cancer from benign tissue (Mahalanobis dist.= 1.498, Az = .77). Some of the RF data acquired were acquired incorrectly necessitating acquisition of additional patients. Software to include elastographic features is being incorporated into the analysis package. With successful repair of the ultrasound scanner, acquisition of RF using an endorectal probe should begin within two months.

14. SUBJECT TERMS

Prostate Cancer, ultrasound, elastography, tissue characterization

15. NUMBER OF PAGES

127

16. PRICE CODE**17. SECURITY CLASSIFICATION
OF REPORT**

Unclassified

**18. SECURITY CLASSIFICATION
OF THIS PAGE**

Unclassified

**19. SECURITY CLASSIFICATION
OF ABSTRACT**

Unclassified

20. LIMITATION OF ABSTRACT

Unlimited

NSN 7540-01-280-5500

Standard Form 298 (Rev. 2-89)
Prescribed by ANSI Std. Z39-18
298-102

FOREWORD

Opinions, interpretations, conclusions and recommendations are those of the author and are not necessarily endorsed by the U.S. Army.

___ Where copyrighted material is quoted, permission has been obtained to use such material.

___ Where material from documents designated for limited distribution is quoted, permission has been obtained to use the material.

___ Citations of commercial organizations and trade names in this report do not constitute an official Department of Army endorsement or approval of the products or services of these organizations.

___ In conducting research using animals, the investigator(s) adhered to the "Guide for the Care and Use of Laboratory Animals," prepared by the Committee on Care and use of Laboratory Animals of the Institute of Laboratory Resources, national Research Council (NIH Publication No. 86-23, Revised 1985).

X For the protection of human subjects, the investigator(s) adhered to policies of applicable Federal Law 45 CFR 46.

N/A In conducting research utilizing recombinant DNA technology, the investigator(s) adhered to current guidelines promulgated by the National Institutes of Health.

N/A In the conduct of research utilizing recombinant DNA, the investigator(s) adhered to the NIH Guidelines for Research Involving Recombinant DNA Molecules.

N/A In the conduct of research involving hazardous organisms, the investigator(s) adhered to the CDC-NIH Guide for Biosafety in Microbiological and Biomedical Laboratories.


(electronic signature)

13 Dec 2001

PI - Signature
TABLE OF CONTENTS

Date

INTRODUCTION	5
RESEARCH ACTIVITIES	6
KEY RESEARCH ACCOMPLISHMENTS	16
REPORTABLE OUTCOMES	16
CONCLUSIONS	17
REFERENCES	18
APPENDICES	19

INTRODUCTION

The ultimate goal of this project is to combine features derived from ultrasound (US) images, US radio frequency (RF) data, tissue elasticity imaging, and clinical data such as PSA into a computerized system for displaying prostate images that indicate probable location(s) of cancer. Each of these different classes of features has been shown to be useful for prostate cancer detection. By combining those features in each class that perform best in a set of test cases, we hope to develop an accurate tool for detecting regions on the ultrasound image that a high probability for cancer. Eventually we hope these techniques will be used to rapidly identify high probability areas and mark them on the ultrasound image in real time or near real time.

This project began by gathering RF data from in-vitro prostatectomy specimens in cross sectional planes 2mm apart using a linear array transducer. These data are used to calculate RF features such as power spectrum slope, and backscatter coefficient at each location in the gland. The data are also used to generate images and elastograms from which image texture features and tissue hardness features are computed. The features will be correlated with histology taken at the same tissue planes to determine which features and feature combinations most accurately predict the presence of cancer. The various image, hardness, and RF features will then be combined with prior probability information derived from an AFIP 3D model of prostate occurrence and with clinical PSA values to produce a system that can accurately identify the presence of prostate cancer using ultrasound data.

After developing the techniques to perform identification of prostate cancer using the linear array scans, our plan is to migrate the technique to data from a curved array transducer and then finally to data from an endorectal prostate probe. We hope in the end to be able to demonstrate an in vitro system using an endorectal prostate probe that will be able to mark areas of high probability for cancer on each ultrasound image. This will prepare us for an in vivo study directed at developing an ultrasound system that can better direct biopsies of the prostate gland to areas of high likelihood for actual prostate cancer.

RESEARCH ACTIVITIES AND PROGRESS

Administrative Overview:

Our efforts in the third year of the project have been focused on continuing the clinical data acquisition begun in June 1999, continuing to work with Mr. He, the graduate student to refine the software to compute the ultrasound based features, and on completing development of a system for correlating ultrasound features with pathology on "whole mount equivalent sections" made by reassembling pathology slide sections. We have succeeded in developing this system and preliminary results were reported in June 2001.

The graduate student on the project, Mr. Xhe He continued working on the project and completed a usable version of software for ultrasound data analysis by May 2001. Preliminary analysis was carried out using this software and then Mr. He took some time out to write his masters thesis based on the work, which was completed in September 2001 and accepted by the graduate college in October 2001. Mr. He received his masters degree in October for the work. Training of Mr. He has continued with numerous software refinements currently underway. The main goal for the next version is to include elastographic features in the analysis and to modify the manner in which user selected regions of interest are selected. Mr. He has tentatively agreed to continue on in his studies towards a Ph.D., which means that he will continue to work on the prostate project. This eliminates the need to train a new graduate student.

Development of a user-friendly interface for the software has consumed a significant amount of Mr. He's time forcing him to devote less time to the critical questions of ultrasonic feature computation and software testing. To assist with these software development issues, a programmer has been hired on a part time basis. Mr. Steven Felker, the programmer, has worked with the ultrasound research group as a senior computer science major and has developed considerable familiarity with Matlab programming. He will assist with file conversion software, and graphical user interface software development to allow Mr. He to focus more on feature computation and data fusion issues.

The complex process of combining the quarter section pathology slide images into the equivalent of whole mount sections for comparison with the ultrasound images and data has been handled in the past year by the research assistant Gorana Skjclarevski. She was trained in this process by Dr. Mark Tuthill of the Department of Pathology and became quite proficient at scanning microscope slides, rearranging them, labeling the resultant image files in an organized way, and combining them into complete cross sectional images of the prostate gland. These cross sectional images were then placed into a database for use by the ultrasound analysis software developed by Mr. He. Unfortunately Ms. Skjclarevski left the project suddenly in June 2001 after her husband took a job in another city. This brought to a halt both ultrasound data acquisition and pathology image processing.

A search for a replacement was instituted and in September 2001, Mr. Steven Knight was hired. The principal investigator trained Mr. Knight in the ultrasound data acquisition from prostatectomy specimens over a four-week period and Mr. Knight also received training from Dr. Tuthill on

pathology image reassembly. Unfortunately, after the training period, Mr. Knight performed only two ultrasound acquisitions in two months and performed no pathology image assembly. It was clear that because of workload and personal problems that Mr. Knight could not perform the jobs expected of him so he was asked to resign in late November and tendered his resignation shortly thereafter.

A search is underway for a replacement and during the interim period, the P.I. will perform ultrasound data acquisition and pathology image assembly as time permits.

In summary, the first half of the year was very productive but work in the second half of the year was hampered by the loss of the laboratory assistant and the failure of her replacement to carry on the data acquisition/image processing work. Additional computer programming expertise has been hired to speed up software development and a search for a laboratory assistant continues. As we had several candidates for the job before selecting Mr. Knight, we are optimistic about hiring a new, more reliable, laboratory assistant in the very near future.

RESEARCH PROGRESS

Task 1 (Months 1-6): Collect RF data on 25 prostate glands with the linear array transducer. Develop a preliminary plan for data acquisition for tasks 5 and 7.

This portion of the project was completed prior to the 1999 annual report and is outlined in that document. No further changes to data acquisition were made in the past year other than a reduction in the number of sutures used to mark the index slice of the ultrasound study. This change was done to reduce the amount of time that the specimen spent in the ultrasound lab prior to being received by pathology.

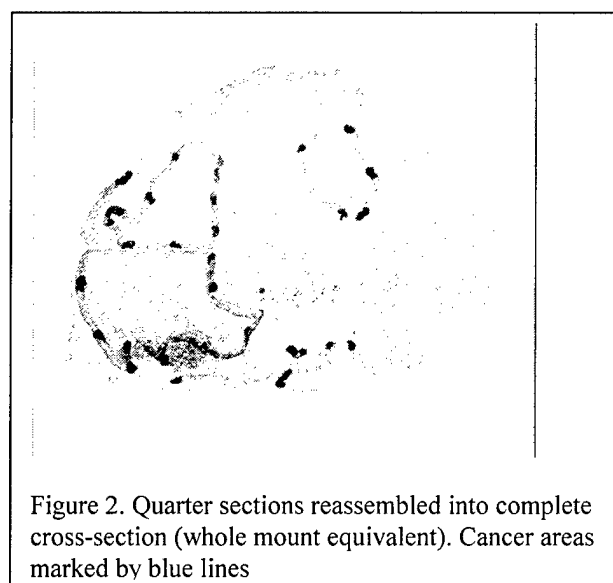
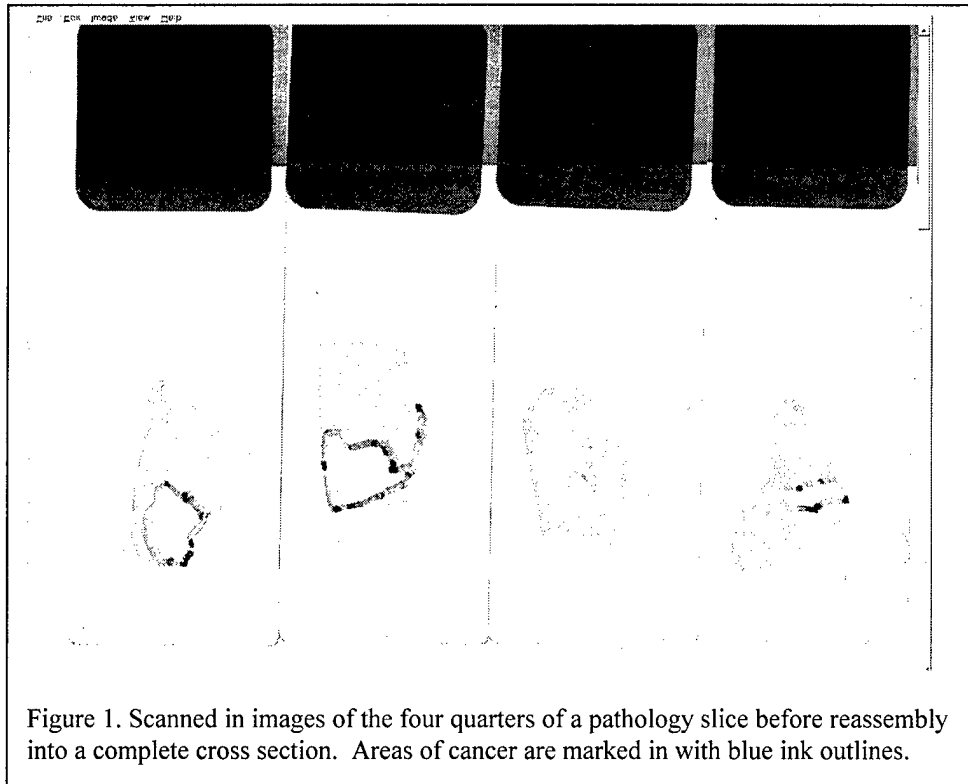
Task 2 (months 1-6): Develop a methodology for registering optical pathology information with ultrasound data.

The procedure outlined in the previous annual report was successfully implemented as outlined in the previous report with only minor modifications. The procedure now consists of the following steps:

1. The prostatectomy specimen is fixed in formalin.
2. The gland is sectioned every 2-3mm after coating the surface of the gland with inks of various colors to identify anterior and posterior surfaces
3. Each 2-3mm thick whole cross section is divided into quarters.
4. The quarters are labeled and embedded in paraffin
5. The embedded quarters are sectioned and mounted onto glass slides
6. The slides are stained and examined by the pathologist—Dr. Trainer
7. Areas of cancer are marked on the slides in indelible ink
8. The slides are digitized by placing them on a flatbed scanner and scanning at 300dpi. This produces pathology images of high enough resolution without producing unnecessarily large image files—see figure 1.

9. The slide images (including identification labels indicating the original slice position and quarter) are imported into Adobe Photoshop and reassembled into complete cross sections (“whole mount equivalents”).
10. The whole mount equivalent images are placed into a database on a shared disk drive for later comparison with ultrasound data.

An example of a “whole mount equivalent” image assembled from quarter sections is shown in figure 2.



A few modifications to the original procedure outlined in the prior report were made. No warping of pathology images was performed due to concerns by the pathologists that such a procedure might introduce undesirable distortions into the pathology data. Thus some of the whole mount equivalents have gaps where the quarter sections did not fit precisely with one another. This has not proved to be a problem for correlation with ultrasound data. When looking for benign or malignant areas, the gaps are simply avoided. Software to perform the selection a corresponding pathology whole mount equivalent image based on the registration scheme described in the 2000 report has been developed and successfully used. See task 4 description for further discussion.

In Summary, a method for registration of histologic information with ultrasound raw data has been developed and is in use in other phases of the project. Task 2 is complete.

Task 3 (months 1-6): Use digital database of prostate cancer rate developed at Georgetown University and AFIP to establish a probability map of prostate cancer in a 3D domain.

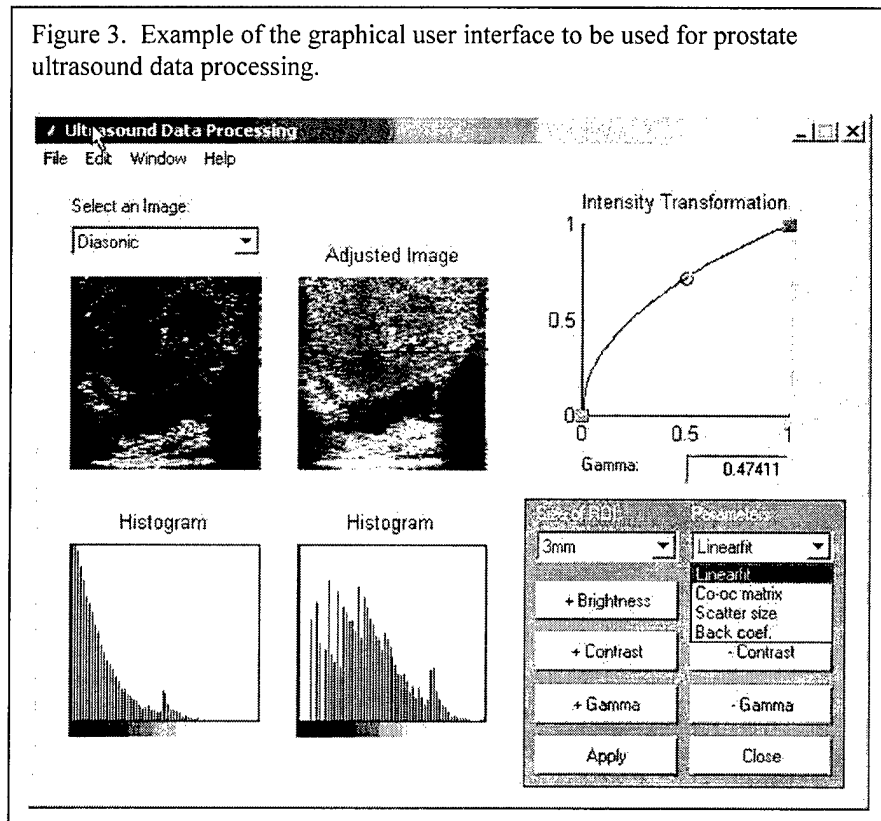
The available pathology data from UVM have been transferred to Georgetown University for probability map creation. The creation of the probability map and 3D distribution mapping has been described in the previous report. Although the probability distribution map has not yet been created, it is not needed at this point since incorporation of prior probabilities is needed only in the final phases of UNKNOWN region of interest classification and we are still in the phase of computing features for KNOWN regions of interest to determine which features best discriminate cancer from benign tissue.

Further work on 3D modeling at UVM has been put on hold pending hiring of a replacement for the research assistant.

Task 4 (months 1-9): Software development. Adapt existing RF analysis software and incorporate texture analysis. Develop software to automatically calculate RF and texture features over multiple subregions in an image.

Rather than adapt existing RF analysis software, it turned out to be more educational and expedient to develop new software based on MATLAB to compute both RF and Texture features. The previously reported user interface (figure 3) was completely revamped to give the user a way to process regions of interest selected from a pathology image.

Figure 3. Example of the graphical user interface to be used for prostate ultrasound data processing.



This new software, which is designed to allow a user to identify a normal or cancerous area on the pathology image and find the corresponding region in the ultrasound data set, has been completed and used successfully to analyze ultrasound data. The software was developed in MATLAB with a Windows Graphical User Interface. To calculate RF or texture features the user selects the ultrasound data file that he/she wishes to use. The software automatically selects the pathology slice the most closely corresponds to the ultrasound data based on the slice correlation scheme as reported in the previous annual report. The user then adjusts the size of the pathology image to match the ultrasound image by drawing a box around the image of the prostate that touches the image of the gland on all four sides. The pathology image is then oriented to match the ultrasound data—this usually involves rotating the pathology image 180 degrees. The user then draws a region of interest on the pathology specimen and specifies whether it is a cancerous or benign region. The software automatically finds the corresponding region on the corresponding ultrasound image, finds the raw RF data corresponding to that region, and computes RF and textures features from the RF data and places the results in a data base. It is also possible to draw multiple regions and then have the software process the RF for all regions of interest at a later time as a batch process. Figure 4 shows the new GUI interface.

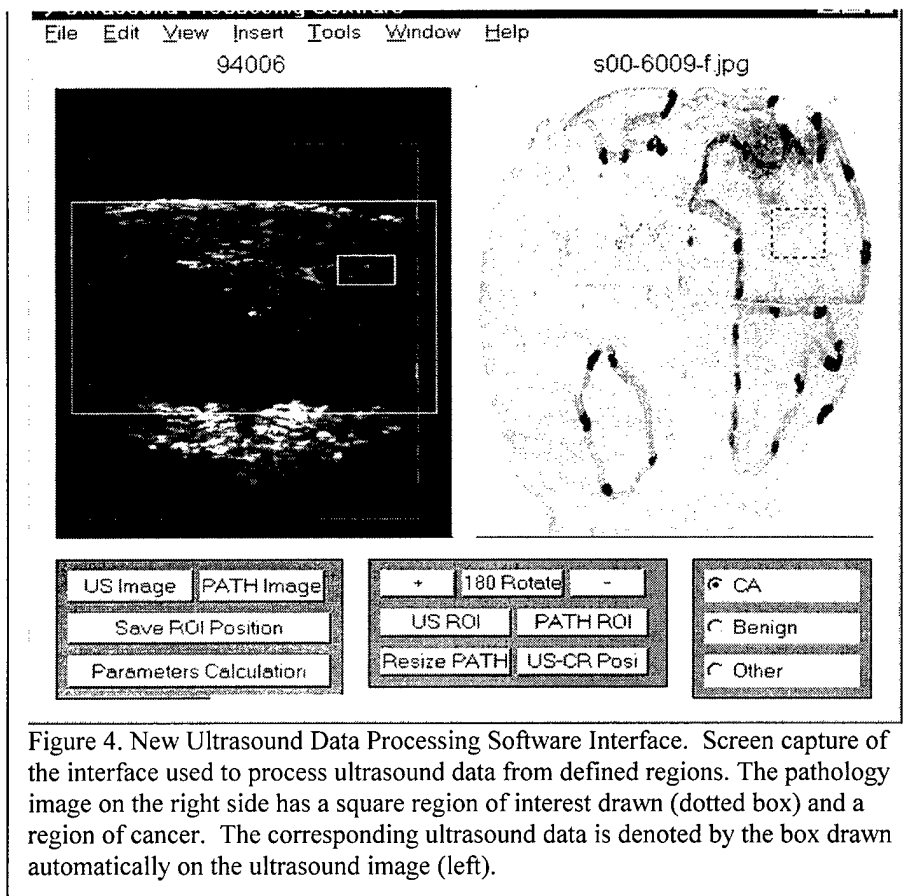


Figure 4. New Ultrasound Data Processing Software Interface. Screen capture of the interface used to process ultrasound data from defined regions. The pathology image on the right side has a square region of interest drawn (dotted box) and a region of cancer. The corresponding ultrasound data is denoted by the box drawn automatically on the ultrasound image (left).

Of course, although this new user interface was designed to let the user process selected regions of interest so that a database of features values for cancer and benign tissue could be generated, the software is also capable of processing RF data from entire slices or multiple slices, automatically subdividing the data into subregions and calculating features for those regions.

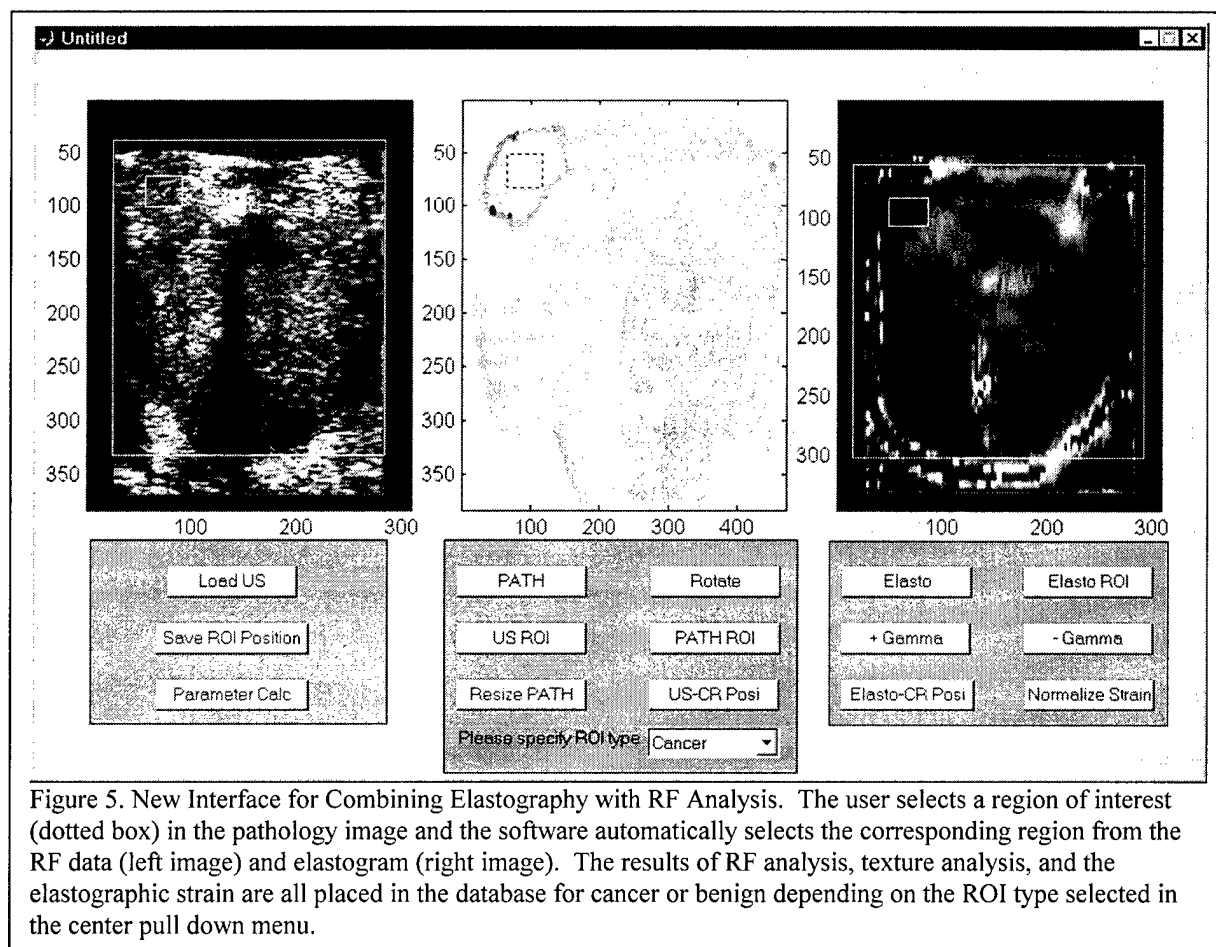
The software outlined above was used to analyze a large subset of our acquired data to verify correct operation of the software and to begin to determine the most useful feature combinations as outlined in Task 7. See task 7 description for our preliminary results. Based on these results, one important modification was made in the way the software computes features. In previous versions, the region of interest size was variable and controlled by the size selected by the user. Evidence that ROI size biases the feature results prompted us to allow users to select an ROI but features are computed from subregions of the ROI of FIXED size to eliminate this bias.

In Summary, the basic parts of task 4 are complete but ongoing modification continues to incorporate data fusion elements (from Task 5) and to make the software more accurate, robust and convenient to use.

Task 5 (months 12-18): Data Fusion

Having developed the software to use pathology images to select data for RF processing, we began the process of development of data fusion software to combine elastography results with

RF results in user-selected regions of interest. Having had success, with an interactive scheme for orienting pathology images with those from ultrasound RF data, we have elected to initially use the same approach for elastography, processing the elastographic data separately using software from the University of Texas and combining those results with those from the RF analysis. We have completed the development of software that calculates RF and texture features from data corresponding to a user selected region on a pathology image AND selects the appropriate region from the corresponding elastographic image placing the mean strain value from the elastogram ROI into the feature database (figure 5).



The user draws boxes around each image to inform the software of the relative sizes of the prostate in each image so that the software can find corresponding regions on each image. This method eliminates problems from distortion of the image in the vertical direction that can occur in elastography. The software also allows the user to adjust the display of the elastogram since the elastographic data may not always give a pleasing image without grayscale processing.

The new software represents a significant programming change in that the tools used (Matlab Guide) are different from the previous version of software. This necessitated a significant rewrite of code but should yield benefits in the future should further modifications to the user interface be required. The elastographic data are currently being acquired from the actual elastographic image, which is a map of strain values windowed into 256 shades of gray. The next version may use the unwindowed strain values. At a still later time, it may be appropriate to calculate the elastographic data directly from the RF after the region of interest is selected. This issue will be addressed after new elastographic routines that include effective lateral motion correction are developed with the help of Dr. Konofagu as noted below.

One issue of great concern is the quality of the elastographic data. Since the prostate glands are not embedded in gel as were the glands scanned by other investigators in animal work, there is great potential for lateral decorrelation which increases the noise in elastograms and decreases the contrast between benign and malignant tissue. Software with improved ability to correct for lateral motion was expected from the University of Texas by April 2001. It finally arrived in October 2001 but has not performed to expectations on test objects. Elastography software problems and personnel problems at Texas have prompted us to move forward with the development of new elastography software incorporating high quality lateral correction on our own. I have enlisted the help of Eliza Konofagu (currently a postdoctoral fellow at Harvard) to head the development effort with the aid of graduate students at the University of Texas. Steve Felker will coordinate integration of the new elastography software with our RF software developed by Mr. He.

Another issue with elastography that was mentioned previously is the problem of quantifying what have been regarded as qualitative images. Our plan to use the change in thickness of the overlying standoff pad as a means of normalizing the strain values has been hampered by the fact that many of the elastograms collected did not include enough of the standoff pad to measure it accurately. We have modified the data acquisition routine to eliminate this problem, but it means that some additional data with the linear array alone must be acquired to have a sufficient sample of cancers. We have acquired approximately 10 glands using the modified technique and must acquire an additional 10 to 15 more. In addition, we plan to test the normalization routines on a phantom test object containing a hard inclusion of known stiffness relative to the surrounding material. This object is under construction at the University of Wisconsin.

Task 6 (months 7-18): More prostate data collection.

As mentioned in the previous section, software from the University of Texas expected to allow acquisition at higher compressions for higher image quality did not meet expectations and because of personnel problems at UT, hopes for new software have faded. Thus experiments using larger compressions are on hold pending internal development of new elastography software incorporating lateral correction and estimation of lateral strains.

In the previous report, the failure of our primary ultrasound instrument was documented as were our plans should the instrument prove irreparable. Luckily, we were able to find a service engineer with experience on the old Dasonics systems and in February 2001, the Dasonics unit was repaired and became operational again. By this time, we had identified some problems with the RF data already acquired (such as the absence of a visible overlying standoff on some cases and saturation of the A/D converter on others) and decided to acquire 15-20 additional prostate cases using the linear array before moving on to linear + endorectal curved array acquisitions. We have acquired about 10 of those cases despite the delay caused by the laboratory technician's departure. We hope to begin test acquisitions with the curved array probe in January or February 2002 with or without a replacement laboratory assistant. The PI will perform the acquisitions but since acquisition with both a linear array and curved array will require upwards of two hours—usually during busy clinic hours, a replacement lab assistant is hoped for to reduce conflicts between acquisitions and the clinical responsibilities of the PI.

Task 7 (months 11-22): Compute RF and texture features for all stage 1 acquisitions.

Computation of RF and Texture Features on approximately 75% of the existing data was completed by June 2001. Potentially useful features were identified using the Mahalanobis distance as an index of the usefulness of both single features and feature combinations for separating benign from cancerous tissue. Figure 6 shows the experimental setup used:

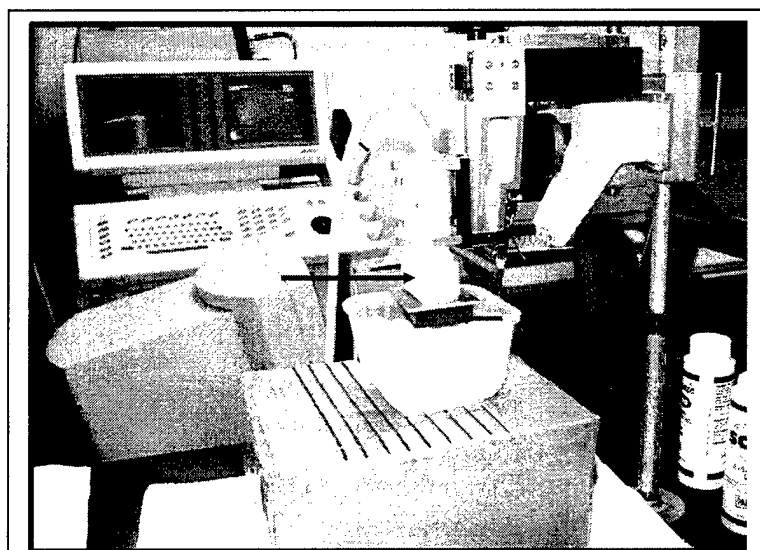


Figure 6: Data Acquisition Setup. The prostate gland is embedded in toweling and flooded with normal saline. The ultrasound probe (long black arrow) is held vertically and compresses the gland driven by a computer controlled stepper motor. The standoff gel block is held in place by the reddish orange plastic block (short black arrow) attached to an aluminum pressure plate attached to the transducer.

At total of eight different RF and texture features were computed from selected regions of interest. Features based on the RF data included the slope of backscatter vs. frequency, the zero frequency intercept of the backscatter intensity, and the mid bandwidth value for backscatter¹. One feature based on image statistics was computed, this was the image signal to noise ratio $(\mu/\sigma)^2$. Four image texture features based on the co-occurrence matrix were computed: angular second moment, entropy, contrast, and correlation³. The features were computed from 36 cancer regions of interest and 19 benign regions of interest. Table 1 shows the mean and standard deviations for

the various features.

Table 1. Feature Values for Benign and Malignant Prostatic Tissue

FEATURE	CANCER (Mean \pm s.d.)	BENIGN (Mean \pm s.d.)
Slope	0.778 \pm .348 dB/MHz	.588 \pm .326
Intercept	-11.81 \pm 2.19 dB	-10.41 \pm 2.20
Mid Band Value	-7.88 \pm 1.48 dB	-7.42 \pm 1.57
Signal to Noise Ratio	1.62 \pm .38	1.36 \pm .35
Angular Second Moment	.0099 \pm .018	.0029 \pm .0026
Entropy	-5.4 \pm 1.04	-6.42 \pm .78
Contrast	4111 \pm .38	2066 \pm 1049
Correlation	-.7469 \pm .115	-.8043 \pm .0788

The Mahalanobis distance is a measure of the statistical distance between two clusters of values relative to the scatter or variance of those values. To provide good discriminability between benign and cancerous prostate tissue, the Mahalanobis distance should be maximized. Table 2 shows the Mahalanobis distance between cancer and benign tissue using linear discriminant analysis and various features or feature combinations. The discriminant analysis was performed using Minitab R13 software using the leave-one-out (cross-validation) method. This method minimizes the optimistic bias that results from using the same data for both training and performance estimation.

Table 2. Feature Performance for Cancer vs. Benign	
FEATURE (S)	MAHALANOBIS DISTANCE
Slope & Intercept	0.418
Intercept & Entropy	1.351
Slope & Entropy	1.498
Intercept & Contrast	0.765
Entropy & Contrast	1.14
Slope	0.309
Intercept	0.403
Signal to Noise, Slope, Entropy	1.700

As is usually the case, more features lead to larger values and greater separation. But with the limited data set at hand, it is appropriate to use no more than 2-3 features to avoid an optimistically biased estimate of performance for the task of separating cancer from benign tissue. Receiver operating characteristic analysis was

applied to the best two-feature combination, slope and entropy. The resulting area under the ROC curve was $A_z = .77$, far from ideal but still encouraging.

During the analysis, it was noted that the size of the region of interest used could affect the results—especially for SNR and the texture features. Since benign regions of interest tended to be larger than cancer regions, some of the difference in features could be the result of ROI size. To eliminate this effect, we have modified the software so that regardless of the size of ROI chosen by the human observer, the features are all computed from sub regions of identical size (approx RF lines wide). For a large region of interest, more subregions are present but this no longer affects the mean value, only the variance and Standard Error of the Mean. We have recomputed all features using this technique but the results have not yet been analyzed. A

disadvantage of this new method is that computation times become very long. We are minimizing this by acquiring a faster PC for processing.

In summary, we have completed processing of a considerable portion of the RF data and the results are promising. Using the knowledge we acquired performing that processing, we are acquiring some additional data and are modifying the way we compute the features to remove bias and increase reliability. We are in the process of combining the elastography feature with the RF, image, and image texture features.

Task 8 and Task 9 (months 13-26 and 24-30): Acquire RF with a curved array transducer.

As mentioned in Task 6, collection of data using a curved array transducer will begin shortly. The software developed for linear array data will require some modification so that the correct region is obtained from the ultrasound data once the pathology image region of interest is selected. This problem (one of scan conversion—i.e. polar to rectangular coordinate conversion) should be solvable in a short period of time. Elastography with a curved array has already been demonstrated to be feasible, but the problem of how to normalize elastograms to correct for the non-uniform stress distribution has yet to be solved. One method is to use a modification of the method we plan for the linear array, but measure standoff distances along each A-line and perform normalization one A-line at a time. This method will be tested on the phantom test object currently under construction. Since the Dasonics scanner is once again operational, there will be no need to change scanners although a change is still possible should the Dasonics instrument fail or should the Dasonics endorectal probe (old and obsolescent) prove to give data of inferior quality.

RESEARCH ACCOMPLISHMENTS

- Software has been developed under this program that can reliably find ultrasound data corresponding to an area of pathology on a pathology image. This technique could have broad applicability to any situation where in-vitro scans are being correlated with pathology.
- Software for computing both RF based and image texture based features for prostatic tissue or any other tissue has been developed and tested.
- Preliminary analysis shows that the features are promising and suggest that RF and texture based features can be used to discriminate between cancer and benign tissue. Discriminability will hopefully be further enhanced by adding elastography.
- Software to combine elastographic strain data with RF and texture features has been developed and is being refined.

REPORTABLE OUTCOMES

1. Database of completely sectioned prostate glands with all cancer foci located plus correlated ultrasound raw data. This is a valuable resource that may be used for studies of the distribution of cancer and for any study requiring ultrasound image or raw data that

can be precisely correlated with histology. The combining of this data set with the AFIP data set will produce a larger and more reliable data set than now exists for estimation of the probability of cancer as a function of location in the gland.

2. Abstract: He Z, Skljarevski G, Trainer T, Tuthill JM, Wagner RF, Huston D, Garra BS. Classification of benign and malignant prostate tissue using radio frequency ultrasound data: preliminary results of in vitro studies of radical prostatectomy specimens. Ultrasonic Imaging 2000;22:238. ----- see Appendix 1.
3. Presentation: He Z, Skljarevski G, Trainer T, Tuthill JM, Wagner RF, Huston D, Garra BS. Classification of benign and malignant prostate tissue using radio frequency ultrasound data: preliminary results of in vitro studies of radical prostatectomy specimens. Presented at the 26th International Symposium on Ultrasonic Imaging and Tissue Characterization, Rosslyn, VA, May 31 2001-----See Appendix 2
4. Thesis: He, Zhi, Quantitative Sonographic Prostate Cancer Characterization, Masters of Science Thesis, October 2001 ----- See Appendix 3
5. Masters Degree Awarded October 2001 to Zhi He
6. Employment & Training Supported by this Project Funding:
 - a. Masters and Doctoral Training by Zhi He
 - b. Part time Programmer: Steven Felker
 - c. Half time Research Assistant: TBN (currently vacant position)

CONCLUSIONS

Despite problems caused by the departure of the research assistant and continued delays in receiving software for elastography from the University of Texas, considerable progress has been made in the past year with completion of software and a procedure for precisely correlating pathology and ultrasound data acquired in vitro with approximately 2mm spatial accuracy. These methods and the software could be applied to other organs with equal success.

Our preliminary analysis of the RF data suggest that cancerous tissue can be differentiated from benign tissue using RF and texture features. Some of the RF data is of poor quality necessitating acquisition of some additional data—this will be acquired in a modified fashion that will allow for normalization of the elastographic data in a novel manner that is simple but robust (unlike other methods that have been reported such as computation of the elastic modulus). Additional personnel have been hired to speed up software development and incorporation of higher quality elastography strain data into our database.

We are almost ready to tackle the problem of using a curved array transducer but are confident that the needed modifications can be made to our software so that it will work properly with the new transducer array. We remain confident that we will be able to produce probability images showing areas likely to contain cancer using the combination of RF, texture, and elastographic features. This has the potential of being a valuable tool for clinicians using ultrasound to guide biopsies AND with the release of standard clinical ultrasound machines capable of storing raw ultrasound data (such as the new General Electric Logiq 9), it will be something that can be implemented on existing commercial hardware!

REFERENCES

-
- ¹ Feleppa EJ, Liu T, Kalisz A, Shao MC, Fleshner N, Reuter V, Fair WM. Ultrasonic spectral parameter imaging of the prostate. *Int J Imaging Syst Technol.* 1997;8:11-25.
- ² Wagner RF, Smith SW, Sandrik JM, Lopez H. Statistics of Speckle in ultrasound B-scans. *IEEE Trans. Sonics Ultrason.* 1983;SU-30:156-163.
- ³ Garra BS, Krasner BH, Horii SC, Ascher S, Mun SK, Zeman RK. Improving the distinction between benign and malignant breast lesions: the value of sonographic texture analysis. *Ultrasonic Imaging* 1993;15:267-285.

APPENDICES

Appendix 1

PROGRAM AND ABSTRACTS

26th International
Symposium on

Ultrasonic Imaging and Tissue Characterization

May 30 – June 1, 2001

Holiday Inn/Rosslyn Westpark Hotel
Arlington, VA

PROGRAM

WEDNESDAY, MAY 30

- 7:30 a.m. Registration/Coffee and Pastry
- 8:30 a.m. Introduction
M. Linzer, *Symposium Chairman*
- 8:35 a.m. 1. ELASTICITY 1 (Invited Papers)
Chmn: J. Ophir, *U. Texas*
- 1.1 Mechanical testing of soft tissues – time, temperature and size considerations — Thomas A. Krouskop and Faouzi Kallel, *Baylor Coll. Med. and U. Texas Med. School*
- 1.2 Factors and tradeoffs affecting image quality in elastography — T. Varghese, J. Ophir, E. Konofagou, F. Kallel and R. Righetti, *U. Wisconsin-Madison, U. Texas Med. School, Harvard Med. School and U. Houston*
- 1.3 Axial resolution in elastography — R. Righetti and J. Ophir, *U. Texas Med. School and U. Houston*
- 10:02 a.m. Coffee
- 10:46 a.m.
- 1.4 Transient elastography — M. Fink, S. Catheline, L. Sandrin and M. Tanter, *ESPCI, Université Denis Diderot, France*
- 1.5 Frequency-domain and rigid-body motion estimators for elastography — S. Kaiser Alam, Frederic L. Lizzi, Ernest J. Feleppa and Tomy Varghese, *Riverside Research Inst. and U. Wisconsin*
- 1.6 In-vivo elastography of the prostate and HIFU applications: initial results — Rémi Souchon, Jean-

The annual International Symposia on Ultrasonic Imaging and Tissue Characterization have long been recognized as the world's leading forums concerned with ultrasonic techniques for medical diagnosis. This year, sessions will be devoted to Elasticity, Tissue Parameters and Imaging/Doppler. Forty-one contributions from six countries will be presented at these sessions. A large number of papers will deal with clinical evaluation of novel methodology and instrumentation for tissue characterization.

A special one-day session on Elasticity will take place on Wednesday, May 30. It will feature fifteen papers in sessions of invited and contributed papers and will conclude with an hour-long panel discussion.

The abstracts for the meeting have been published in the October 2000 issue of the journal *Ultrasonic Imaging* (Dynamedia) and will be distributed to the attendees at the time of the meeting. No proceedings will be published.

PROGRAM COMMITTEE

M. Linzer, *Chairman*
F.L. Lizzi, *Riverside Research Institute*
M. Fink, *University of Paris VII*
J.G. Miller, *Washington University*
J. Ophir, *University of Texas, Houston*
R.L. Parker, *U. Rochester*

CORPORATE SPONSORS

Advanced Technology Laboratories, Inc.
Bothell, WA

GE Medical Systems
Milwaukee, WI

Yves Chapelon, Olivier Rouvière, Albert Gelet, Faouzi Kallel and Jonathan Ophir, *INSERM, Hôpital Edouard Herriot, France and U. Texas Med. School*

12:10 p.m. Lunch

1:45 p.m. 2. ELASTICITY 2
Chmn: R.J. Parker, *U. Rochester*

2.1 Noninvasive monitoring of temperature and lesion formation during rf ablation — T. Varghese, J.A. Zagzebski, Q. Chen, G. Frank, U. Techavipoo and F.T. Lee, Jr., *U. Wisconsin-Madison*

2.1 Experimental evidence of anisotropy of muscle using transient elastography — J.-L. Genisson, S. Catheline, S. Chaffai, L. Sandrin and M. Fink, *ESPCI, Université Paris VII*

2.3 Vibrational Doppler imaging and spectroscopy for breast mass detection and characterization — B.S. Garra, G.S. Lin, L. Mobbs and R. Oppenheimer, *U. Vermont Coll. Med. and Advanced Imaging Assoc.*

2.4 In-vitro imaging of lesion models using sonoelastography — L.S. Taylor, J.G. Strang, Z. Wu, B.C. Porter, D.J. Rubens and K.J. Parker, *U. Rochester*

2.5 In-vivo sonoelastography of the human prostate: system improvements and new results — L.S. Taylor, D.J. Rubens and K.J. Parker, *U. Rochester*

3:10 p.m. Coffee

3:52 p.m.

2.6 Transrectal prostate elastography: numerical and experimental studies — Lahbib Soualmi, Rémi Souchon, Michel Bertrand and Jean-Yves Chapelon, *École Polytechnique, Canada and INSERM, France*

2.7 Jitter correction of digitized A-lines to improve speckle motion estimation — Roch Maurice, Rémi Souchon, Michel Bertrand and Jean-Yves Chapelon, *École Polytechnique, Canada and INSERM, France*

2.8 On Matlab parallel processing for modeling and applications in elastography — Erland Svahn, Guy Charron and Michel Bertrand, *École Polytechnique, Canada*

2.9 Imaging nonlinear elastic properties in soft tissue — R.Q. Erkamp, S.Y. Emelianov, A.R. Skovrova, X. Chen, and M. O'Donnell, *U. Michigan and Inst. Math. Problems in Biology, Russia*

5:00 p.m. 3. ELASTICITY 3 (Panel Discussion)
Chmn: J. Ophir, *U. Texas*
Bertrand, Fink, Garra, Krouskop, Parker

6:00 p.m. Adjourn

6:30 p.m. Open bar

7:15 p.m. Banquet

THURSDAY, MAY 31

7:30 a.m. Coffee and Pastry

8:30 a.m. 4. TISSUE PARAMETERS 1
Chmn: E.J. Feleppa, *Riverside Res. Inst.*

4.1 Classification of benign and malignant prostate tissue using radio frequency ultrasound data: preliminary results of *in vitro* studies of radical prostatectomy specimens — Z. He, G. Skljarevski, T. Trainer, J.M. Tuthill, R.F. Wagner, D. Huston and B.S. Garra, *U. Vermont and FDA*

4.2 Application of spectrum-analysis and neural-network-based imaging to detection and treatment of prostate cancer — Ernest J. Feleppa, Andrew Kalisz, Jeffery Ketterling, Stella Urban, William R. Fair, Christopher Porter, Peter B. Schiff, Ronald Ennis, Cheng-Shie Wu and Tian Liu, *Riverside Research Inst., Haelth, Veterans Affairs Medical and Columbia NY Presbyterian Med. Ctr.*

4.3 Novel ultrasonic visualization of brachytherapy seeds — S. Kaisar Alam, Ernest J. Feleppa, Frederic L. Lizzi, Ronald D. Ennis, Jeff Ketterling, Stella Urban, Tian Liu and Cheng-Shie Wu, *Riverside Research Inst. and Columbia U.*

4.4 3-D images of the human eye using very high frequency ultrasound: synthesis, biometry and treatment planning — F.L. Lizzi, C.X. Deng, R. Muratore, S. Mikaelian, D.J. Coleman and R.H. Silverman, *Riverside Research Inst. and Cornell U.*

4.5 Evolution of backscatter (12-25 MHz) with depth in human skin *in vivo* — C. Fournier, S.L. Bridal, G. Berger and P. Laugier, *UMR CNRS - Université Paris VI*

9:55 a.m. Coffee

10:40 a.m.

4.6 High-frequency of cartilage lesions — B. Jaffré, E. Bc Pellaumail, G. Berge — *U. Paris VI and C.*

4.7 Clinical assessment parameters: pausal osteoporosis M. Dougados, G. Ber — *U. Paris V, INSERM VII and UMR CNRS*

4.8 Relative roles determining ultrasonic Keith A. Wear, *FDA*

4.9 Parametric II carotid plaque consistency with a clinical ultrasonic Cohen-Bacrie, C. L. Laugier and S.L. Bri Laboratoires d'Electronique d'Anatomie Pathologique des Pompidou

11:50 a.m. Lunch

1:50 p.m. 5. TISSUE PARAMETERS 2
Chmn:

5.1 Optimal transducer skull for ultrasonic Gerber, M. Tanter, J. — *U. Paris VII and UR*

5.2 Phase aberration 8 x 128 array — A. Trahey, *Duke U.*

5.3 Ultrasound processing Fourier-Bessel method D. Fox, Jiqi Cheng

5.4 New method for localities in Doppler Fei, Deepak Ranga — *Virginia Commonwealth U.*

5.5 Error compensation in flow measurement techniques — Subrahmanya Ding-Yu Fei, *Virginia Commonwealth U.*

3:15 p.m. Coffee

4:00 p.m.

Appendix 2

**PROSTATE TISSUE
CLASSIFICATION USING RF
ULTRASOUND
PRELIMINARY RESULTS**

Zhe He J. Mark Tuthill
Gorana Skljarevski Robert Wagner
Thomas Trainer Dryver Huston
 Brian Garra

**UNIVERSITY OF VERMONT &
FDA CENTER FOR DEVICES AND
RADIOLOGIC HEALTH**

Supported by a Grant From the US Army Medical Research & Materiel Command

**IN VITRO PROSTATE TISSUE
CLASSIFICATION PROJECT**

GOAL

To combine ultrasound RF, elastographic, image texture, and clinical features to more accurately locate regions of high suspicion for cancer using prostate ultrasound.

**IN VITRO PROSTATE TISSUE
CLASSIFICATION PROJECT
METHODS 1**

- Scan Entire Prostate Gland in Saline Bath at 2mm Intervals (prostatectomy specimens)
- Scan Calibration Phantom at Same Gain Settings
- Section the Prostate Specimen Along Planes Similar to Those Scanned Using US
- Identify CA & Benign Regions on Path Specimens and in Corresponding US Data Set

**IN VITRO PROSTATE TISSUE
CLASSIFICATION PROJECT
METHODS 2**

- Compute Elastographic, RF, and Texture Features for the CA and Benign Regions
- Determine Which Features Best Separate Cancer From Benign
- Combine Those Features With Location Specific CA Probability and PSA Probability & Generate an Estimator for Cancer Probability
- Begin With Linear Array Data—then Develop a Similar Classifier for Curved Array EC Probe

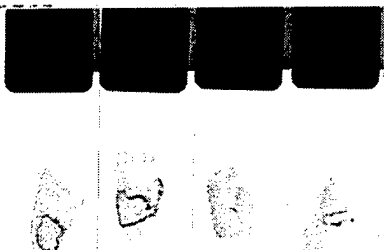
IN VITRO SCAN SETUP



**A COMPLICATION:
PATHOLOGY SECTION
PROCESSING & REGISTRATION**

- "Whole Mount" Sections Are Not Done – Each Pathology Slice Was Divided into Fourths to Fit Microscope Slides
- After Fixation & Staining, CA Areas Are Marked With Indelible Ink
- Marked Slides are Scanned at 400 dpi Using a Flatbed Scanner
- Images are Reassembled Into a Whole Pathology Section Using Photoshop

PATHOLOGY QUARTER SECTIONS WITH CA MARKED



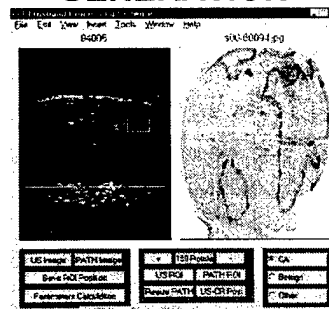
QUARTER SECTIONS ASSEMBLED INTO WHOLE SLICE



IN VITRO PROSTATE TISSUE CLASSIFICATION PROJECT FEATURE COMPUTATION SOFTWARE

- Matlab Based
- Windows GUI
- US Image Selected Causes Corresponding Pathology Image to Be Selected
- Pathology Image Oriented & Sized by User to Match US
- ROI Drawn on Path Image → Corresponding ROI in US RF Data Set

REGION OF INTEREST GENERATION



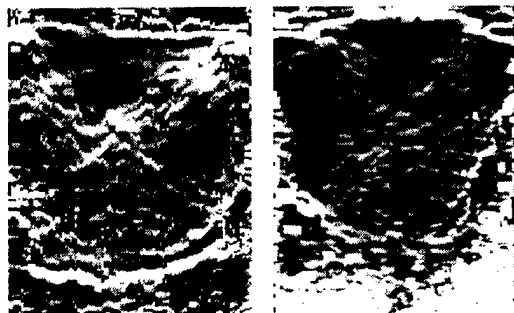
CASE MATERIAL

- 78 Radical Prostatectomy Specimens So Far
- Many With Only Microscopic (1-2mm) Cancer Foci Only
- Data From Many Cases Unusable Due to Technical Problems During Acquisition
- Current Preliminary Analysis Includes:
 - Cancer: 36 ROI from 12 Cancer Patients
 - Benign: 19 ROI from Benign Regions

FEATURES CALCULATED

- RF
 - Backscatter vs. Frequency Slope
 - Backscatter Zero Frequency Intercept
 - Backscatter Mid Band Value
- Image Statistics
 - Signal to Noise Ratio (μ/σ)
- Image Texture
 - CoC Angular Second Moment, Entropy, Contrast, and Correlation
- Elastographic Axial Strain (qualitative only)

PROSTATE ELASTOGRAMS



RESULTS

Feature	CA Mean (\pm s.d.)	Benign Mean (\pm s.d.)
Slope	0.778 \pm .348 dB/MHz	.588 \pm .326
Intercept	-11.81 \pm 2.19 dB	-10.41 \pm 2.20
Mid Band	-7.88 \pm 1.48 dB	-7.42 \pm 1.57
SNR	1.62 \pm .38	1.36 \pm .35
ASM	.0099 \pm .018	.0029 \pm .0026
ENT	-5.4 \pm 1.04	-6.42 \pm .78
CON	4111 \pm 3872	2066 \pm 1049
COR	-.7469 \pm .115	-.8043 \pm .0788

FEATURE PERFORMANCE

FEATURE(S)	Mahalanobis Dist.	Az
Slope & int	.418	
Int & ENT	1.351	
Slope & ENT	1.498	.77
Int & CON	.765	
ENT & CON	1.14	
Slope	.309	
Intercept	.403	
SNR, slope, ENT	1.700	

FUTURE WORK

- Add New Prostate Cases to Improve Database Quality
- Use a Constant Size ROI to Eliminate Bias in Statistical Features Due to ROI Size (est. to be 1/5 to 1/8 of Observed Difference)
- Add the Elastography Results to the Classifier
- Add Cancer Probability Distribution Information to Classifier
- Add PSA Information
- Acquire Data Using a Curved Linear (EC) Probe and Develop a Classifier for That Data



Appendix 3

QUANTITATIVE SONOGRAPHIC PROSTATE CANCER CHARACTERIZATION

A Thesis Presented

by

Zhi He

to

The Faculty of the Graduate College

of


The University of Vermont

In Partial Fulfillment of the Requirements
for the Degree of Master of Science
Specializing in Mechanical Engineering

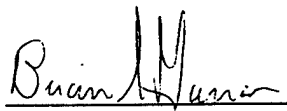
October, 2001

Accepted by the Faculty of the Graduate College, The University of Vermont, in partial fulfillment of the requirement for the degree of Master of Science, specializing in Mechanical Engineering.

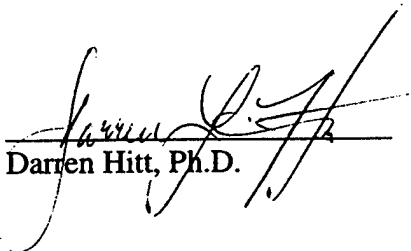
Thesis Examination Committee:



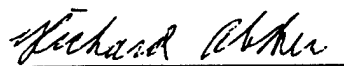
Dryver R. Huston, Ph.D. Advisor



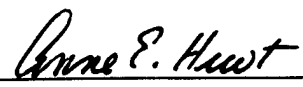
Brian S. Garra, M.D.



Darren Hitt, Ph.D.



Richard Absher, Ph.D. Chairperson



Anne E. Huot, Ph.D. Interim Dean
Graduate College

Date: August 29, 2001

Abstract

Prostate cancer is second only to lung cancer as the cause of cancer deaths among American men. All men are at risk for developing prostate cancer, and as a man ages, his risk of developing prostate cancer increases. The purpose of this study is to combine clinical, ultrasound, and elastographic features into a system to reliably identify areas of the prostate that are likely to be cancerous. The radio frequency (RF) ultrasound data were acquired at 2 mm intervals from 78 radical prostatectomy specimens. After acquiring the ultrasound data, the specimen is sectioned for histological analysis at 2 mm intervals allowing a comparison of each ultrasound 'slice' with a corresponding histology image. The areas of cancer in each histology image are marked by indelible ink and a corresponding region of interest in the ultrasound data set is then found. The ultrasound features used in this study include the basic texture feature – envelope signal-to-noise ratio (SNR), four features coming from the co-occurrence matrix and three features coming from spectral analysis of RF echo signals. Software has been developed to compute feature values at all points in each RF data 'slice'. Using two features together (entropy of a co-occurrence matrix, and correlation of a co-occurrence matrix), the best classification performance is 0.8386 (area under receiver operating characteristic curve). Using three features together (entropy, signal-to-noise ratio, and slope from spectral analysis of radio frequency echo signals), the best classification performance is 0.8541. The preliminary results show RF and envelope-detected signal analyses are diagnostically useful to discriminate cancer in prostate tissue.

Acknowledgements

This project was supported by a contract from the US Army Medical Research and Materiel Command.

I would like to thank my advisor Dr. Dryver Huston for his guidance and support. He has consistently been there to read numerous drafts of this thesis and to offer indispensable advice.

I would also like to thank Dr. Brian Garra for his valuable insight and ideas on the project.

I would also like to thank the members of my thesis committee, Dr. Richard Absher and Dr. Darren Hitt, for their valuable suggestions on the thesis.

I also want to thank Dr. Robert Wagner and Dr. Keith Wear who took time to meet me at D.C. and provided helpful suggestion on how to proceed.

Finally, I would like to thank my wife Qi Yue for her love, understanding, unwavering support and encouragement.

Table of Contents

Acknowledgements	ii
List of Tables	vi
List of Figures	vii
Chapter 1: Introduction and Background.....	1
1.1 Prostate Cancer	1
1.1.1 Introduction.....	1
1.1.2 What is Prostate Cancer	2
1.1.3 Cause of Prostate Cancer	3
1.1.4 PSA	3
1.2 Introduction to Ultrasound.....	4
1.2.1 Introduction.....	4
1.2.2 Ultrasound System.....	4
1.2.3 Medical Ultrasound.....	5
1.2.4 Ultrasound Image.....	6
1.3 Goal.....	10
1.3.1 The Clinical Problem	10
1.3.2 Recent Research on Quantitative Ultrasound	10
1.3.3 Goal.....	11
1.4 Thesis Structure	12
Chapter 2: Parameter Extraction Methods.....	13
2.1 Image Statistics	13
2.1.1 Tissue Ultrasound Signal to Noise Ratio	13
2.1.2 Rayleigh Distribution.....	14
2.1.3 Experimental Result for Prostate and Phantom	16
2.1.4 Signal to Noise Ratio Based on Split-spectrum.....	22
2.2 Image Texture	26
2.2.1 Co-occurrence Matrix	26
2.2.2 Features Based On Co-occurrence Matrix	27

2.3 Spectral Analysis of Radio Frequency (RF)	29
2.3.1 Average Power Spectra Measured from Tissue and Phantom.....	32
2.3.2 Backscatter Coefficient of Reference Phantom	34
2.3.3 Tissue Backscatter Coefficient as a Function of Frequency.....	34
Chapter 3: Evaluation Methods	37
3.1 Correlation	37
3.1.1 Correlation Coefficient	37
3.1.2 Pearson's Product Moment Correlation Coefficient	39
3.1.3 Limitations of the Correlation Tests	41
3.2 t-test	41
3.3 Mahalanobis distance.....	43
3.4 Discriminant Analysis.....	44
3.4.1 Linear Discriminant Analysis	44
3.4.2 Cross-Validation	44
3.4.3 Prior Probabilities	44
3.5 Performance Analysis	45
Chapter 4 System Implementation.....	51
4.1 RF Data Acquire	51
4.2 Saturated-ratio Control Software	53
4.3 PATH Image Composite.....	56
4.4 User Interface Design	58
4.4.1 Building Database.....	60
4.4.2 Loading PATH Image for US Image Automatically	61
4.4.3 Locating the ROI Between the US and the PATH Image	62
4.4.4 GUI Usage	64
Chapter 5: Results	65
5.1 Case Material	65
5.2 Features Calculated.....	65
5.3 Feature Analysis	66

5.3.1 t-test	66
5.3.2 Correlation	69
5.3.3 Mahalanobis Distance	70
5.4 Classification Result	73
5.5 Parametric Image	79
Chapter 6 Conclusions	82
6.1 Summary	82
6.2 Possible Future Work.....	83
References.....	84
Appendix A: Database Structure	87
Appendix B: Flowchart of GUI Usage	88
Appendix C: Bias Caused by ROI Size	89
Appendix D: Backscatter Coefficient of Reference Phantom	90
Appendix E: Phase Shifting with the Hilbert Transform.....	91

List of Tables

Table 1: Signal to noise ratio values for sub-regions of a tissue mimicking calibration phantom. Where L means low band, H means high band, and N means normal.	25
Table 2: Haralick's texture parameters	29
Table 3: Characterizations of Pearson r	40
Table 4: Characterizations of Az	48
Table 5: Case materials	65
Table 6: List of features	66
Table 7: Results for the mean, standard deviation and t-test	67
Table 8: Correlation matrix of the eight candidate features	69
Table 9: Mahalanobis distance of each of the eight features	70
Table 10: Mahalanobis distance of two features combination.....	72
Table 11: Mahalanobis distance of three features combination.....	72
Table 12: Performance of the two-feature combinations.....	73
Table 13: Performance of the three-feature combinations.....	76
Table 14: Table structure – patient	87
Table 15: Table structure – roiInf	87
Table 16: Bias caused by ROI size	89

List of Figures

Figure 1: Male organs [Cap 2001]	2
Figure 2: Ultrasound unit [NCSU 2001].....	5
Figure 3: The RF signal of a single A-line	6
Figure 4: FFT result of a single A-line	7
Figure 5: The implementation of Hilbert transform in computer	8
Figure 6: Ultrasound image of prostate	9
Figure 7: Histogram of envelope values from phantom shown in Figure 9	18
Figure 8: Probability distribution of phantom envelope	18
Figure 9: Signal to noise ratio values for sub-regions of a tissue mimicking calibration phantom. Average value for the four regions is 1.893.....	19
Figure 10: Histogram of envelope values from prostate shown in Figure 12.....	20
Figure 11: Probability distribution of prostate envelope	20
Figure 12: Signal to noise ratio values for sub-regions of a prostate section (case 18)	21
Figure 13: 17-point Hamming window.....	23
Figure 14: Frequency response of high-pass filter.....	24
Figure 15: Frequency response of low-pass filter.....	24
Figure 16: B-mode images of data used for calculating the backscatter coefficient ..	31
Figure 17: Average power spectrum measured from tissue.....	33
Figure 18: Average power spectrum measured from phantom.....	33
Figure 19: Backscatter coefficient of reference phantom	34
Figure 20: Tissue backscatter coefficient	35
Figure 21: Backscatter coefficient in decibel format.....	35
Figure 22: Tissue backscatter intensity vs. frequency	36
Figure 23: Scatter plots of different types of correlations (a) Positive correlation (b) Negative correlation (c) No correlation (d) Moderate positive correlation	38
Figure 24: Deference between means [Trochim 2001].....	42
Figure 25: The binormal model for ROC analysis [Frederick 2000].....	46

Figure 26: Two normal distributions with 10 different decision thresholds L1, L2, ... L10 [ROC 2001]	47
Figure 27: ROC curve [ROC 2001]	48
Figure 28: A sample Receiver Operating Characteristic (ROC) curve.....	50
Figure 29: In vitro experimental scan setup.....	52
Figure 30: Pad and glue	52
Figure 31: Saturated control – before adjustment.....	54
Figure 32: Saturated control – after adjustment.....	55
Figure 33: Pathology quarter sections with CA marked.....	57
Figure 34: Quarter sections assembled into whole slice.....	57
Figure 35: Graphic user interface	59
Figure 36: Mapping the ROI between pathology and ultrasound images	63
Figure 38: ROC curves of two-feature combination.....	74
Figure 39: Scatter plot of the ENT and SNR	75
Figure 40: Scatter plot of the ENT and COR.....	75
Figure 41: ROC curves of three-feature combination.....	77
Figure 42: 3D scatter plot of ENT, SNR and slope	78
Figure 43: 3D scatter plot of ENT, SNR and intercept.....	78
Figure 44: Parametric image of the prostate (case 48, slice 11) using backscatter slope feature with 5 mm x 12 RF vector regions of interest (ROI) with various degrees of overlap of the regions of interest.	81
Figure 45: Flowchart of GUI usage	88

Chapter 1 Introduction and Background

1.1 Prostate Cancer

Prostate cancer is second only to lung cancer as the cause of cancer deaths among American men. All men are at risk for developing prostate cancer, and as a man ages, his risk of developing prostate cancer increases. Early detection of prostate cancer can dramatically reduce morbidity. Convenient, noninvasive methods of prostate cancer detection have the potential of improving early detection and reducing death rates.

1.1.1 Introduction

The prostate is an organ that is only present in men. It lies just inferior to the urinary bladder, which is shown in Figure 1. It is a chestnut-shaped organ that surrounds the beginning of the urethra. It is composed of 30 to 50 compound tubuloalveolar glands between which is the fibromuscular stroma. These glands secrete a milky fluid during ejaculation that contributes to semen. The prostate no longer serves its main purpose when fathering children is no longer a goal.

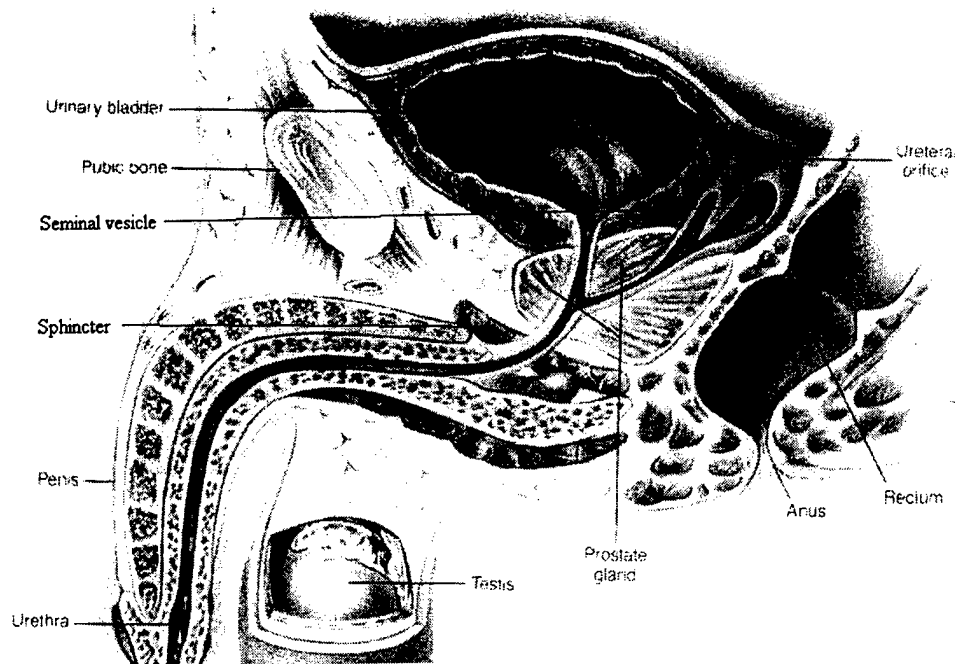


Figure 1: Male organs [Cap 2001]

1.1.2 What is Prostate Cancer?

Because the prostate is wrapped tightly around the urethra, any enlargement can cause the flow of urine to be restricted. This often happens as men get older. It may be due to a condition known as Benign Prostatic Hyperplasia (BPH). BPH is not cancer. However, enlargement of the prostate may also be caused by cancer. Prostate adenocarcinoma is a malignant transformation and growth of the glandular component of the prostate. This tumor can spread beyond the capsule termed capsular penetration, to the seminal vesicles which are glands located next to the prostate and below the bladder, or to the lymph nodes which filter the clear fluid draining from the prostate. The most common site of distant spread is to bone [Cap 2001].

1.1.3 Cause of Prostate Cancer

The cause of prostate cancer is presently unknown. But the risk of getting prostate cancer has been shown to vary with several factors [Prostate 2001]:

Age: Below the age of 40, the risk of prostate cancer is extremely low. After the age of 50, the chance of getting prostate cancer increases rapidly with age. Three-quarters of all men with prostate cancer are over the age of 65.

Race: Studies in America have shown African American men are twice as likely to develop prostate cancer as white men.

Family History: Other members of the family having been diagnosed with prostate cancer increases the risk by 2 or 3 times, particularly if they were diagnosed with the disease at a young age or there have been several members of the family diagnosed with the disease.

Diet: American studies have shown that a diet high in animal (saturated) fat may double the risk of getting prostate cancer.

1.1.4 PSA

Prostate specific antigen (PSA) [PROAC 2001] is an enzyme that is released into the bloodstream by both normal and cancerous prostate cells. Any condition that could cause injury or irritation to the prostate gland such as infection (prostatitis) or noncancerous enlargement of the prostate (BPH) can cause elevation of PSA. However, the possibility of cancer is higher with an elevated PSA. A PSA count of above 4.0ng/ml is usually considered elevated.

1.2 Introduction to Ultrasound

1.2.1 Introduction

By convention, the limit of human hearing is normally taken to be 20kHz (the unit Hz means one cycle per second). Vibrations with frequencies above 20kHz are said to be ultrasonic. In fact, medical ultrasound uses frequencies much higher than this. Typically, the range 2 – 10 MHz is used for medical ultrasonic scanners.

Ultrasound waves are usually elastic compression waves, particularly in liquid or semi-liquid materials, such as soft-tissue organs. As the ultrasound wave propagates through the target, it will interact differently with different types of tissue or matter. The interaction depends on the acoustic properties of the tissue, such as the attenuation, absorption and scattering, impedance and velocity. The acoustic parameters depend strongly on the frequency of the ultrasound, as well as other parameters such as temperature. The values for the speed of ultrasound waves in different soft tissues are very similar. On modern scanners, it is assumed that the value is 1540m/s, which is a reasonable approximation in most cases [Lerski 1988]. Ultrasound does not penetrate through hard tissue, such as bone, very well and as a result, the scanning of bones is not routinely used in medical ultrasound.

1.2.2 Ultrasound System

There are numerous types of ultrasound systems. Conventional sonographic units are comprised of a transducer, pulse generator, demodulator, amplifier, time gain compensator, digital scan converter, memory storage, image processing, and a display. More complex ultrasound systems may also have Doppler, color flow, or other electronic features. Figure 2 is a simplified representation of ultrasound unit.

The following is a simplified explanation of the ultrasound system. A more detailed description of medical ultrasound can be found in [NCSU 2001]. The transducer (a

piezoelectric crystal) works to both send very high frequency sound waves and receive their echoes from the target. When sending the sound, the piezoelectric crystal vibrates in response to voltage changes applied to it. This converts electrical energy into mechanical sound wave energy and introduces motion in the adjacent medium (solid, liquid, or gas). These sound waves are transmitted through the target and reflected at some of the boundaries. A reflected sound wave will travel back and strike the piezoelectric crystal. The crystal will vibrate, and this mechanical stress will cause it to output a voltage proportional to the stress. These voltage changes are then sent to amplifiers, filters, and other electronic hardware so that the computer display can display data for viewing.

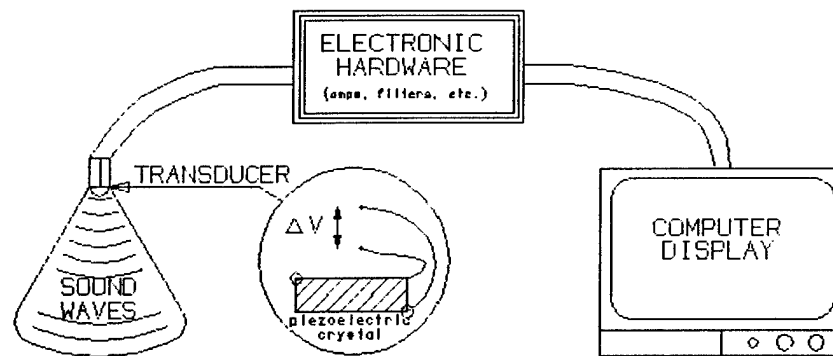


Figure 2: Ultrasound unit [NCSU 2001]

1.2.3 Medical Ultrasound

Ultrasound has proven to be a very valuable and cost-effective complementary medical imaging method, along with CT (Computed Tomography) and MRI (Magnetic Resonance Imaging). Ultrasound tissue characterization techniques are often based on the premise that disease processes alter physical characteristics of

tissue and that these alterations can cause observable changes in acoustic scattering properties [Lizzi 1986].

1.2.4 Ultrasound Image

To investigate quantitative sonographic characterization, it is important to convert the radio frequency (RF) data into image. The two-dimensional B-mode ultrasound images, as shown in Figure 6, are formed by combining data derived from a series of one-dimensional A-line scans. Each A-line scan is the backscattered RF signal recorded at a single transducer location resulting from the transmitted pressure wave reflecting from scattering sites within the object being scanned.

One A-line scan and its FFT result are shown in Figure 3 and 4. The ultrasound transmit pulse has a 5 MHz center frequency.

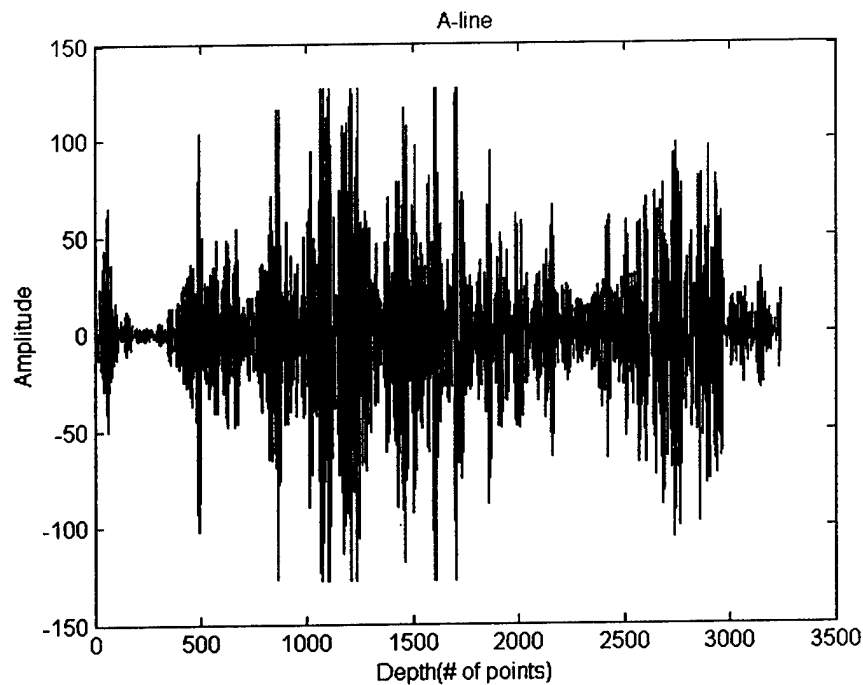


Figure 3: The RF signal of a single A-line

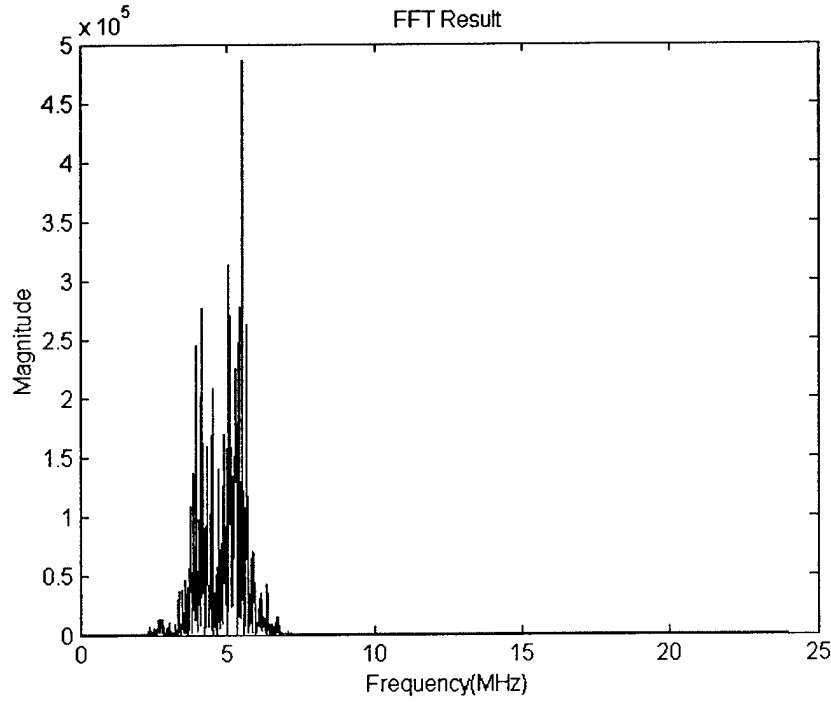


Figure 4: FFT result of a single A-line

An image of the underlying tissue properties can be formed by combining the return signals from a sequence of A-line scans at different lateral positions. In order to create an image, that is recognizable by the human eye, the data are often processed to form an image called B-mode image. To get the standard B-mode ultrasound image, the envelope of the RF signal needs to be found. This is accomplished by using the Hilbert transform [Mohanty 1987].

The Hilbert transform is defined as

$$\begin{aligned}\hat{x}(t) &= \frac{1}{\pi} \otimes x(t) \\ &= \frac{1}{\pi} \int_{-\infty}^{\infty} \frac{x(\tau)}{t - \tau} d\tau\end{aligned}\tag{1.1}$$

The Hilbert transform produces a sequence that is the input data with a 90° phase shift (i.e., sines become cosines and vice versa). The details can be found in Appendix E. Figure 5 shows how to realize the Hilbert transformation in a computer with digital data.

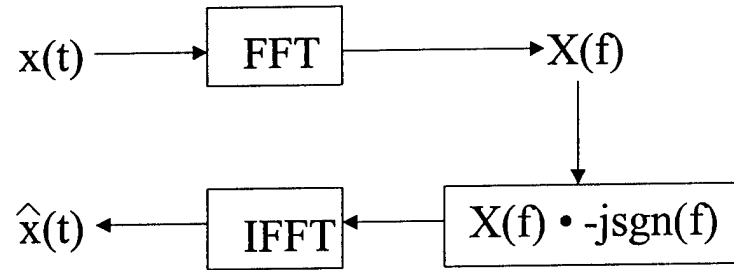


Figure 5: The implementation of Hilbert transform in computer

The Hilbert transform shifts the phase and is therefore called a quadrature filter. A signal $z(t)$ is called an analytic signal if

$$z(t) = x(t) + i\hat{x}(t) \quad (1.2)$$

where $\hat{x}(t)$ is the Hilbert transform of $x(t)$. If $x(t) = A\cos(\omega t + \phi)$, then

$$\hat{x}(t) = A\sin(\omega t + \phi) \text{ and } z(t) = e^{i(\omega t + \phi)}.$$

The envelope of the RF signal can then be computed by taking the magnitude of the complex sequence.

$$V = \sqrt{I^2 + Q^2} \quad (1.3)$$

where V is the envelope of the RF signal. I is a real input sequence which is the original data. Q is the imaginary part which is the actual Hilbert transform. The imaginary part is a version of the original real sequence with a 90° phase shift. This method was used to compute the envelope of the RF signal in Figure 3. The amplitude of the envelope-detected signal, represented by brightness, is displayed in a standard B-mode ultrasound image. See Figure 6. It should be noted that the B-mode image is useful for certain applications, it does not contain all of the original ultrasound information. Other signal processing and image representation modes are also very useful in medical ultrasound.



Figure 6: Ultrasound image of prostate

1.3 Goal

1.3.1 The Clinical Problem

The problem of finding an accurate method for the detection and staging of adenocarcinoma of the prostate (ACP) is one of the outstanding challenges in the field of diagnostic medicine. The principal methods used to detect and confirm the presence of the ACP are digital rectal examination (DRE), the serum Prostatic Specific Antigen assay (PSA), and transrectal-ultrasound-guided (TRUS) prostatic biopsy.

Unfortunately, current individual diagnostic imaging and laboratory tests for the detection and staging of ACP perform poorly. The PSA test now plays a central role in screening for ACP because it is inexpensive and relatively sensitive. The problem is that there is considerable overlap between PSA values for patients with cancer and those with no cancer, especially for the group of older males with benign prostatic hypertrophy (BPH). For this reason, an elevated PSA must be followed by a confirmatory test. The DRE and TRUS alone have proven to be insufficiently sensitive to be used either as screening studies or as studies that can reliably guide a prostate biopsy in a patient with an elevated PSA [Garra 1998]. At present, most clinicians do not consider TRUS imaging to be adequate for detecting suspicious regions. It is considered to be inadequate because its sensitivity is not sufficient to reveal the presence of cancer and to direct a biopsy needle to the cancer site [Feleppa 1996]. One ultimate goal of this research would be to create a system that can reliably direct a biopsy needle to sites that are likely to be cancerous.

1.3.2 Recent Research on Quantitative Ultrasound

Because of the limitations of the conventional methods in this field, a number of investigators are using quantitative techniques to offer improved sensitivity and specificity for prostate cancer. Feleppa et al. [Feleppa 1996] used quantitative

ultrasonic radio frequency (RF) spectral features and elementary discriminant functions to discriminate cancerous from noncancerous prostate tissue. Feleppa et al. [Feleppa 1997] reported a value of A_z of 0.79 ± 0.07 when using their RF features to make the discrimination between cancerous and noncancerous tissue, and a value of A_z of 0.60 ± 0.21 from clinical interpretation of the conventional images. And improved results using RF features have been achieved in Feleppa's recent study [Feleppa 2001]. The work of Feleppa et al. is limited to the microscopic features. Huynen et al. [Huynen 1994] investigated the discriminating power of macroscopic features from ultrasonic image texture. Ophir and colleagues [Ophir 1997] have recently measured the elastogram for human prostate tissue in vitro. The elastogram is a display of tissue hardness deduced from the local tissue strain that occurs in response to an externally applied static compression. It has been shown to be useful in the characterization of malignant breast tumors that are harder than benign lesions [Garra 1997], and is expected to be useful in prostate cancer detection since prostatic malignancies are also often "hard" on palpation.

1.3.3 Goal

The history of developments in the field of quantitative analysis of ultrasound and elastogram features strongly suggests that investigators turn their attention to an analysis of an optimal combination of the microscopic RF features, the macroscopic image texture features, and measures of tissue hardness derived from the elastogram.

So the ultimate goal of this project is to combine features derived from ultrasound (US) images, US radio-frequency (RF) data, tissue elasticity imaging, and clinical data such as PSA into a computerized system for displaying prostate images that indicate probable locations of cancer [Garra 2000]. Only features derived from US images and RF data are used to discriminate cancerous from noncancerous prostate tissue in the study of this thesis.

1.4 Thesis Structure

This thesis is organized as follows: Chapter 2 introduces the features used in this research, which come from ultrasound images and ultrasound radio-frequency data. Chapter 3 outlines the evaluation methods, which include correlation, t-test, Mahalanobis distance, discriminant analysis and performance evaluation. Chapter 4 develops a MATLAB-based tool, with which we can draw Region of Interest (ROI) on a pathology image to get the corresponding data in the ultrasound radio-frequency data sets and compute the corresponding US features for the chosen ROI. In Chapter 5, all the evaluation methods introduced in Chapter 3 will be applied to the data acquired via the feature computation software developed in Chapter 4. Finally, Chapter 6 summarizes the conclusions reached in the thesis, as well as suggesting future directions of research.

Chapter 2: Parameter Extraction Methods

US data can be processed in a wide variety of methods. The availability of modern digital signal processing hardware and software opens up the possibility of an excess of available signal processing techniques. A major goal of this project is to determine the most suitable signal processing techniques for discriminating prostate cancer. Following a series of discussions with experienced medical ultrasound investigators [Garra 1993, Wagner 1983, Wear 1995], a set of eight features was chosen for further investigation. This choice was based on a combination of the ability of these features to work on the detection of cancer in other organs and by an understanding of the underlying physical mechanisms. The choice of features were the basic texture feature – envelope signal-to-noise ratio (SNR), four features coming from the co-occurrence matrix and three features coming from spectral analysis of RF echo signals. The following is a description of the signal processing algorithm associated with each feature and the underlying rationale for use.

2.1 Image Statistics

There are many features based on the first-order statistics. Tissue ultrasound Signal to Noise Ratio (SNR) was chosen in our study. This may be useful because it may be another way to measure the relative contribution of specular vs. diffuse tissue backscatter components. These have been previously shown to be of value for characterization of both liver and kidney tissue [Garra 1989, Garra 1994].

2.1.1 Tissue Ultrasound Signal to Noise Ratio

$$SNR = \mu / \sigma \quad (2.1)$$

with

$$\mu = \frac{1}{n} \sum_{x,y} f(x,y)$$

$$\sigma = \sqrt{\frac{1}{n} \sum_{x,y} (f(x,y) - \mu)^2}$$

where μ is mean gray level, an indicator of average tone of the image. σ is variance of gray level, an indicator of how much variation exists in the image with respect to the average tone. n is the total number of pixels, and $f(x,y)$ is the gray level in pixel (x,y) .

2.1.2 Rayleigh Distribution

The probability distribution of a narrow band noise process $n(t)$ can be derived by considering a complex phasor

$$n(t) = r(t) \exp(j\varphi(t)) \quad (2.2)$$

where $r(t)$ is the magnitude or envelope and $\varphi(t)$ is the phase. This can also be written in terms of its real and imaginary parts (in-phase and quadrature components) as

$$n(t) = x(t) + jy(t)$$

$$x(t) = r(t) \cos(\varphi(t))$$

$$y(t) = r(t) \sin(\varphi(t))$$

If both random processes $x(t)$ and $y(t)$ are Gaussian distributed with the same variance and zero mean then the probability density functions $P(x)$ and $P(y)$ are given by

$$P(x) = \left(\frac{1}{2\pi\sigma^2}\right)^{\frac{1}{2}} \exp\left(\frac{-x^2}{2\sigma^2}\right)$$

$$P(y) = \left(\frac{1}{2\pi\sigma^2}\right)^{\frac{1}{2}} \exp\left(\frac{-y^2}{2\sigma^2}\right)$$

Assuming x and y are statistically independent then

$$\begin{aligned} P(x, y) &= P(x)P(y) \\ &= \frac{1}{2\pi\sigma^2} \exp\left(\frac{-(x^2 + y^2)}{2\sigma^2}\right) \end{aligned} \quad (2.3)$$

Transforming differential areas using

$$dxdy = r dr d\phi$$

Gives the joint probability density function as

$$P(r, \phi) = \frac{r}{2\pi\sigma^2} \exp\left(-\frac{r^2}{2\sigma^2}\right) \quad (2.4)$$

Since this is independent of phase the random variables r and ϕ are statistically independent and therefore

$$P(r, \phi) = P(r)P(\phi)$$

Then

$$P(\varphi) = \int_0^{\infty} P(r, \varphi) dr \quad \text{for } 0 \leq \varphi \leq 2\pi \quad (2.5)$$

$$= \frac{1}{2\pi}$$

$$P(r) = \int_0^{2\pi} P(r, \varphi) d\varphi \quad \text{for } r \geq 0 \quad (2.6)$$

$$= \frac{r}{\sigma^2} \exp\left(-\frac{r^2}{2\sigma^2}\right)$$

This is normally called the Rayleigh Distribution [Bourke 2001]. The Rayleigh distribution is a special case of the Weibull distribution [Hahn 1967].

2.1.3 Experimental Result for Prostate and Phantom

In using quantitative techniques to analyze the backscattered RF signal, it is helpful to have a model that relates physical interaction between the ultrasound pulse and the scattering medium to measured quantities derived from the observed signal. The most widely accepted model of ultrasound scattering in soft tissue has been developed by Wagner et al. [Wagner 1986, Wagner 1987]. In this model, the scatterers are divided into three classes. The major two classes are described as follows:

The first class consists of a large number of randomly-located scatterers whose structure is much smaller than the wavelength. When the number of scatterers per resolution cell is sufficiently large and the phases of the complex phasors are randomly distributed between 0 and 2π , then, the real and imaginary parts of the resulting accumulated signal have a circular Gaussian joint pdf given by Equation

(2.3). The pdf of the magnitude signal that is displayed in B-mode images is given by a Rayleigh pdf Equation (2.6).

The second class of tissue scatterers is nonrandomly distributed with long-range order. It contributes a specular backscattered intensity. When these scatterers are present along with the random diffuse scatterers, the resulting magnitude signal is no longer Rayleigh distributed.

From the above discussion, we know a histogram of the gray-scale pixel values for the B-scan image with fully developed speckle will follow a Rayleigh probability density function (pdf). The theoretical value of SNR for Rayleigh statistics is found to be 1.91. [Wagner 1983]. For an image with specular as well as diffuse scatters, the value will be lower, in most instances.

Figure 7 is the histogram of a phantom magnitude image shown in Figure 9. This phantom has predominately small scatters and contains very few specular scatters. The probability distribution of gray level should follow a Rayleigh distribution. Figure 8 shows that it does follow a Rayleigh distribution. It should therefore exhibit a μ/σ value very close to 1.91. Figure 9 demonstrates that sub-regions calculated from within the phantom do in fact exhibit a μ/σ close to 1.91.

Figure 10 shows a histogram of a typical prostate magnitude image. This image is shown in Figure 12 with the calculated signal to noise ratios for several regions of interest in the image. Figure 11 is the probability distribution of this image, which shows substantial non-Rayleigh behavior. This non-Rayleigh behavior is also revealed by the envelope SNR less than 1.91. All the sub-regions have values less than 1.91 and it indicates that the sub-regions contain specular as well as diffuse, randomly positioned scatters. This is an expected result since tissue rarely exhibits purely diffuse scattering. Tests on other sections have yielded similar results.

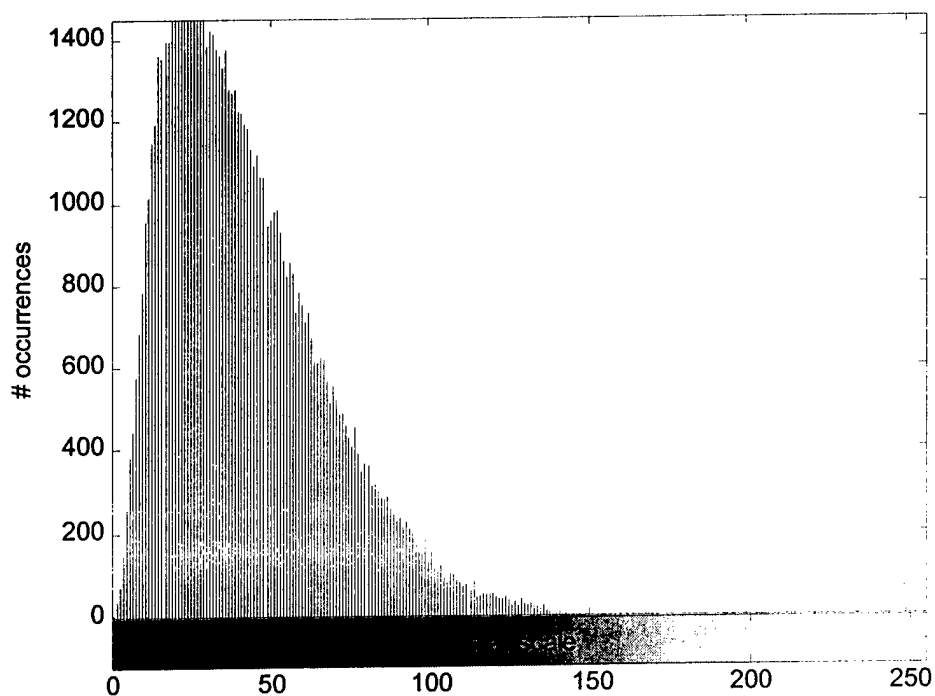


Figure 7: Histogram of envelope values from phantom shown in Figure 9

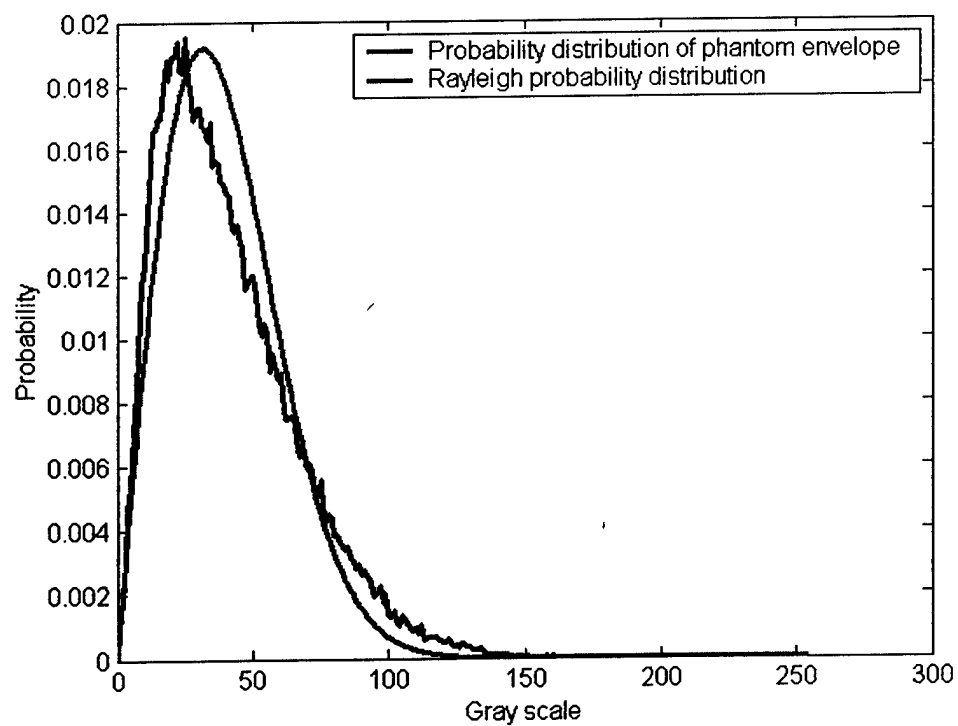


Figure 8: Probability distribution of phantom envelope

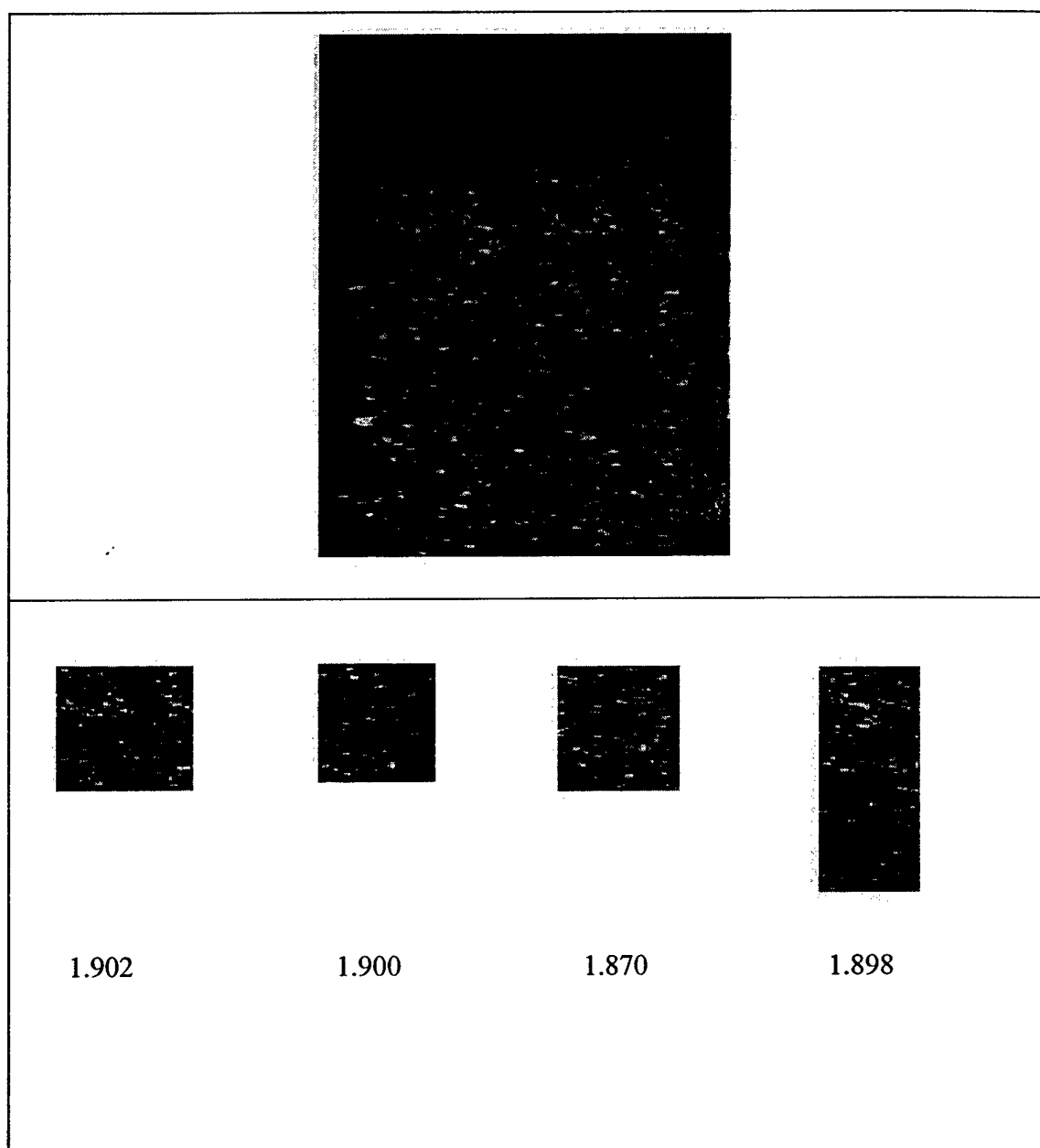


Figure 9: Signal to noise ratio values for sub-regions of a tissue mimicking calibration phantom. Average value for the four regions is 1.893.

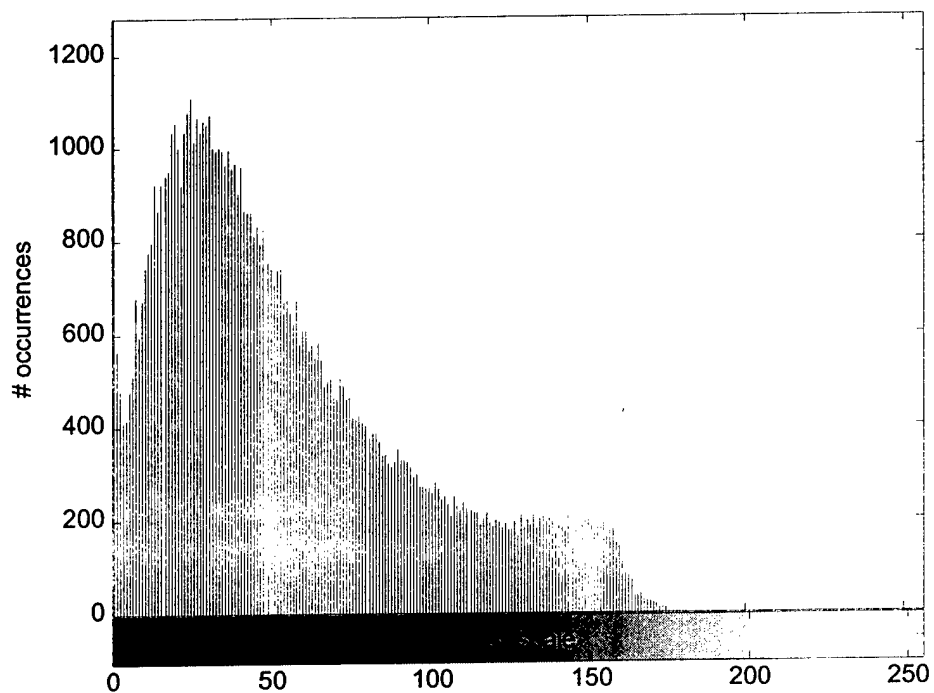


Figure 10: Histogram of envelope values from prostate shown in Figure 12

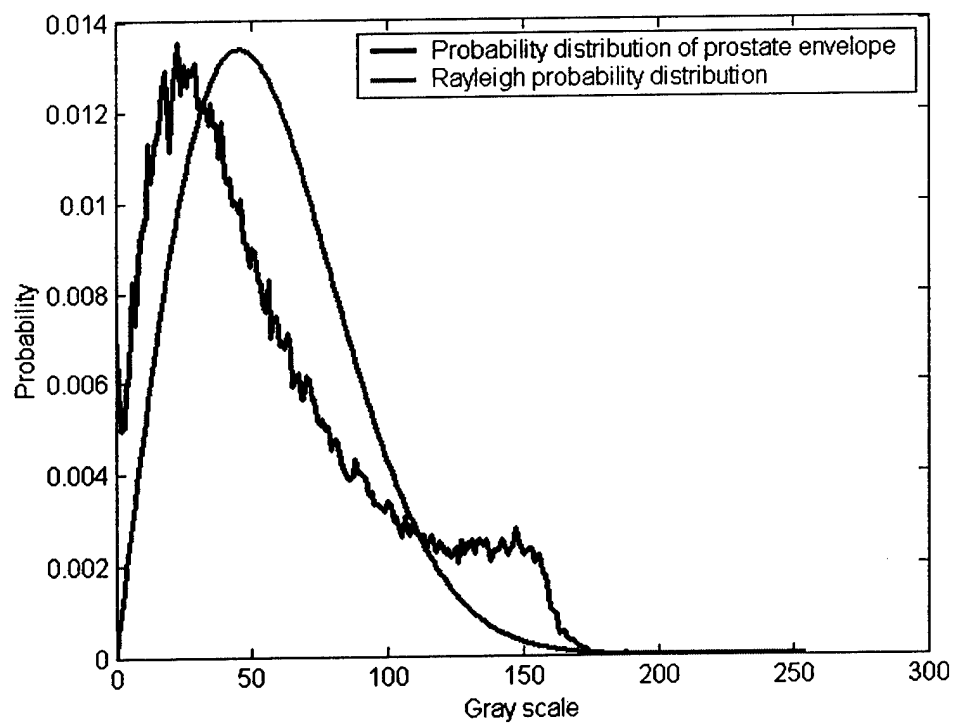


Figure 11: Probability distribution of prostate envelope

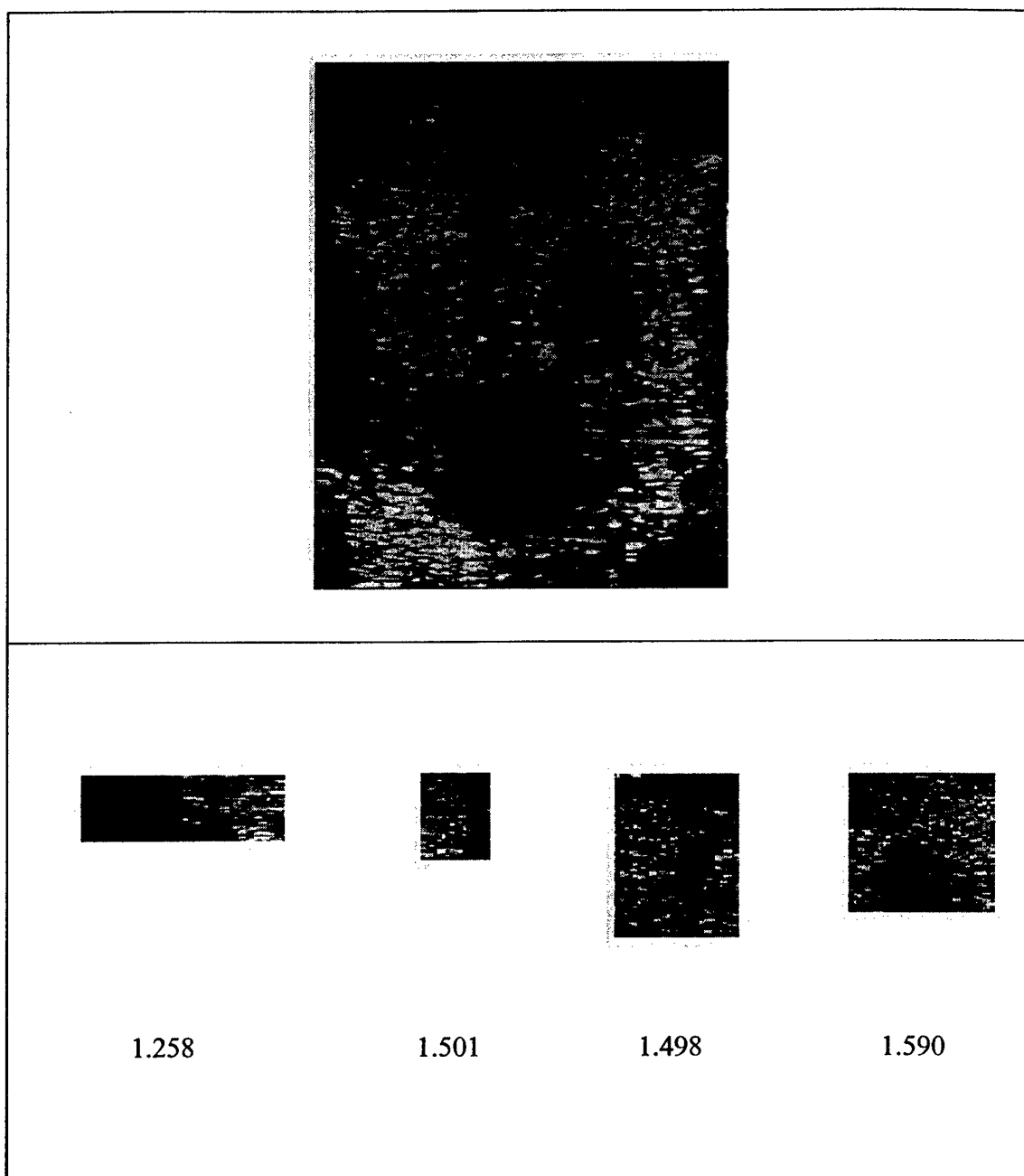


Figure 12: Signal to noise ratio values for sub-regions of a prostate section (case 18)

2.1.4 Signal-to-Noise Ratio Based on Split-spectrum

Based on the suggestion from Dr. Keith A. Wear and Dr. Robert F. Wager, we tried to split the spectrum to calculate the signal to noise ratio (SNR) for the high band and low band separately. When we use the phantom data as the input, the result should also be close to 1.91.

To calculate the SNR based on split-spectrum, there are several steps to finish this task:

- 1) Get the complex (Real, Imaginary) FFT of the trace of interest (from a given ROI).
- 2) Split the spectrum into two parts – higher band and lower band.
- 3) Take the IFFT of the complex data set from each band.
- 4) Detect envelope of each signal and get μ/σ as before.

The most important step is how to split the spectrum into two halves. As shown before, the center frequency is 5MHz, and the sampling frequency is 48MHz. We can use the following formula to change the center frequency into Nyquist frequency.

$$f_N = \frac{f_c}{0.5 \times f_s} = \frac{5M}{0.5 \times 48M} = 0.2083 \quad (2.7)$$

where f_N is the center frequency in Nyquist frequency. f_c is the center frequency, and f_s is the sampling frequency.

High-pass and low-pass filters are needed to split the spectrum. It might be natural to use the center frequency as the cut-off frequency to devise the filters. But an abrupt truncation will introduce “ringing” artifacts when we do the IFFT. So we want the window for the upper half and the window for the lower half to overlap. The Hamming window [MATLAB 2000] was used to devise the high-pass and low-pass filters. We use cut-off frequency 0.1883 to devise the high-pass filter and 0.2283 for

low-pass filter. The coefficients of a Hamming window are computed from the following equation.

$$w[k+1] = 0.54 - 0.46 \cos(2\pi \frac{k}{n-1}), \quad k = 0, \dots, n-1 \quad (2.8)$$

Figure 13 shows the 17-point Hamming window used in this research.

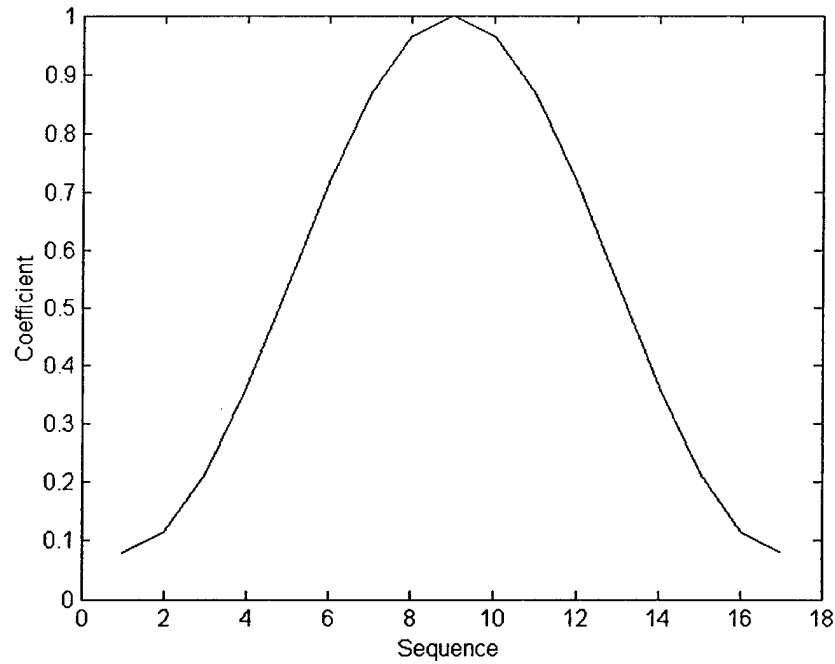


Figure 13: 17-point Hamming window

Figure 14 shows the frequency response of the high-pass filter. Figure 15 shows the frequency response of the low-pass filter.

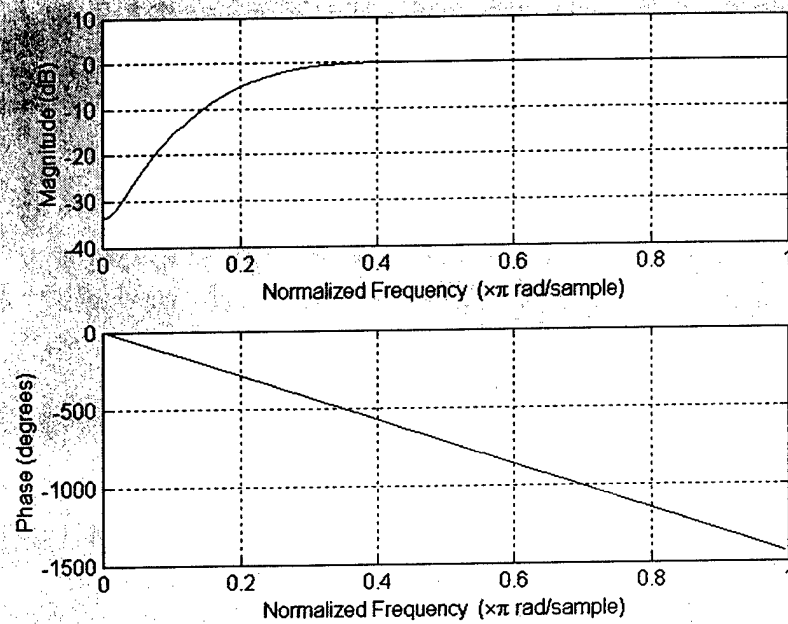


Figure 14: Frequency response of high-pass filter

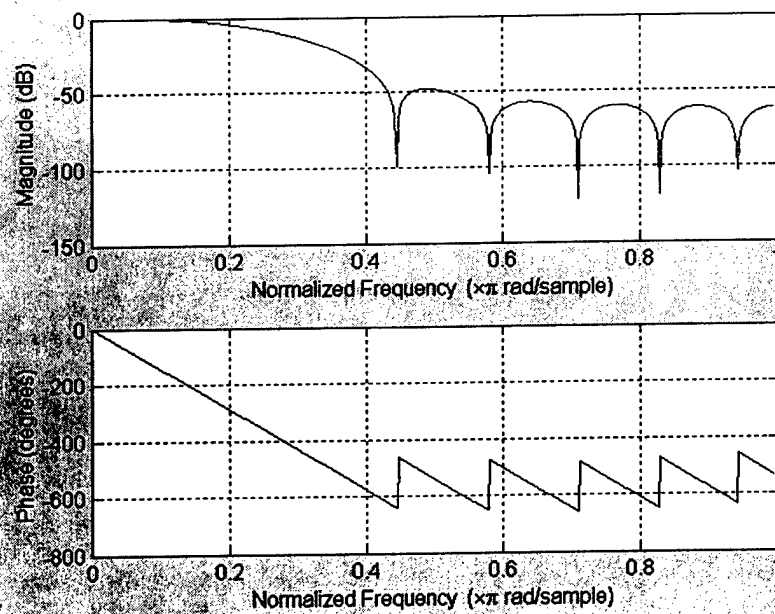


Figure 15: Frequency response of low-pass filter

When we split the spectrum, the bandwidth for each half clearly becomes smaller than for the full bandwidth case. Since the size of the resolution cell is inversely proportional to the bandwidth, the resolution cell for the split cases will be larger than the original. Therefore, there should be an even better chance that the SNR will be closer to 1.91 than originally. The more scatters per resolution cell – all else being equal – the closer the SNR will be to 1.91. We have randomly chosen five ROIs in one phantom image and calculated the SNR of lower band, higher band and the normal SNR. The results are shown in Table 1. The average value for the SNR generated from the lower band data set is 1.899 and 1.909 for the higher band data set and 2.101 for the normal. This demonstrates that the SNR values generated from the lower band and higher band data set are closer to 1.91 than the SNR value generated via normal way.

	SNR _L	SNR _H	SNR _N
ROI 1	1.910	1.876	2.132
ROI 2	1.957	1.965	2.052
ROI 3	1.846	1.823	2.119
ROI 4	1.905	1.923	2.079
ROI 5	1.879	1.956	2.127
Average Value	1.899	1.909	2.102

Table 1: Signal to noise ratio values for sub-regions of a tissue mimicking calibration phantom. Where L means low band, H means high band, and N means normal.

2.2 Image Texture

There are several paradigms for measuring texture mathematically. A commonly used one is based on the gray level co-occurrence matrix (GLCM), also known as the spatial gray level dependence matrix (SGLD) in the literature. It has been categorized as an efficient approach to texture analysis [Frederick 2000, Garra 1993]. Using this approach representative texture features can be measured to characterize the property of each region of interest (ROI). Features based on the co-occurrence matrix have already been demonstrated to be valuable for prostatic cancer [Huynen 1994].

2.2.1 Co-occurrence Matrix

The first step in computing the co-occurrence matrix is to demodulate the radio frequency (RF) signal to produce an envelope-detected image. This is accomplished by using the Hilbert transform. Details can be found in Chapter 1. The Hilbert transform shifts the input data with a 90° phase. The envelope of the RF can then be computed by taking the magnitude of the original and 90° phase shift time sequences.

Then the next step is to compute the co-occurrence matrix, C . This is an $N \times N$ matrix where N is the number of the gray levels. Each of the elements of C , c_{ij} , takes on a value that is the number of times a pixel has the value i , and its “neighbor” pixel has the value j . The neighbor pixel is defined as being of a given radial distance of pixels d at angle θ . The values in the matrix are then normalized to represent probabilities of specific gray level combination. Different co-occurrence matrices can be constructed by changing the direction and distance between pixel pairs when defining spatial relationships. The co-occurrence matrix for distance d and angle θ and N possible gray level values can be found from Equation 2.9.

$$GLCM = \begin{bmatrix} p_{d,\theta}(0,0) & p_{d,\theta}(0,1) & \cdots & \cdots & \cdots & p_{d,\theta}(0,N) \\ p_{d,\theta}(1,0) & p_{d,\theta}(1,1) & \cdots & \cdots & \cdots & p_{d,\theta}(1,N) \\ \vdots & \vdots & \ddots & & & \vdots \\ \vdots & \vdots & & \ddots & & \vdots \\ \vdots & \vdots & & & \ddots & \vdots \\ p_{d,\theta}(N,0) & p_{d,\theta}(N,1) & \cdots & \cdots & \cdots & p_{d,\theta}(N,N) \end{bmatrix} \quad (2.9)$$

An example is given as following,

$$GLCM = \begin{bmatrix} 0 & 0 & 0 & 1 & 2 \\ 1 & 1 & 0 & 1 & 1 \\ 2 & 2 & 1 & 0 & 0 \\ 1 & 1 & 0 & 2 & 0 \\ 0 & 0 & 1 & 0 & 1 \end{bmatrix} \quad (2.10)$$

This is a matrix of a 5x5 image with only 3 gray levels. The corresponding co-occurrence matrix ($d = 1, \theta = 45^\circ$) is shown in Equation (2.11)

$$C = \begin{bmatrix} 4 & 2 & 0 \\ 2 & 3 & 2 \\ 1 & 2 & 0 \end{bmatrix} \quad (d = 1, \theta = 45^\circ) \quad (2.11)$$

Alternatively the neighbor pixel can be defined as being dx pixels away in the vertical direction and dy pixels away in the lateral direction. The actual values of dx and dy are 5 in this research. Methods for choosing an effective neighbor distance can be found in [Mia 1999].

2.2.2 Features Based On Co-occurrence Matrix

Once the co-occurrence matrix is calculated, parameters that might be useful in distinguishing tissue types can be extracted.

<p>Angular Second Moment (ASM) or Energy:</p> $f_1 = \sum_i \sum_j p(i, j)^2$	<p>An indicator of uniformity or smoothness. Homogeneous textures will have a higher value than inhomogeneous ones because smooth textures have more concentrated densities than rough textures. Rough textures have densities with higher spread or variance.</p>
<p>Contrast (CON) or Difference Moment:</p> $f_2 = \sum_i \sum_j (i - j)^2 p(i, j)$	<p>An indicator of gray level variance and therefore smoothness.</p>
<p>Correlation (COR):</p> $f_3 = \frac{\sum_i \sum_j (ij) p(i, j) - \mu_x \mu_y}{\sigma_x \sigma_y}$	<p>An indicator of underlying structure in a texture. The absolute value of this measure will be large if the image has some sort of structure such as a smooth background or repeated sharp edges over a given region.</p>
<p>Entropy (ENT):</p> $f_4 = -\sum_i \sum_j p(i, j) \log p(i, j)$	<p>An indicator of the amount of information provided by pairwise interactions of image pixels separated by a distance d.</p>
<p>Inverse Difference Moment (IDM):</p>	<p>Emphasizes small changes and subtle</p>

$f_s = \sum_i \sum_j \frac{p(i, j)}{1 + (i - j)^2}$	textures.
Dissimilarity (DIS): $\sum_i \sum_j i - j p(i, j)$	Measures the degree of dissimilarity between pixels.

Table 2: Haralick's texture parameters

The joint probability of gray levels i and j in the direction θ at a distance d is $p(i, j)$. N is the number of gray levels in the digitized image. μ_x and μ_y are means of row and column sums separately. σ_x and σ_y are standard deviations of row and column sums separately.

Many texture measures can be calculated from the co-occurrence matrix. One set of such texture parameters are known as Haralick's texture measures [Frederick 2000]. Some of them are summarized in Table 2. ASM, COR, CON and ENT are chosen from the above listed six features

2.3 Spectral Analysis of Radio Frequency (RF)

Backscatter is the reflection from the scattering sites of the pressure wave back in the direction of the transducer that transmitted the pulse. The ultrasonic backscatter coefficient is a useful parameter that describes the scattering efficiency, as a function of ultrasonic frequency, of a tissue or material. The backscatter coefficient as a function of frequency of the tissue can be used to generate three useful features –

slope, intercept and mid-band value. These features have been successfully used by Feleppa [Feleppa 1996] to differentiate prostatic cancer from benign tissue.

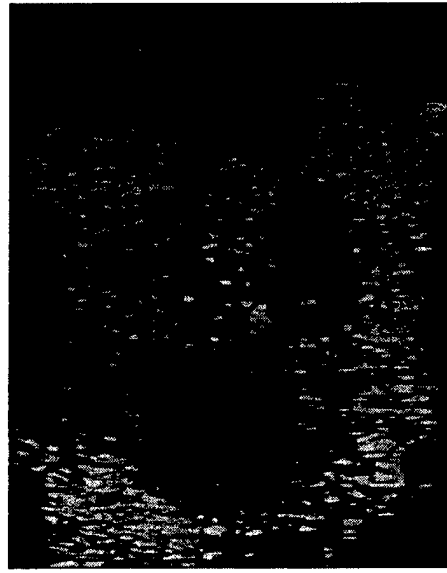
A reference phantom method for measuring ultrasonic backscatter coefficients was used in this study. With the reference phantom method, spectra obtained in tissues are compared with spectra obtained from a phantom with known scattering and attenuation properties. The data were compensated for attenuation due to intervening tissues between the transducer and the ROI.

The formula [Wear 1995] used to compute the tissue backscatter coefficient as a function of frequency $\eta_t(f)$ is

$$\eta_t(f) = \eta_p(f) \frac{S_t(f)}{S_p(f)} \times \exp[-4\alpha_p(f)z + 4\sum_{i=1}^n \alpha_i(f)z_i] \quad (2.12)$$

where $\eta_t(f)$ is tissue backscatter coefficient as a function of frequency. $\eta_p(f)$ is backscatter coefficient of reference phantom. $S_t(f)$ and $S_p(f)$ are average power spectra measured from tissue and phantom, respectively. $\alpha_p(f)$ is reference phantom attenuation coefficient and z is the distance from the transducer to the center of the ROI. In vivo measurements are presumed to involve n tissue layers with attenuation coefficients $\alpha_i(f)$ and thickness z_i .

The reference phantom was a tissue-like slurry containing glass beads and graphite in agar particles suspended in a water-alcohol solution. The attenuation coefficient was 0.57dB/MHz-cm. The phantom used to test the backscatter coefficient measurement method consisted of glass beads embedded in agar. Figure 16(b) is the phantom image.



(a) RF image



(b) Phantom image



(c) ROI on RF

Figure 16: B-mode images of data used for calculating the backscatter coefficient

To simplify the model, the tissue attenuation coefficient $\alpha_t(f)$ was assumed to be constant. A value of 0.5dB/MHz-cm was selected because it is commonly considered to be representative of moderately vascular tissues [Feleppa 1996].

The RF feature is an ROI-based spectral analysis. In order to facilitate the ROI selection, an interactive user-based tool was developed.

Figure 16(a) shows one ultrasound image used in this test. Figure 16(b) shows the corresponding phantom image. And Figure 16(c) is one ROI inside the ultrasound image chosen by user.

2.3.1 Average Power Spectra Measured from Tissue and Phantom

After specifying the ROI on a B-mode image, the RF data samples along each scan-line segment within the ROI were multiplied by a Hamming window. The windowed data were subjected to a fast Fourier transform (FFT), and the squared magnitude of the computed spectrum was derived. Spectral results for all scan line segments within the ROI were averaged to form an estimate of the average power spectrum. The average power spectra measured from tissue $S_t(f)$ and phantom $S_p(f)$ are shown in Figure 17 and Figure 18.

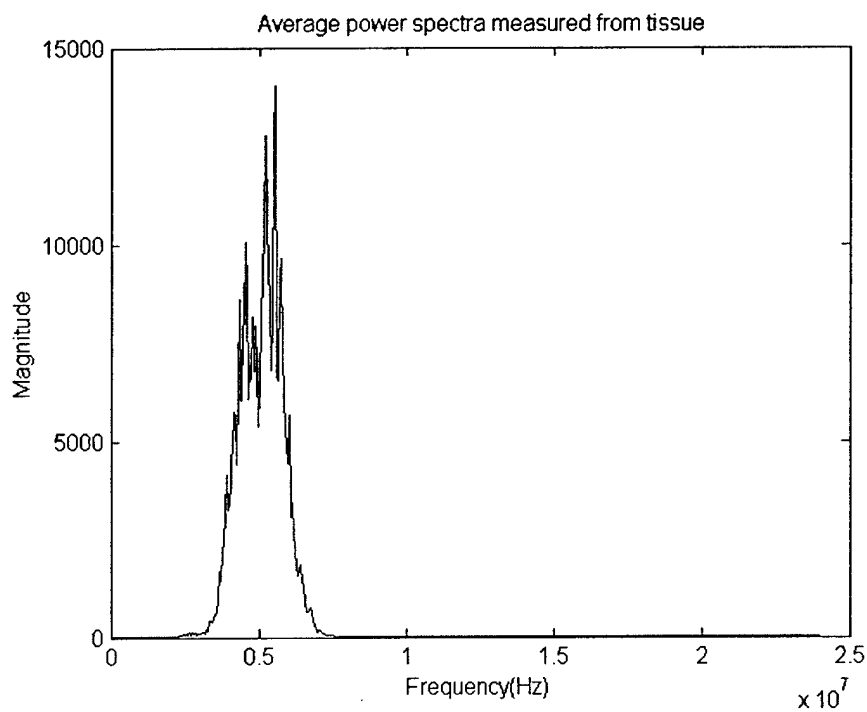


Figure 17: Average power spectrum measured from tissue

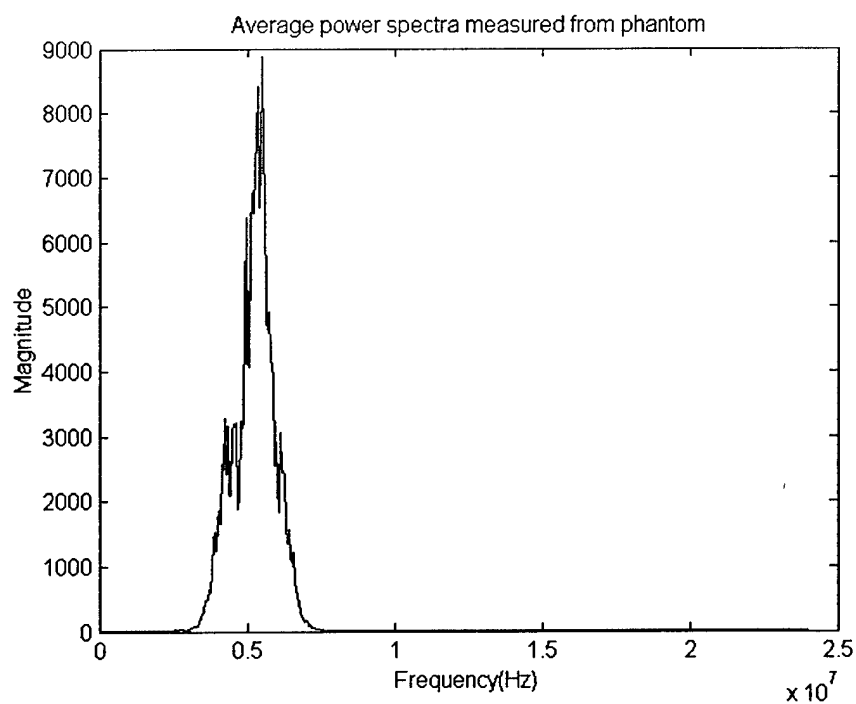


Figure 18: Average power spectrum measured from phantom

2.3.2 Backscatter Coefficient of Reference Phantom

The backscatter coefficient of reference phantom $\eta_p(f)$ is a known number, which is shown in Figure 19 and listed in Appendix D.

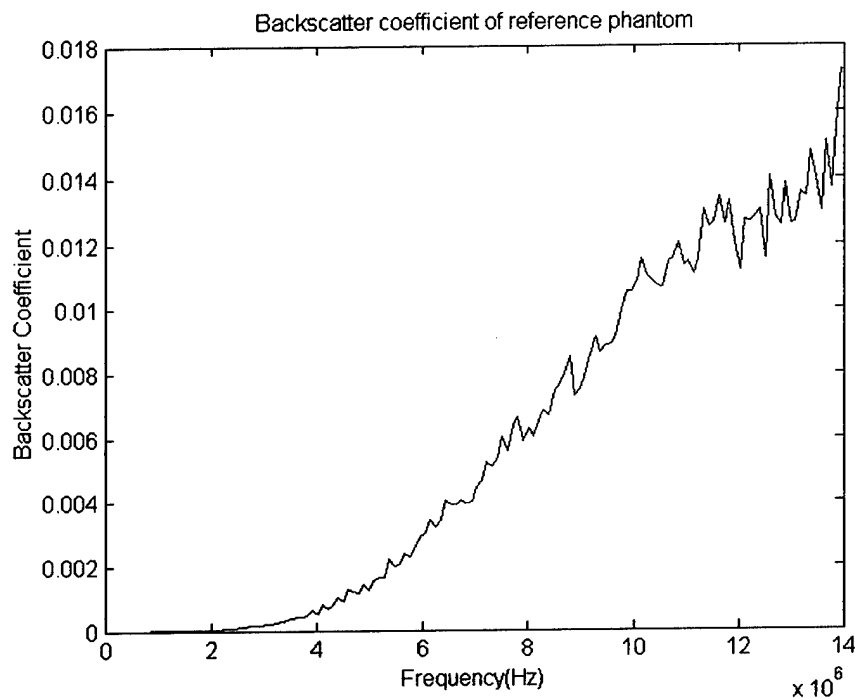


Figure 19: Backscatter coefficient of reference phantom

2.3.3 Tissue Backscatter Coefficient as a Function of Frequency

The tissue backscatter coefficient as a function of frequency $\eta_t(f)$ was calculated by using Equation 2.12 and shown in Figure 20. Then the spectrum was converted to decibel which is shown in Figure 21. Linear regression analysis was applied to compute the intercept, slope and mid-band value (value of the fit at the center frequency) on the decibel format curve. The analysis was performed over the frequency range of 3.0 to 7.0MHz, Figure 22.

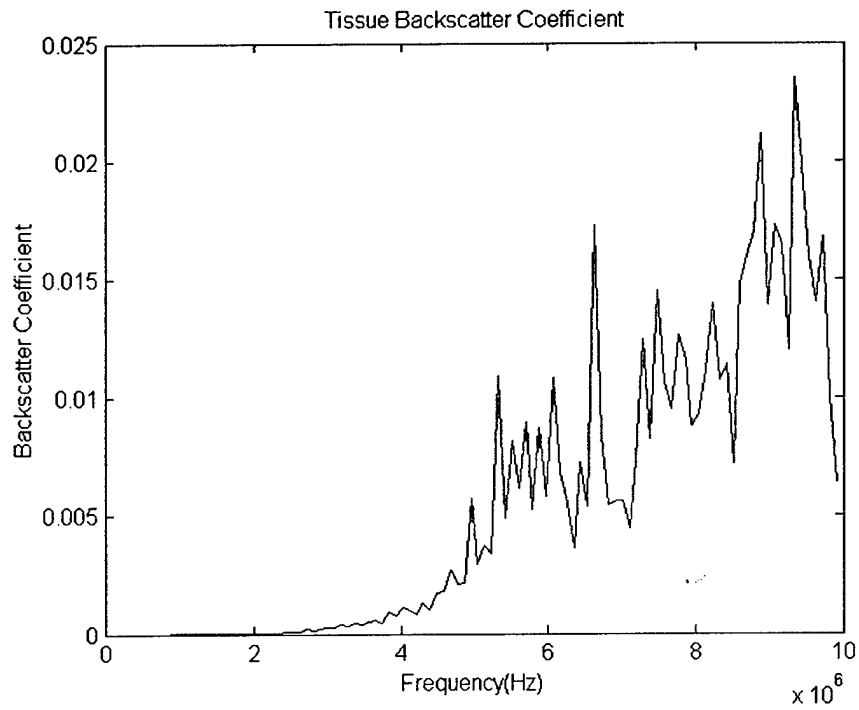


Figure 20: Tissue backscatter coefficient

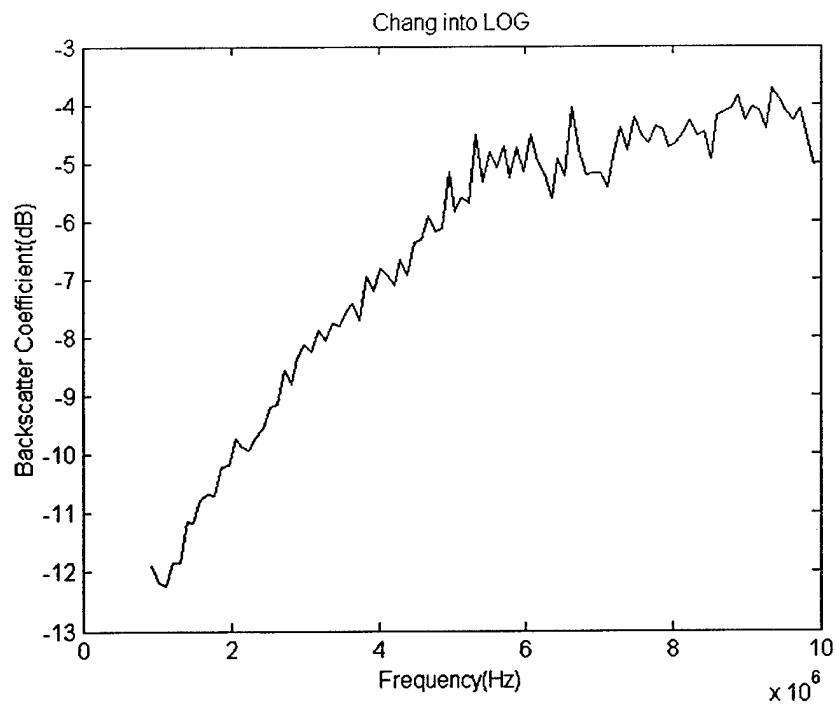


Figure 21: Backscatter coefficient in decibel format

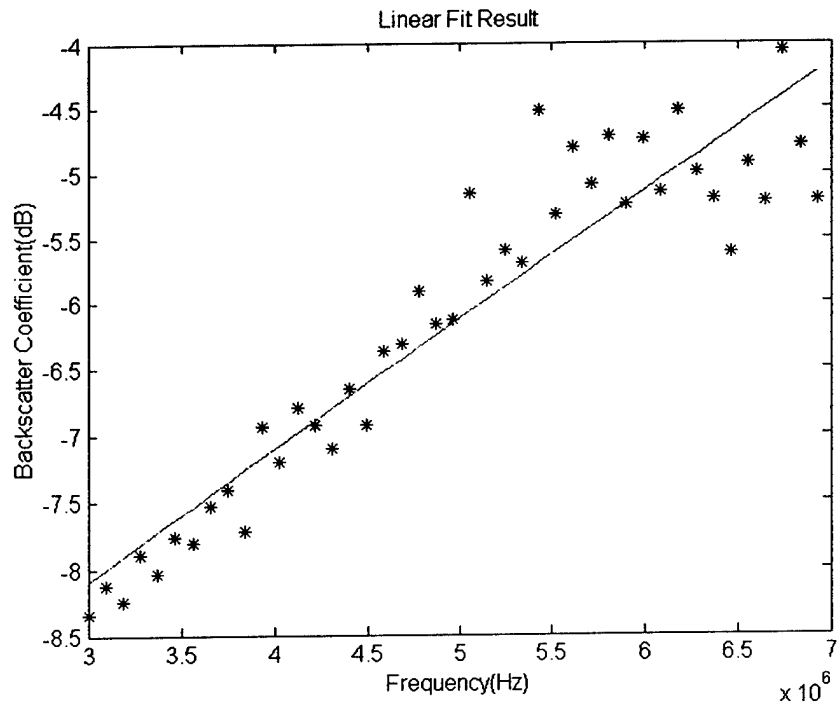


Figure 22: Tissue backscatter intensity vs. frequency

Chapter 3: Evaluation Methods

This chapter contains a review of several data analysis techniques such as correlation analysis, t-test, Mahalanobis distance, discriminant analysis and performance analysis, which will be used in Chapter 5 to analyse the parameters described in Chapter 2.

3.1 Correlation Analysis

Statistical correlation refers to a quantifiable relationship between two variables. Furthermore, it is a measure of the strength and direction of that relationship. The strength and direction of a correlation are indicated by the correlation coefficient. Computing the correlation coefficients provides an efficient method to identify all redundant features within a group. A redundant feature provides little or no new information to aid in the task of distinguishing between samples from the two classes [Mia 1999].

3.1.1 Correlation Coefficient

The correlation coefficient (r) is a number between -1 and 1 that measures the degree to which two variables (X and Y) are linearly related. If there is a perfect linear relationship with positive slope between the two variables, the correlation coefficient is 1; There is positive correlation ($r > 0$) when cases with large values of X also tend to have large values of Y whereas cases with small values of X tend to have small values of Y . If there is a perfect linear relationship with negative slope between the two variables, the correlation coefficient is -1; There is negative correlation ($r < 0$) when cases with large values of X tend to have small values of Y and *vice versa*. A correlation coefficient of 0 means that there is no linear relationship between the variables. Correlation coefficients give no information about cause and effect.

Similarly they provide misleading information if the relationship between X and Y is non-linear.

Scatter plots are useful tools to interpret the correlation coefficient. Different types of correlations are shown in Figure 23

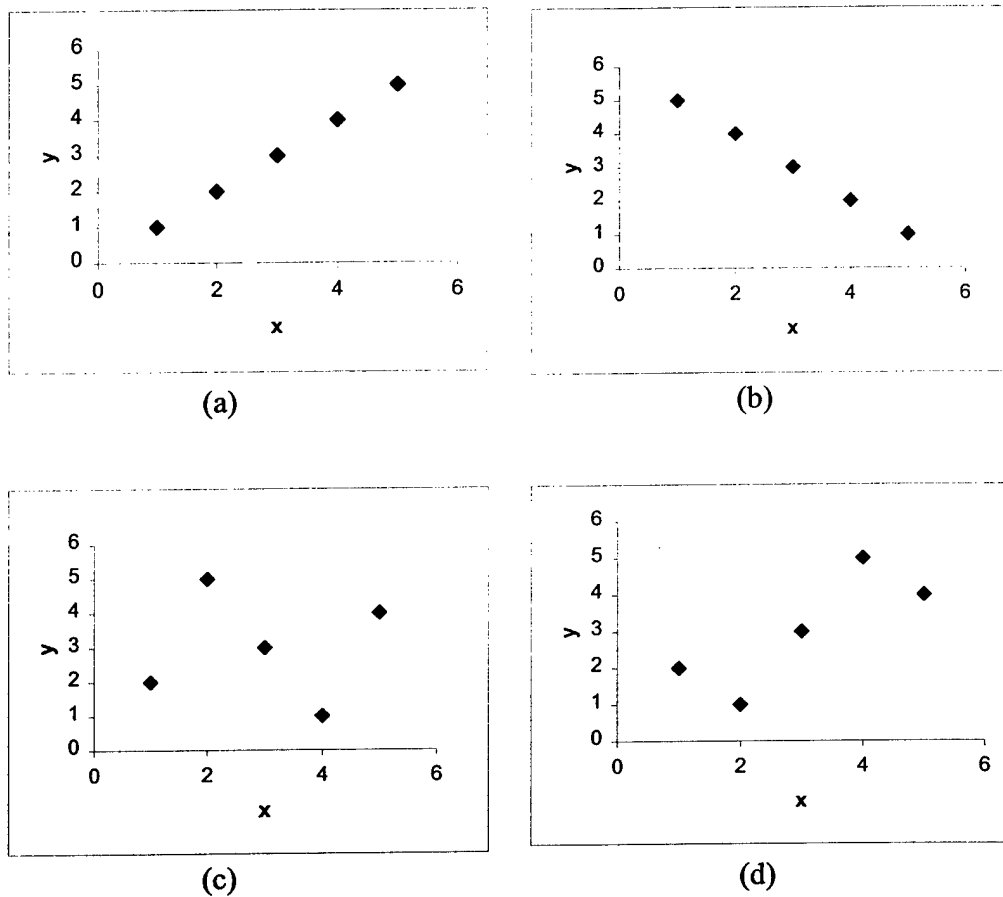


Figure 23: Scatter plots of different types of correlations (a) Positive correlation (b) Negative correlation (c) No correlation (d) Moderate positive correlation

There are a number of techniques for measuring correlation coefficients. The most popular are Person's Product Moment and Spearman's Rank.

3.1.2 Pearson's Product Moment Correlation Coefficient

Pearson's product moment correlation coefficient, usually denoted by r , is one example of a correlation coefficient. It is a measure of the linear association between two variables that have been measured on interval or ratio scales, such as the relationship between height in inches and weight in pounds. However, it can be misleadingly small when there is a relationship between the variables but it is a non-linear one [Minitab 1997].

We can use the following formula to compute Pearson's r . The correlation between two variables x and y is defined as the covariance of x with y divided by the product of the standard deviation of x and the standard deviation of y :

$$r_{xy} = \frac{\text{cov}_{xy}}{s_x s_y} \quad (3.1)$$

with

$$\text{cov}_{xy} = \frac{\sum (x - \bar{x})(y - \bar{y})}{n - 1}$$

where cov_{xy} is the covariance between two variables x and y , \bar{x} and s_x are the sample mean and standard deviation for the first sample, and \bar{y} and s_y are the sample mean and standard deviation for the second sample.

If there are multiple features, we can build the correlation matrix with equation (3.2). Computing the correlation matrix provides an efficient method to identify the redundant features within a group.

$$R = \begin{bmatrix} r_{11} & r_{12} & \cdots & r_{1n} \\ r_{12} & r_{22} & & r_{2n} \\ \vdots & & \ddots & \vdots \\ r_{1n} & r_{2n} & \cdots & r_{nn} \end{bmatrix} \quad |r_{ij}| \leq 1.0 \quad i, j = 1, \dots, n \quad (3.2)$$

with

$$r_{ij} = \frac{\text{cov}_{ij}}{\sigma_i \sigma_j} \quad r_{ij} = r_{ji} \quad r_{ii} = 1$$

$$\text{cov}_{ij} = \frac{1}{N-1} \sum_{k=1}^N (f_{ik} - m_i)(f_{jk} - m_j)$$

where σ_i and σ_j are the standard deviation of the i^{th} and j^{th} feature. N is the total number of samples and n is the number of features. The correlation matrix is symmetric about the major axis.

The strength of correlation can be indicated by magnitude (absolute value). For example, -0.9 is just as strong as 0.9 except the direction. Table 3 shows the characterizations of Pearson r .

Data Range	Correlation
.90 to 1	very high
.70 to .89	High
.50 to .69	Moderate
.30 to .49	low
.00 to .29	little if any

Table 3: Characterizations of Pearson r

So the Pearson product moment correlation coefficient can be used to measure the degree of linear relationship between two variables. The correlation coefficient assumes a value between -1 and +1. If one variable tends to increase as the other decreases, the correlation coefficient is negative. Conversely, if the two variables tend to increase together the correlation coefficient is positive [Minitab 1997].

3.1.3 Limitations of the Correlation Tests

Correlation does not imply causality. A significant correlation does not necessarily mean cause and effect. It should be noted that Pearson r computations are sensitive to extreme values in the data.

3.2 t-test

The t-test assesses whether the means of two groups are statistically different from each other. The t-test will be used to help find the most promising features among the features introduced in Chapter 2 [Minitab 1997].

For example, in Figure 24, there are three different possible outcomes, labeled medium, high and low variability. Notice that the differences between the means in all three situations are exactly the same. The only thing that differs between these is the variability or “spread” of the scores around the means. A small difference between means will be hard to detect if there is lots of variability or noise. A large difference between means will be easily detectable if variability or noise is low. This way of looking at differences between groups is directly related to the signal-to-noise metaphor – differences are more apparent when the signal is high and the noise is low [Trochim 2001].

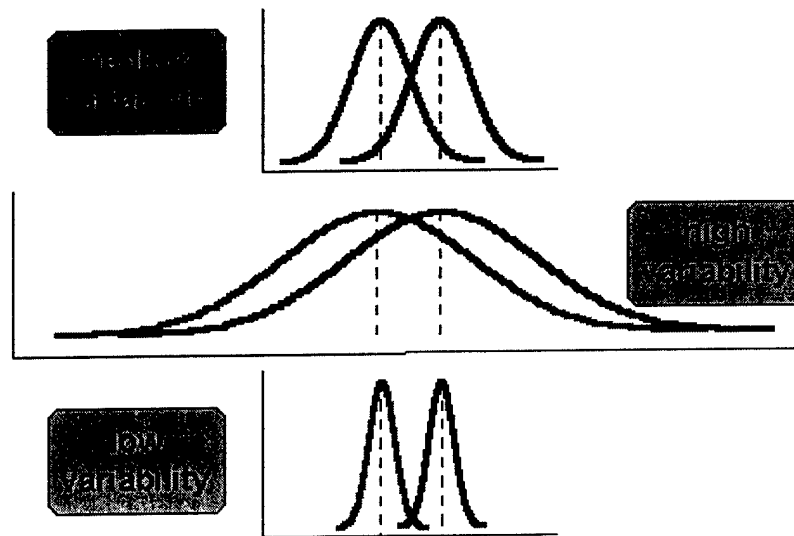


Figure 24: Deference between means [Trochim 2001]

There are five factors that contribute to whether the difference between the means of two groups can be considered significant: the difference between the means of the two groups, the overlapping degree between the groups, the number of subjects in the two groups, the alpha level used to test the mean difference (how confident that there is a mean difference), and whether a directional (one-tailed) or non-directional (two-tailed) hypothesis is being tested [Minitab 1997].

There are three types of t-test: paired t-test (correlated t-test), equal variance t-test (pooled variance t-test) and unequal variance t-test (separate variance t-test). In this study, it is necessary to tell the difference between independent sample means with unequal variance. The test statistic t is calculated by Equation (3.2)

$$t = \frac{(\bar{x}_1 - \bar{x}_2)}{s} \quad (3.2)$$

with

$$s = \sqrt{\frac{s_1^2}{n_1} + \frac{s_2^2}{n_2}}$$

A p-value below 0.05 is generally considered statistically significant, while one of 0.05 or greater indicates no difference between the groups.

3.3 Mahalanobis Distance

An alternative distance measure that is in common use is the Mahalanobis distance. This is similar to the Bayesian distance in that it takes into account the shape of the covariance matrix of the class model. However, the derivation of the Mahalanobis distance formula assumes that the covariance matrices of each class are the same in order to simplify the calculations involved. Thus it is valid to use the Mahalanobis distance measure if the data for each class are similarly distributed. However, there is nothing to prevent its use if they are not. The Mahalanobis distance is defined as:

$$d_i^2(x) = (x - m_i)' S_p^{-1} (x - m_i) \quad (3.2)$$

where $d_i^2(x)$ is the Mahalanobis distance (also called the squared distance) of observation x to the center (mean) of group i . m_i is the mean value of group i . S_p^{-1} is the inverse of the variance-covariance matrix of X . A column in X is represented by x . Notice,

$$d_i^2(m_j) = d_j^2(m_i) \quad (3.3)$$

This is the Mahalanobis distance between groups i and j .

3.4 Discriminant Analysis

A discriminant analysis is used to classify observations into two or more groups. Discriminant analysis can also be used to investigate how variables contribute to group separation [Minitab 1997].

There are two types of discriminant analysis – linear and quadratic discriminant analysis. With linear discriminant analysis, all groups are assumed to have the same covariance matrix. Quadratic discrimination does not make this assumption but its properties are not as well understood. The linear discriminant analysis with cross-validation and prior probabilities is used in this study.

3.4.1 Linear Discriminant Analysis

An observation is classified into a group if the Mahalanobis distance of observation to the group center (mean) is the minimum. Linear discriminant analysis has the property of a symmetric Mahalanobis distance.

3.4.2 Cross-Validation

Cross-validation is a technique used to compensate for an optimistic apparent error rate. The apparent error rate is the percent of misclassified observations. The cross-validation routine works by omitting each observation one at a time, recalculating the classification function using the remaining data, and then classifying the omitted observation.

3.4.3 Prior Probabilities

Sometimes if the prior probabilities are known or can be estimated, discriminant analysis can utilize it in calculating the posterior probabilities, or probabilities of assigning observations to groups. With the assumption that the data have a normal distribution, the linear discriminant function is increased by $\ln(p_i)$, where p_i is the

prior probability of group i . Because observations are assigned to groups according to the smallest generalized distance, the effect is to increase somewhat the posterior probabilities for a group with a high prior probability.

3.5 Performance Analysis

An approach that provides information about the overall performance of a diagnostic system is known as Receiver Operation Characteristic (ROC) analysis. Such curves were first applied to assess how well radar equipment in World War II distinguished random interference (noise) from signals truly indicative of enemy planes.

When a diagnosis is made, there are usually two types of errors [Mia 1999]: Type 1 errors are when samples from Class 1 are assigned to Class 2. Type 2 errors are when samples of Class 2 are assigned to Class 1. If the normal cases are called Class 1 and the abnormal cases are called Class 2, then the Type 1 error rate is called the False Positive Fraction (FPF) and Type 2 error rate is called the False Negative Fraction (FNF). Similarly, the percentage of correctly assigned samples in Class 1 is called True Negative Fraction (TNF) and the percentage of correctly assigned samples in Class 2 is called the True Positive Fraction (TPF). See Figure 25.

Usually, in ROC analysis, performance of a diagnostic system is described by the indices of “sensitivity” and “specificity”, where “sensitivity” can be expressed as the True Positive Fraction (TPF) and “specificity” by the True Negative Fraction (TNF) of a diagnosis. In a complimentary way, the FNF and the FPF can be defined as $FNF = 1 - TPF$ and $FPF = 1 - TNF$, respectively. Due to this dependence, it is only necessary to measure one pair of indices. Frequently TPF and FPF are used.

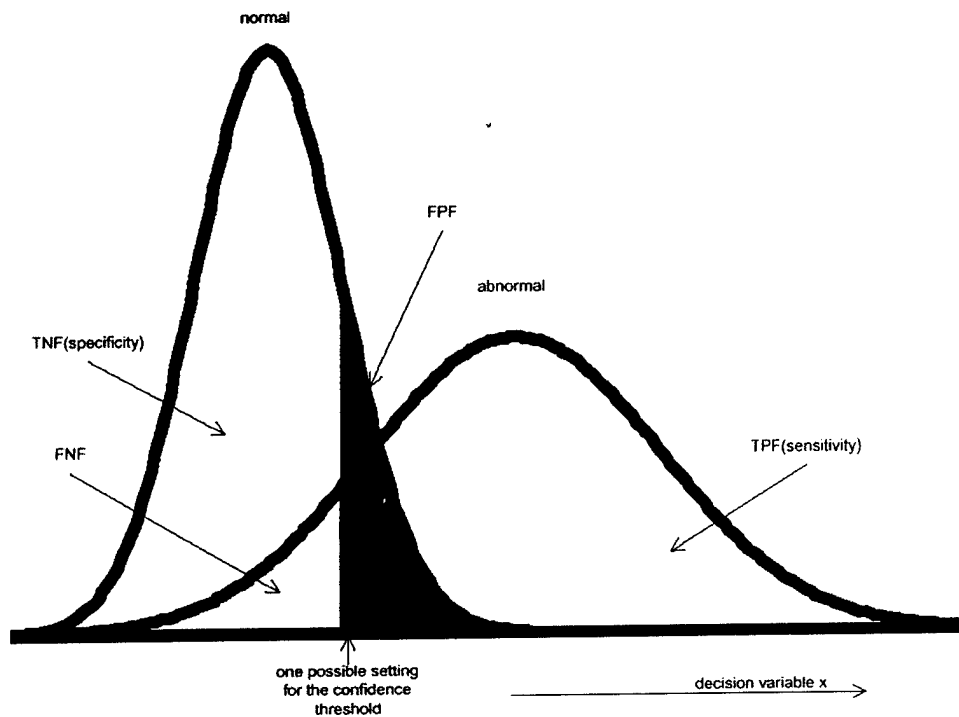


Figure 25: The binormal model for ROC analysis [Frederick 2000]

Figure 26a indicates 10 different decision thresholds, thresholds L1, L2, ... L10. For each of these decision thresholds the FP and TP percentages have been computed. These 10 combinations (FP, TP) have been plotted in curve a in Figure 27. This graphical representation is called ROC curve, which plots the TPF as a function of the FPF.

To show the effect of more or less overlap of the two distributions, in curves b and c of Figure 27, the same two hypothetical distributions are used but they are shifted closer to each other and farther apart, respectively. The effect of more overlapping distributions is seen in ROC curve b and the effect of less overlap is seen in curve c of Figure 27. The less the histograms overlap, the better the ROC approaches the ideal point of $(FP, TP) = (0, 100)$. As curves bow more to the left, they indicate greater

accuracy (a higher ratio of true positives to false positives). The more the histograms overlap, however, the more the ROC approaches the diagonal line that runs from the point $(FP, TP) = (0, 0)$ to the point $(FP, TP) = (100, 100)$. This straight line would signify that the diagnostic test had 50/50 odds of making a correct diagnosis (no better than flipping a coin).

The above example shows that the performance of any decision model is primarily determined by the discriminatory power of the features. If the features show too much overlap, a different decision threshold does not help. This not only applies to models that operate on one feature but also applies to models that use several features at a time. Therefore, the principal task in developing a decision model with an optimal performance is finding the most discriminating features.

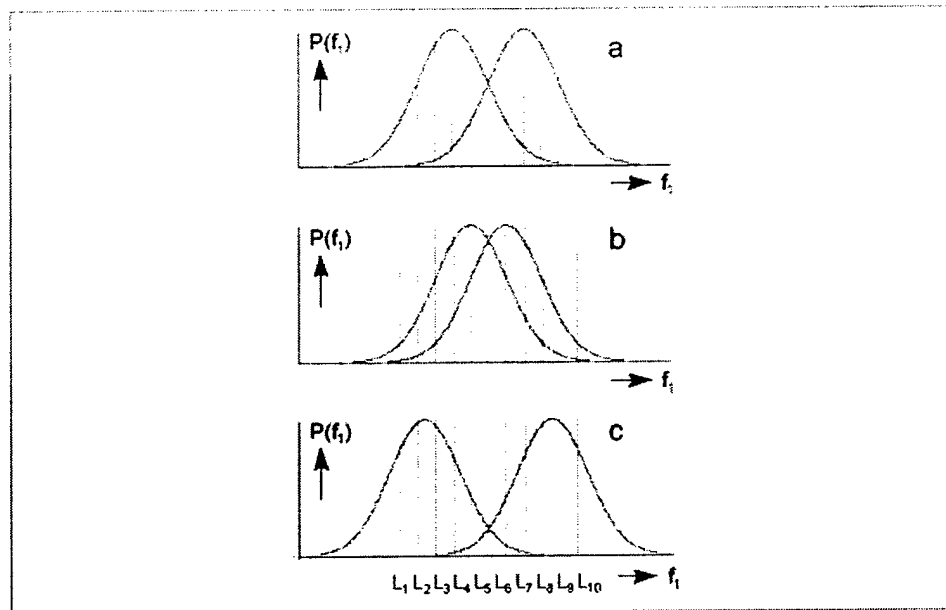


Figure 26: Two normal distributions with 10 different decision thresholds L_1, L_2, \dots, L_{10} [ROC 2001]

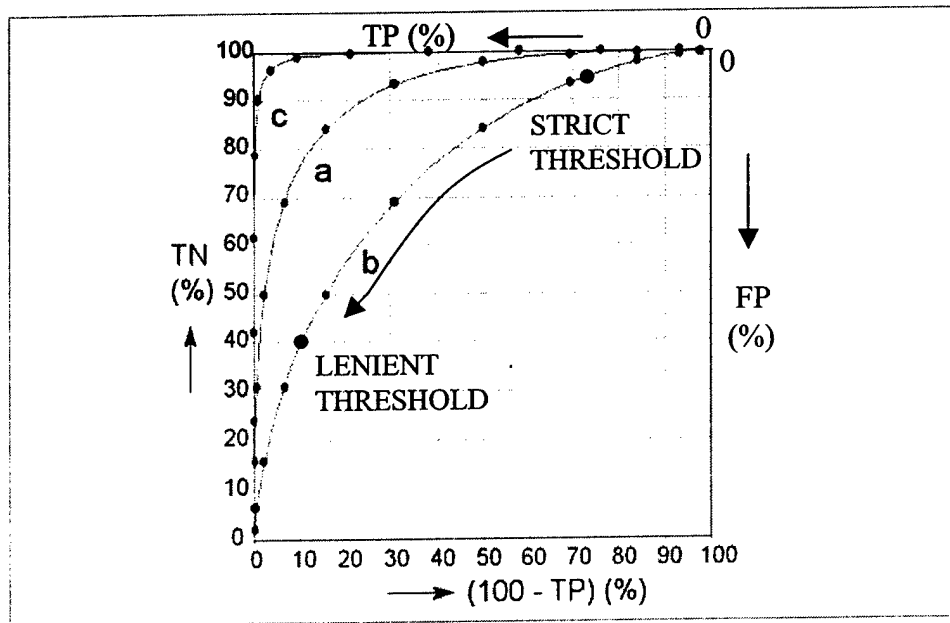


Figure 27: ROC curve [ROC 2001]

The accuracy is indexed more precisely by the amount of area under the curve, which increases as the curves bend to the ideal point of $(FP, TP) = (0,100)$. A rough guide for classifying the accuracy of a diagnostic test is the traditional academic point system:

Data Range	Accuracy of Classification
.90 – 1	Excellent
.80 – .89	Good
.70 – .79	Fair
.60 – .69	Poor
.50 – .59	Fail

Table 4: Characterizations of Az

If the accuracy is acceptable, we can select a threshold for yes/no diagnoses. The goal is to choose a threshold that yields a good rate of true positives without generating an unacceptable rate of false positives. Each point on the curve represents a specific threshold moving from the strictest at the top right to the most lenient at the bottom left. Strict thresholds limit false positives at the cost of missing many cases of cancer; lenient thresholds maximize discovery of the cases of cancer at a cost of many false positives.

One popular software package for performing ROC curve-fitting and statistical analysis is the ROCKIT software developed by a research group led by Charles Metz at the University of Chicago, which uses the LABROC4 algorithm [Metz 1998].

An example ROC curve drawn by using ROCKIT is shown in Figure 28. It shows the performance is 0.7663 ± 0.0659 (area under the ROC curve) by only using a single feature – entropy.

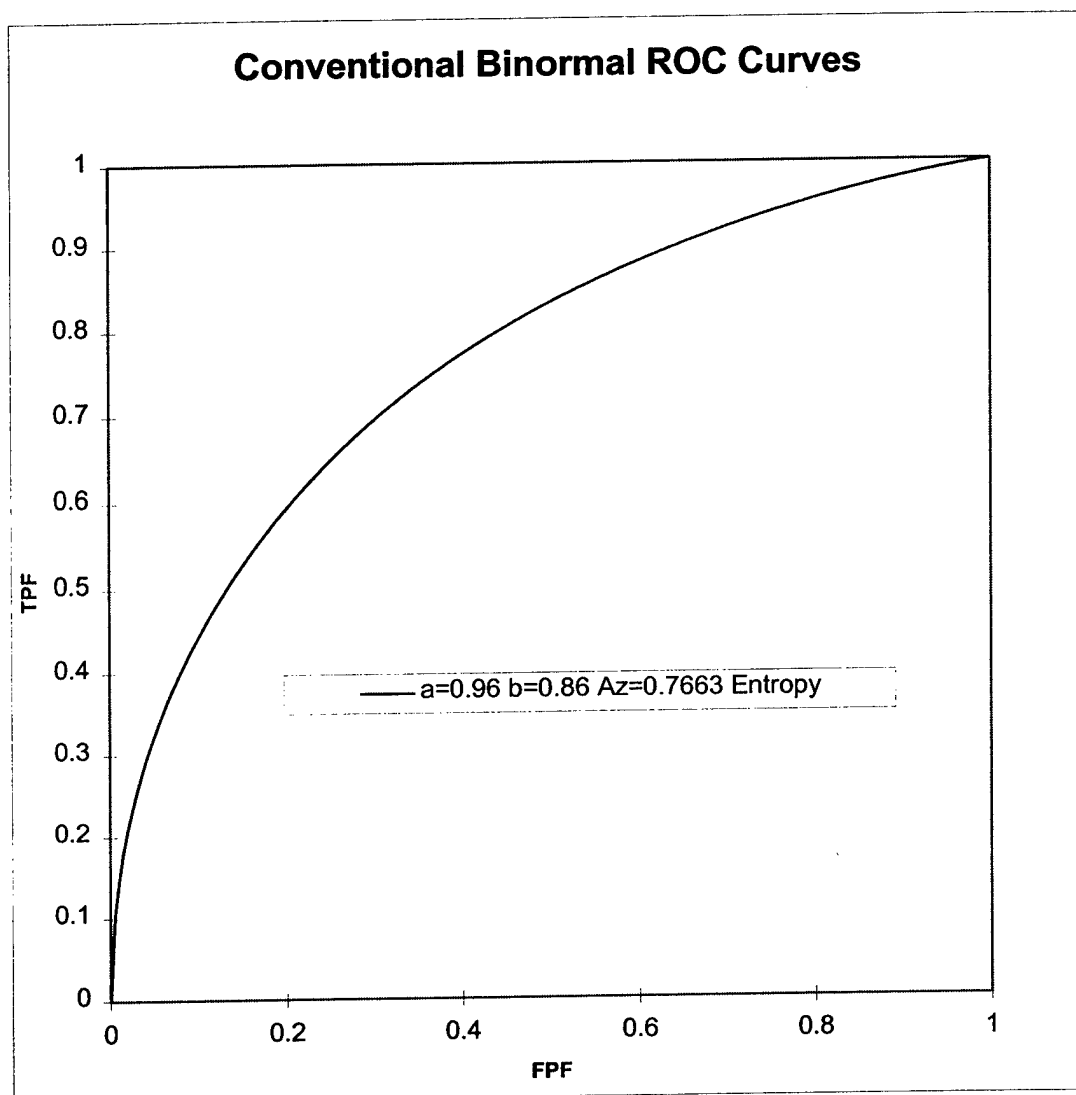


Figure 28: A sample Receiver Operating Characteristic (ROC) curve

Chapter 4 System Implementation

This chapter describes the procedure for acquiring ultrasound radio frequency (RF) data and for composing a pathology image, and the control of the saturation ratio of the RF data. Finally, a detailed description of the development and usage of the software is given.

4.1 RF Data Acquire

Using the linear array transducer, in vitro ultrasound data are acquired from fresh radical prostatectomy specimens that are obtained immediately after resection at Fletcher Allen Health Care. The whole prostate gland is transported from the operating suite to the ultrasound instruments. The specimen is immediately immersed in sterile isotonic saline solution in a tank with sound absorbing walls. The prostate is oriented so that the plane of the base of the gland is vertical and the posterior (peripheral zone) is at the top of the tank. The gland is then scanned using a Diasonics Spectra real-time scanner with a 5 MHz center-frequency scanhead. The scan planes are parallel to the base of the gland and are taken in the tranverse plane with a clamped transducer. The scan planes are taken at 2 mm intervals. The ultrasonic RF signal is digitized (8 bits) at 48 MHz using a LeCroy digitizer. Figure 29 shows the experimental scan setup. Figure 30 is the enlarged image of the pad and the glue that provides a tight contact and an air-free seal between the transducer and the specimen. The air-free seal is necessary for the transducer to send the high frequency sound into the object unimpeded.

After the conclusion of the prostate RF data acquisition, RF data from a special phantom, whose frequency-dependent attenuation and backscatter properties are known, is collected using the same machine settings. These data are used for calibration of the prostate RF data.

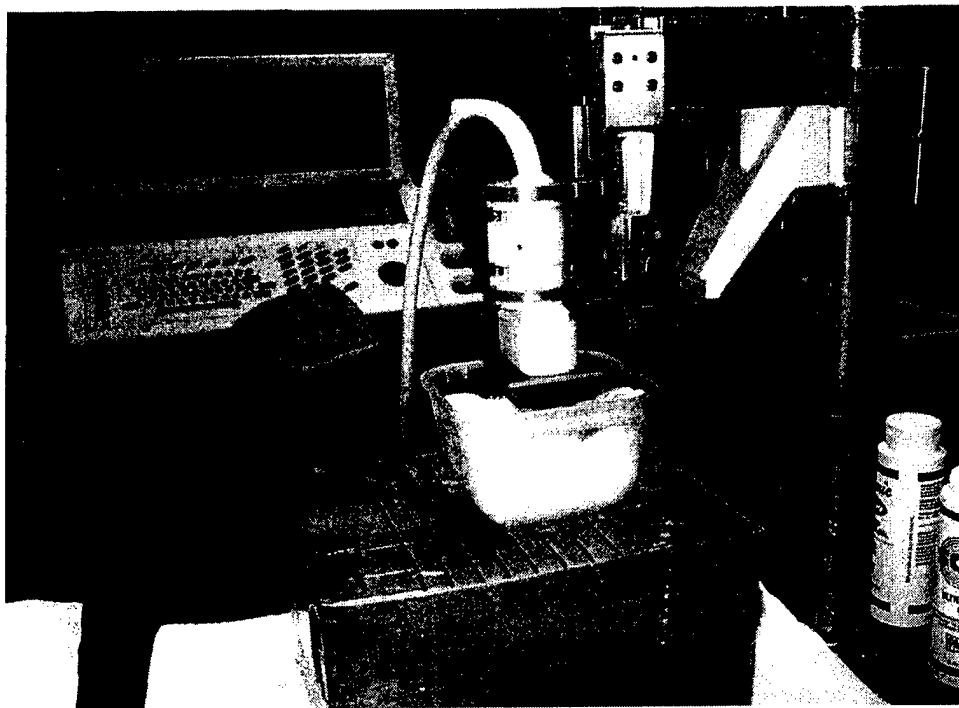


Figure 29: In vitro experimental scan setup



Figure 30: Pad and glue

4.2 Saturated-ratio Control Software

When the ultrasound radio frequency data are acquired, one problem needs to be considered. Because the LeCroy digitizer samples the data in 8 bits, the data range is from -128 to 127. If the maximum value of the data is outside of this range, which means that data is “saturated”, some important information is missed. The saturated-ratio is defined as the number of data outside the range of -128 to 127 over the total number of the data. Usually the saturated-ratio of “good” data should be pretty close to 0%, which means few data is outside the range of -128 to 127.

An example of saturated RF data appears in Figure 31. The upper image shows the ultrasound image of the radio frequency data. The lower image shows one line in the radio frequency data set. The saturated-ratio of this example is 10.31%, which means more than 10% of the data are outside the range of -128 to 127. Obviously, many peaks are cut off and some important information is lost. Thus, the system needs to be adjusted.

It should be noted that it is difficult to determine if the RF data are saturated by merely examining the B-mode images. In order to minimize saturation problems, a software tool has been developed. The software helps in the adjustment of the machine settings that reduce the saturation-ratio and let the data fall into the range of -128 to 127. Once the saturation-ratio is pretty close to 0%, the settings of the machine are fixed. The result after adjustment is shown in Figure 32.

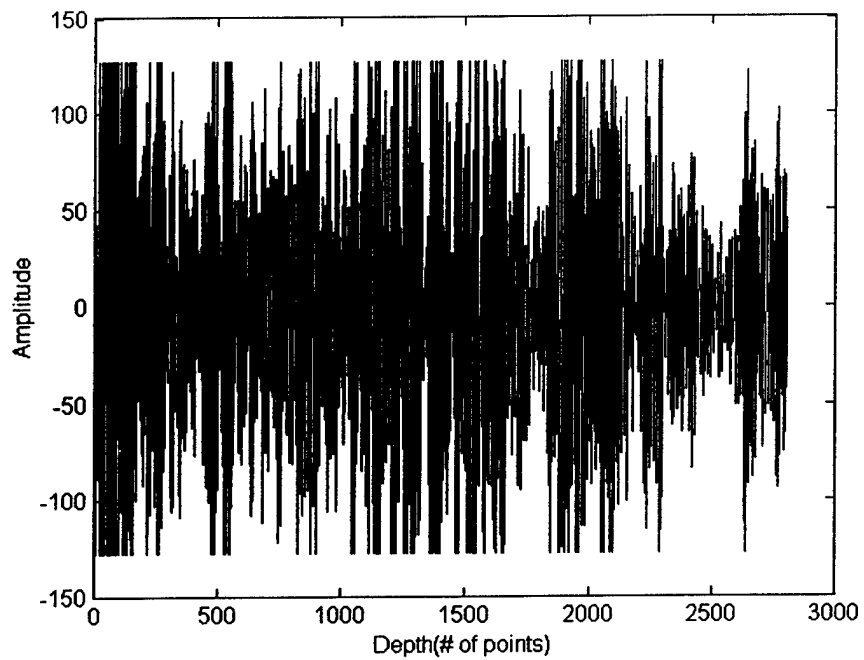
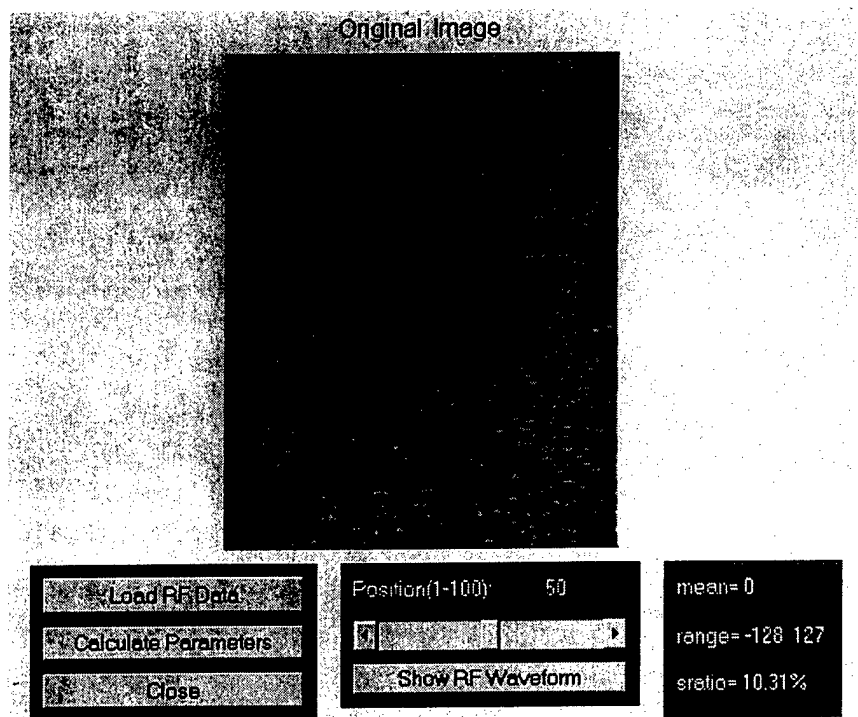


Figure 31: Saturated control – before adjustment

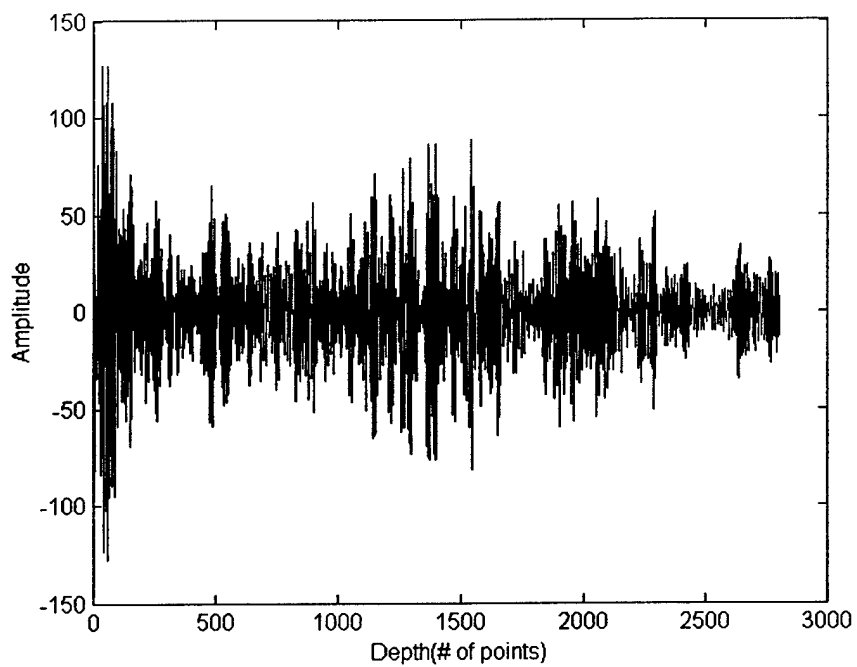
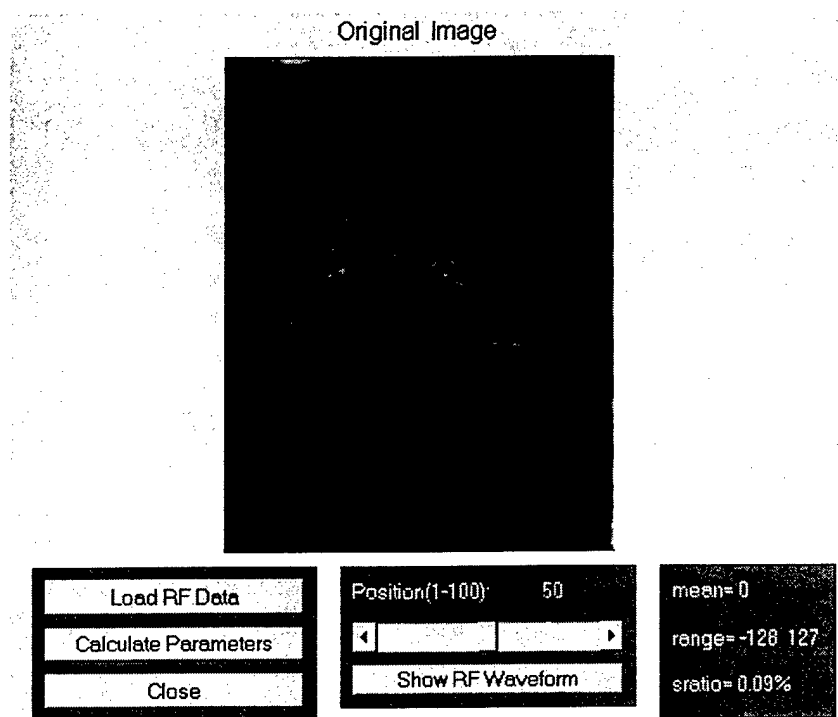


Figure 32: Saturated control – after adjustment

4.3 PATH Image Composite

After ultrasound data acquisition, the prostatectomy specimen is fixed in buffered formalin. This process stiffens the tissue so that less deformation occurs during sectioning. Next the specimen is sent to a surgical pathologist for examination. The gland is sliced into multiple transverse sections with the plane of the sections being perpendicular to the posterior surface of the gland. This is simply achieved by placing the posterior surface down on the cutting table and cutting downward vertically. Ideally, these slices would correspond to the ultrasound image slices.

After the transverse sections are made in pathology, each section is further divided into quarters so that the tissue will fit on a standard microscope slide. The pathologist examines the section quarters and all foci of cancer are marked on the glass slide with indelible ink. Then the slides (quarter sections) are digitized for reassembly into complete sections (also known as “whole mount” sections).

The glass slides are simply arranged on the tray of a transparency flatbed scanner and “scanned” in at a resolution of 200 – 400 dpi. The digitized images are then placed into Adobe Photoshop, and the images are “warped” slightly to fit better with each other. Warping is necessary since some shrinkage and distortion occurs during the sectioning and fixation process. Figure 33 shows the scanning result of four-quarter sections with cancer marked. Figure 34 is the result of assembling four-quarter sections into a whole slice.

Since the cancer area was marked with indelible ink on the pathology image by the pathologist, this information will be used to find the location of the cancer area in the ultrasound image and in the ultrasound RF data set as well. The details can be found in 4.4.3.

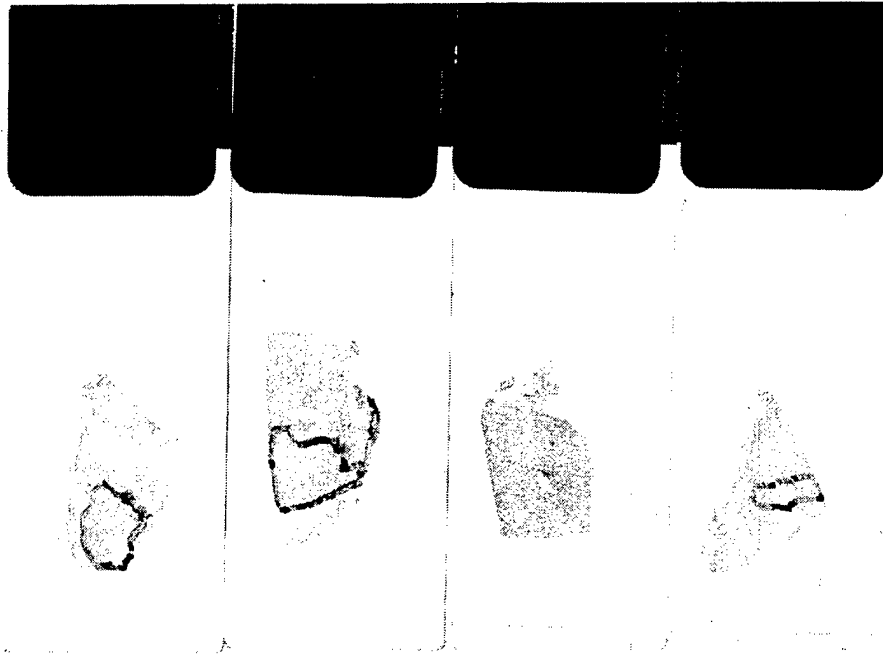


Figure 33: Pathology quarter sections with CA marked

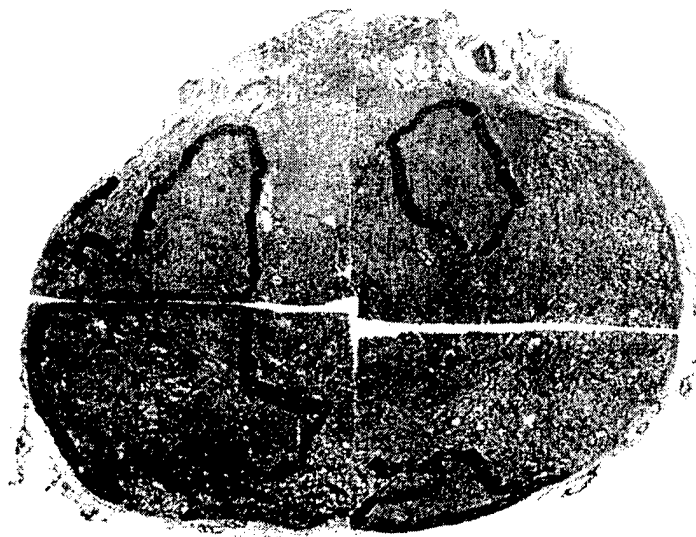


Figure 34: Quarter sections assembled into whole slice

4.4 User Interface Design

Feature computation software has been developed for the in vitro prostate tissue classification project. This MATLAB based software has a Windows graphical user interface (GUI). Figure 35 is a screen shot of the GUI. When the user chooses one ultrasound image (left image), it will automatically select the corresponding pathology image (right image). Then the user draws a ROI on the pathology image and the software maps it in the ultrasound RF data set. All of the features introduced in Chapter 2 are calculated for the ROI. The result is stored in a database. This section will introduce how to build the database, how to load the PATH image for the US image automatically, how to locate the ROI between the US and PATH images, as well as the usage of this software.

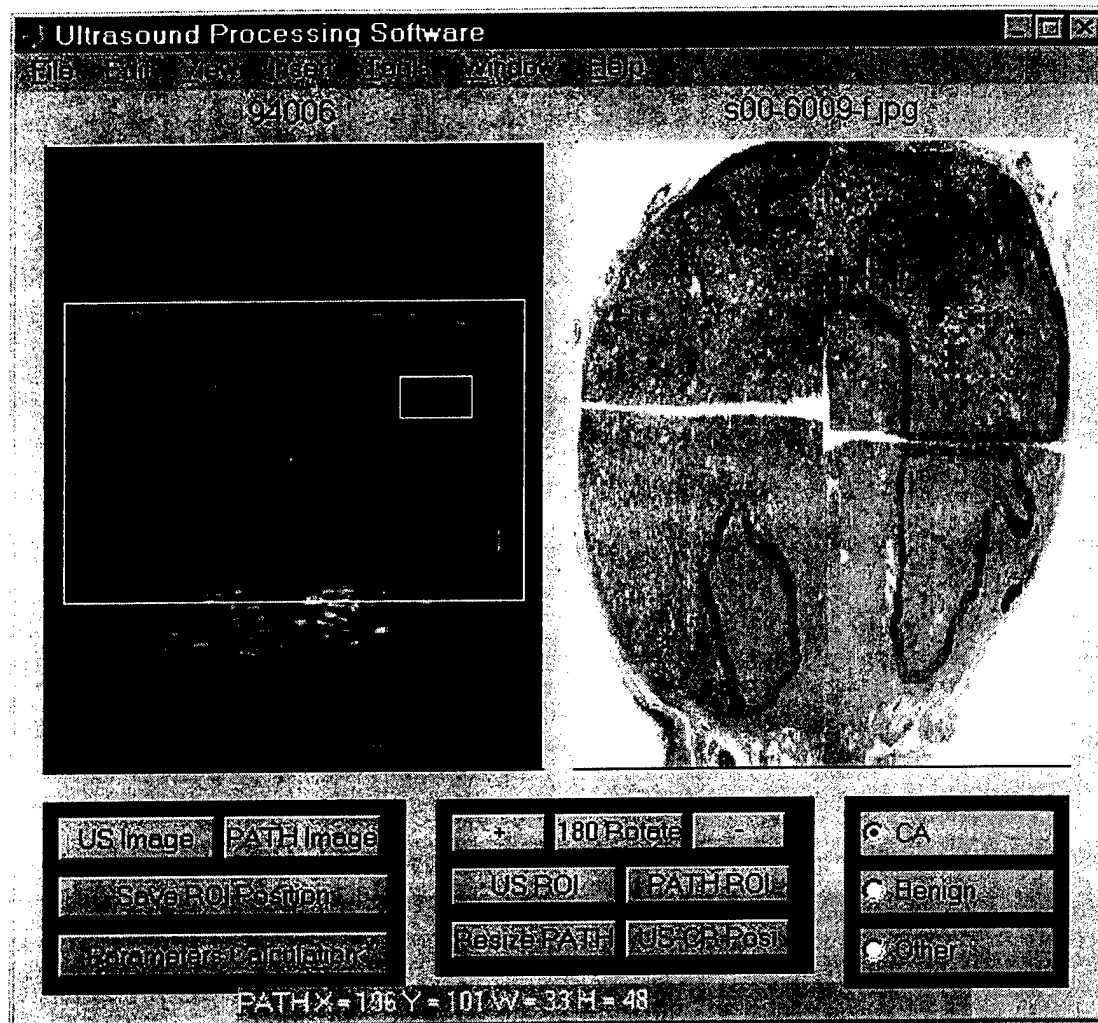


Figure 35: Graphic user interface

4.4.1 Building Database

In the development of the software, according to specification, it was necessary to store a large amount of different types of information. It was decided to use a database to fulfill this requirement. Microsoft Access 2000 was chosen to store the information. Software was developed to accomplish the data processing tasks by using the database tools provided by MATLAB.

The first development step was to decide the structure of the database. Generally, there are three steps related with the database. First, it is necessary to put some information about each case, such as the ultrasound filename of the case, the number of slices in the case, the corresponding pathology filename and number, and the corresponding phantom filename. Second, when this tool is used to locate the region of interest (ROI) inside the radio frequency data, the location and character of each ROI needs to be recorded. Third, it is necessary to store the features for each ROI. So three tables are needed in the database. The first (patient) stores the information of each case, the second (roiinf) saves the ROI information, and the third (feature) saves the features for each ROI. The structure of patient and roiinf is listed in Appendix A.

After building the structure of the database, the connection to MS Access 2000 had to be constructed. This can be done via Open Database Connectivity (ODBC) Data Source Administrator, which is in the Control Panel (the operating system is Window 2000). ODBC is a widely accepted application programming interface (API) for database access. It is based on the Call-Level Interface (CLI) specifications from X/Open and ISO/IEC for database APIs and uses Structured Query Language (SQL) as its database access language.

Once the database and the connection to the database are built, the database is ready to be used in the program and to provide the services we needed.

4.4.2 Loading PATH Image for US Image Automatically

When processing the data, the specific ultrasound file for a slice in one case is loaded. The corresponding pathology image also needs to be loaded. Most of the time this relation is not a simple one to one mapping. Usually, the number of ultrasound slices is not the same as that of the pathology images. Also both of these numbers vary with the size of the gland. It would be annoying to do the calculation every time the data is processed. The strategy to handle this issue is to put these information in the database. There is one table in the database called patient, whose structure can be found in Table 14. With the help of these information, when one ultrasound file is loaded, the corresponding pathology image can be calculated using following equation:

$$j = \text{round}(i \times \frac{n_p}{n_u}) \quad (4.1)$$

where i and j are the position in the ultrasound and pathology slices. n_p and n_u are the numbers of ultrasound and pathology slices respectively.

For example, if 15 slices were taken using ultrasound and only 12 were taken in pathology. Once the third ultrasound slice is chosen, according the above equation, the second slice in the pathology images will be loaded. The spacing between slices is 2mm for ultrasound and $15/12 \times 2\text{mm} = 2.5\text{mm}$ for pathology. The third ultrasound slice is at a position within the gland of $3 \times 2 = 6\text{mm}$. The second pathology slice is at a position of $2 \times 2.5 = 5\text{mm}$ within the gland.

Since the position of the slice in pathology and ultrasound is not the same, this introduces uncertainty into the exact pathology slice with which the ultrasound data should be correlated. The solution to this problem is to only use cancer foci that are large enough to appear on several pathology slices. This reduces the possibility that

ultrasound data coming from normal prostate tissue is mistakenly used as cancer in the data processing.

4.4.3 Locating the ROI Between the US and the PATH Image

When one ROI is specified in the pathology image, the corresponding ultrasound data needs to be found. The features for that ROI are then calculated. The following is the details for how to map the ROI between ultrasound and pathology images.

First, the boundary of the prostate in the pathology image needs to be specified. The original size of the pathology image is 600 x 600. This is shown in upper right of Figure 36. When the pathology image is loaded into the GUI, it will be resized to 256 x 400 (the size of the image axes) (upper middle). Then the user will use the mouse to draw a box (shown in long dash dot) inside the image to find the boundary of the gland, which is represented by the red ellipse. The boundary of the prostate will be resized to 256 x 400 (upper left).

Second, it is necessary to specify the boundary of prostate in ultrasound image. The original size of ultrasound image matrix is 256 x 320 (lower right). Due to the size of transducer, if the size of gland is larger than the transducer, the boundary of the gland will be outside of the image. So the tool should allow the user to draw a box outside of the original image region when indicating the boundary of the prostate,. To solve this problem, the size of the image matrix was increased to 308 x 384 by adding some zeroes around the original image matrix (lower middle). Then the image is resized to 256 x 400. With the help of radiologist, the boundary of the gland in the ultrasound image is contained by a box using long dash dot. The boundary of the gland outside of the original image is marked by red dashes.

Since the boundaries of gland are marked on both the ultrasound and the pathology image, the next step is to draw the ROI on the pathology image and according to the

geometric relation between them to find the corresponding position in ultrasound data set. All of these relations are shown in Figure 36.

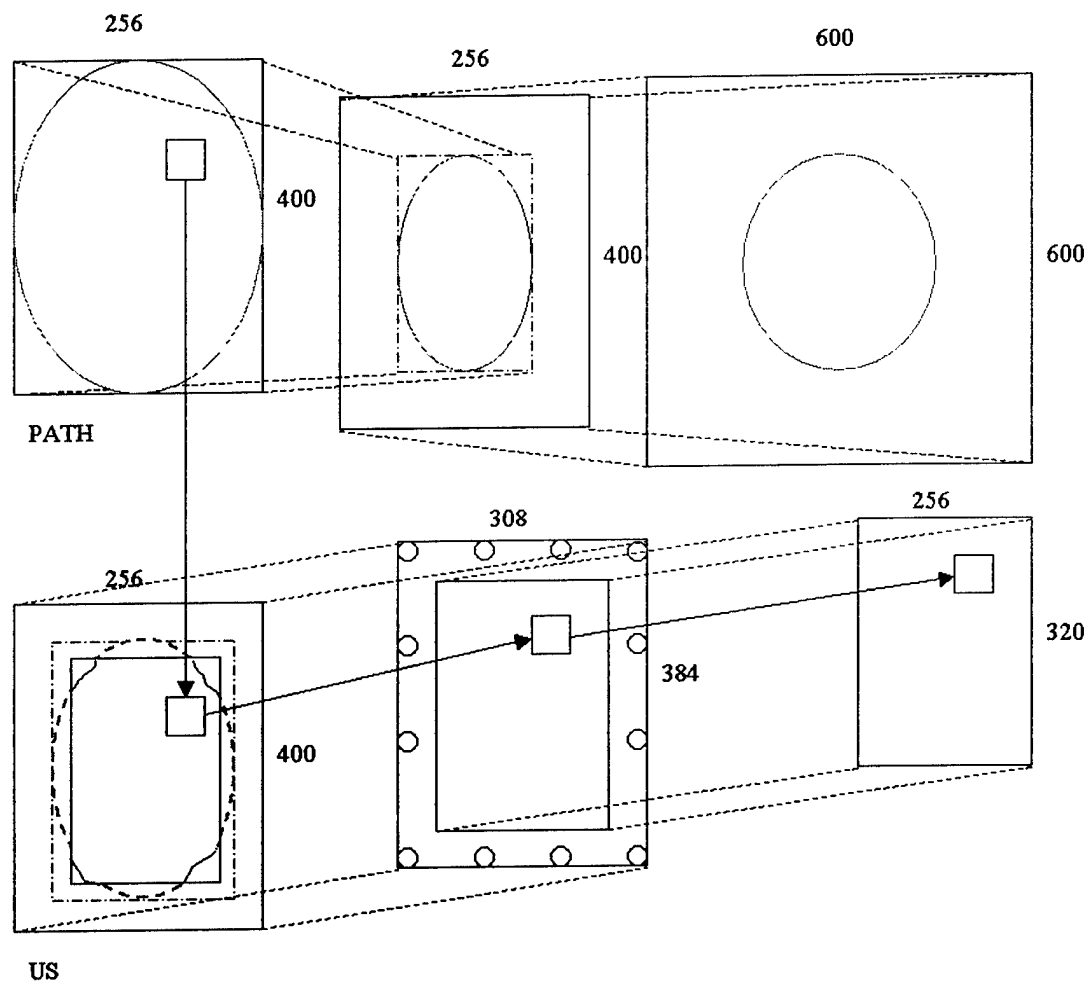


Figure 36: Mapping the ROI between pathology and ultrasound images

4.4.4 GUI Usage

Before using the software to compute the tissue features, it is necessary to build the ODBC connection to the Microsoft Access 2000 and input the needed information into the database, which is described in 4.4.1.

First, one ultrasound slice file and the corresponding pathology image are loaded. The software automatically turns the RF data into an ultrasound image and loads the right pathology image according to the information in the database. Notice that the position of scanning and cutting the prostate are in opposite directions. The pathology image needs to be rotated 180 degree to get the same direction as the scanning image.

Second, find the boundary of the prostate on both images, map the region of interest to the ultrasound data set, and save all the position information in the database.

Then with the help of the position information, all of the features are calculated for each ROI. The results are saved in the database.

The flowchart of the usage of the GUI is shown in Appendix B.

Chapter 5: Results

The parameters described in Chapter 2 were extracted from the RF ultrasound signals by using the tool introduced in Chapter 4. The evaluation methods described in Chapter 3 were used to analyze those parameters. The results of that analysis are presented in this chapter. First, the case material and features are summarized. Then, the results of feature analysis are reported.

5.1 Case Material

78 radical prostatectomy specimens have been studied so far. Unfortunately not all of the data from the specimens are useful. Many of the samples have only microscopic (1-2mm) cancer. Some of the data were unusable due to technical problems during acquisition. The current preliminary analysis includes:

Categories	Number of ROIs
Cancer	36 (from 12 cancer patients)
Benign	19 (from benign regions)

Table 5: Case materials

5.2 Features Calculated

The parameters listed in Table 6 were extracted from all of the ROIs listed in Table 5. These features include the raw RF features, which manifest the microscopic information on scatter size and acoustic concentration that is not visually accessible in

images, and the textures features from the co-occurrence matrix, which carry the information on macroscopic tissue architecture. The detail of each feature has been introduced in Chapter 2.

Groups	Features
RF	Backscatter vs. Frequency Slope
	Backscatter Zero Frequency Intercept
	Backscatter Mid Band Value
Image Statistics	Signal to Noise Ratio
Image Texture (Co-occurrence)	Angular Second Moment
	Entropy
	Contrast
	Correlation

Table 6: List of features

5.3 Feature Analysis

First, the ability of each feature to separate the two groups was assessed by using Student's t-test. Then, to identify the combination of features that most efficiently separated normal from cancer with lowest error rates, a stepwise discriminate analysis was employed.

5.3.1 t-test

The t-test assesses whether the means of two groups are statistically different from each other. Table 7 provides the results for the mean and standard deviation (s.d.) of the features for the two groups listed in Table 5. It is usual to say that p-levels < 0.05 are statistically significant. The p-level of ENT is the smallest one, which is 0.00016

and far less than 0.05. It indicates that the mean of ENT is significantly different between benign and cancer regions. This is a positive sign that ENT is one of the best features for separating the two groups.

Feature	CA Mean (\pm s.d.)	Benign Mean (\pm s.d.)	t-test p value
Slope	0.778 \pm .348 dB/MHz	.588 \pm .326	0.05224
Intercept	-11.81 \pm 2.19dB	-10.41 \pm 2.20	0.03160
Mid Band	-7.88 \pm 1.48dB	-7.42 \pm 1.57	0.29304
SNR	1.62 \pm .38	1.36 \pm .35	0.01583
ASM	.0099 \pm .018	.0029 \pm .0026	0.03089
ENT	-5.4 \pm 1.04	-6.42 \pm .78	0.00016
CON	4111 \pm 3872	2066 \pm 1049	0.00482
COR	-.7469 \pm .115	-.8043 \pm .0788	0.03420

Table 7: Results for the mean, standard deviation and t-test

The results are also plotted in the bar chart with error bars in Figure 37. The height of a bar represents the mean value for that group. The error bar shows the 95% confidence limits for each mean. Obviously, ENT is the most significant feature.

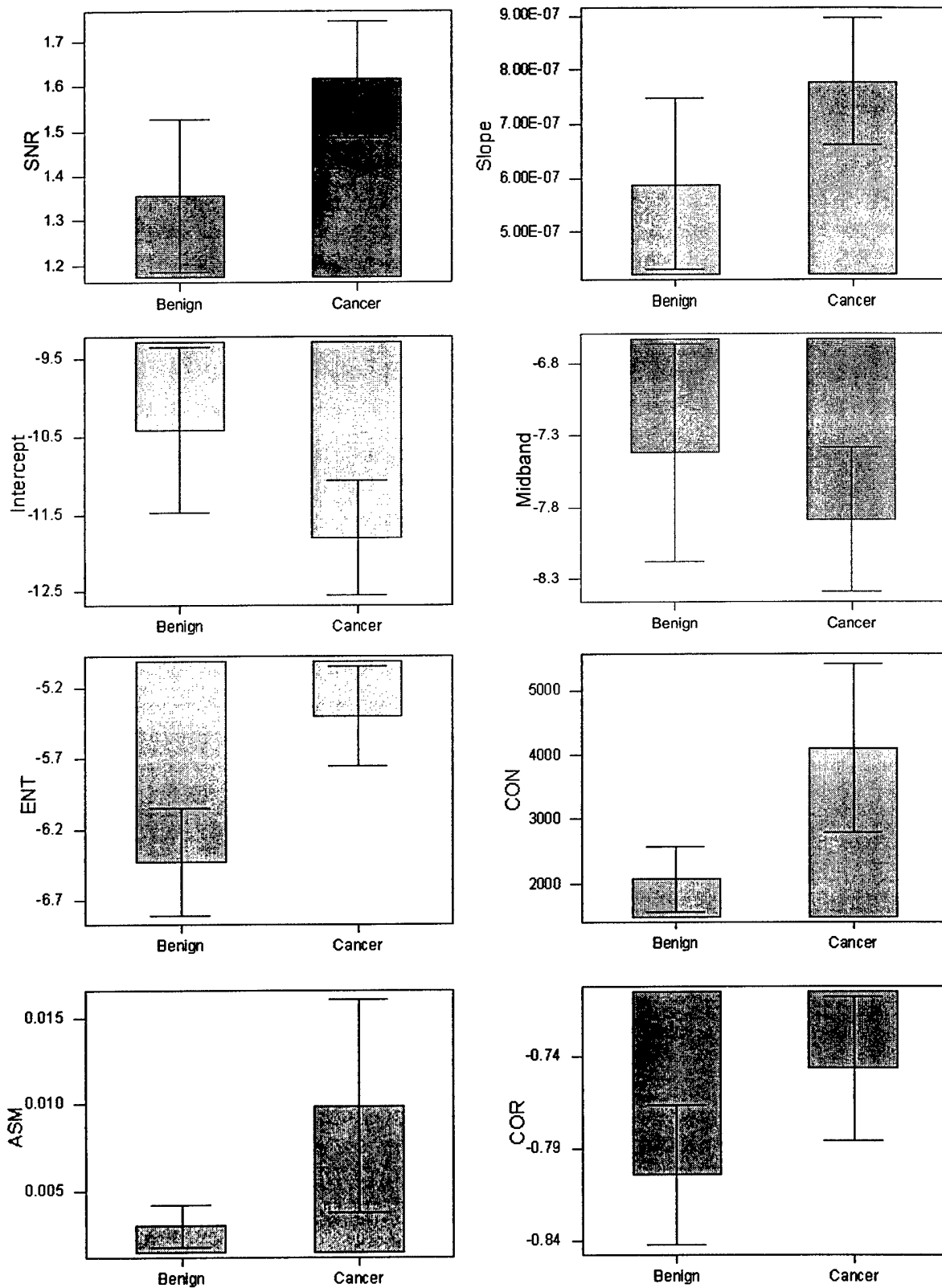


Figure 37: Bar chart of each feature

5.3.2 Correlation

A correlation matrix, as described in Chapter 3, was computed for the set of eight features. The correlation matrix is symmetric about the major axis, so the upper right portion of the matrix, which is not shown, is a mirror image of the lower left portion of the matrix. A positive coefficient indicates the values of variable A vary in the same direction as variable B. A negative coefficient indicates the values of variable A and variable B vary in opposite directions.

	SNR	Slope	Intercept	ENT	ASM	CON	COR	Midband
SNR	—							
Slope	.032 .816	—						
Intercept	-.064 .641	-.767 .000	—					
ENT	.377 .005	.088 .522	-.281 .037	—				
ASM	.349 .009	.074 .592	-.109 .430	.716 .000	—			
CON	.595 .000	.069 .069	-.141 .306	.639 .000	.852 .000	—		
COR	.776 .000	.045 .746	-.155 .258	.284 .035	.094 .493	.498 .000	—	
Midband	-.138 .316	-.025 .858	.647 .000	-.350 .009	-.103 .453	-.183 .180	-.242 .075	—

Cell Contents: Pearson correlation

P-Value

Table 8: Correlation matrix of the eight candidate features

From Chapter 3 we know that when r is between 0.70 and 0.89, it indicates a high correlation. Using a correlation value of 0.70 as the threshold for redundant features, there are four pairs of features that meet that criterion. From the table above, we know the ENT and ASM features have a correlation coefficient of 0.716; the slope and intercept features have a correlation coefficient of -0.767; the CON and ASM features have a correlation coefficient of 0.852; the COR and SNR features have a correlation coefficient of 0.776. So some features can be eliminated without significant loss of information. The decision of which feature(s) to be eliminated can be aided by computing the Mahalanobis distance for each feature.

5.3.3 Mahalanobis Distance

The Mahalanobis distance is a measure of the separation between the means of a feature computed for the two classes. While a low value does not necessarily mean a feature provides no separation between the two classes (separation may still be provided by using a quadratic or other more complex classifiers.). A high value is a good indication that the feature will provide good separation. The Mahalanobis distance, as described in Chapter 3, is presented in Table 9 for each of the eight features.

Feature	Mahalanobis Distance
SNR	0.4855
Intercept	0.4028
Slope	0.3097
Mid-band	0.0949
ENT	1.1430
COR	0.3036
CON	0.4073
ASM	0.2173

Table 9: Mahalanobis distance of each of the eight features

Of the four pairs of features identified as having a high correlation, the ENT feature has the largest Mahalanobis distance. The feature ASM, highly correlated with ENT, is eliminated from the analysis. The other features are retained for further analysis. This leaves seven features from which to select feature combinations that perform well.

The Mahalanobis distance for each of the two-feature combinations is computed in Table 10. Notice that only the pairs including feature ENT have a value larger or equal to the value of 1.143. All of the Mahalanobis distances of the other two-feature combinations are less than 1.143, which also means their classification performances are not better than using the signal feature ENT. Since the Mahalanobis distance of ENT vs. midband and ENT vs. CON is almost the same as 1.143, and ENT vs. ASM has a high correlation, the most promising pairs of two-feature combinations are ENT vs. SNR, ENT vs. intercept, ENT vs. slope and ENT vs. COR.

We added one more feature to the above promising pairs to see if any improvement introduced. The Mahalanobis distance of those combinations are shown in Table 11. The largest Mahalanobis distance value is generated by the combination of ENT, slope and SNR, which is 1.700.

	SNR	Intercept	Slope	Midband	ENT	COR	CON	ASM
SNR	—							
Intercept	0.918	—						
Slope	0.840	0.418*	—					
Midband	0.544	0.419	0.410	—				
ENT	1.319	1.352	1.498	1.144	—			
COR	0.487*	0.651	0.628	0.342	1.266	—		
CON	0.577	0.765	0.723	0.454	1.143	.492	—	
ASM	0.558	0.594	0.518	0.493	1.315*	.501	.426*	—

* indicates the two items have a high correlation

Table 10: Mahalanobis distance of two features combination

	SNR	Intercept	Slope	Midband	COR	CON	ASM
ENT&SNR	—						*
ENT&Intercept	1.564	—					*
ENT&Slope	1.700	1.498*	—				*
ENT&Midband	1.321	1.498	1.500	—			*
ENT&COR	1.323*	1.459	1.629	1.275	—		*
ENT&CON	1.377	1.353	1.499	1.144	1.292	—	*

* indicates the two items among the combination have a high correlation

Table 11: Mahalanobis distance of three features combination

5.4 Classification Results

The linear discriminant analysis with cross validation are used to classify observations into two groups. This analysis will use the “leave one out” method [Lachenbruch, 1968] and a linear Bayes classifier to generate 2 x 2 contingency tables at multiple arbitrary decision threshold levels for cancer vs. each of the benign cases. These results were used to compute sensitivities and specificities and to produce an ROC curve with the help of ROCKIT software. The classification performance was measured by the area under the ROC curve (A_z).

Feature Combination	Performance $A_z \pm \text{s.d.}$
ENT SNR	0.8219 \pm 0.0583
ENT Intercept	0.8114 \pm 0.0708
ENT Slope	0.8090 \pm 0.0660
ENT Midband	0.7648 \pm 0.07681
ENT COR	0.8386 \pm 0.0567
ENT CON	0.7778 \pm 0.0675

Table 12: Performance of the two-feature combinations

The classification performance of the six two-feature combinations discussed above is shown in Table 12. The corresponding ROC curves are shown in Figure 38.

When A_z is between 0.80 and 0.89, the accuracy of the classification is good. The threshold level was set at $A_z \geq 0.82$ to identify feature combinations that yielded good classification performance. No single feature provided classification performance above this level. The best classification performance achieved by single feature is 0.77 ± 0.07 that was provided by ENT as shown in Figure 28. There are only two

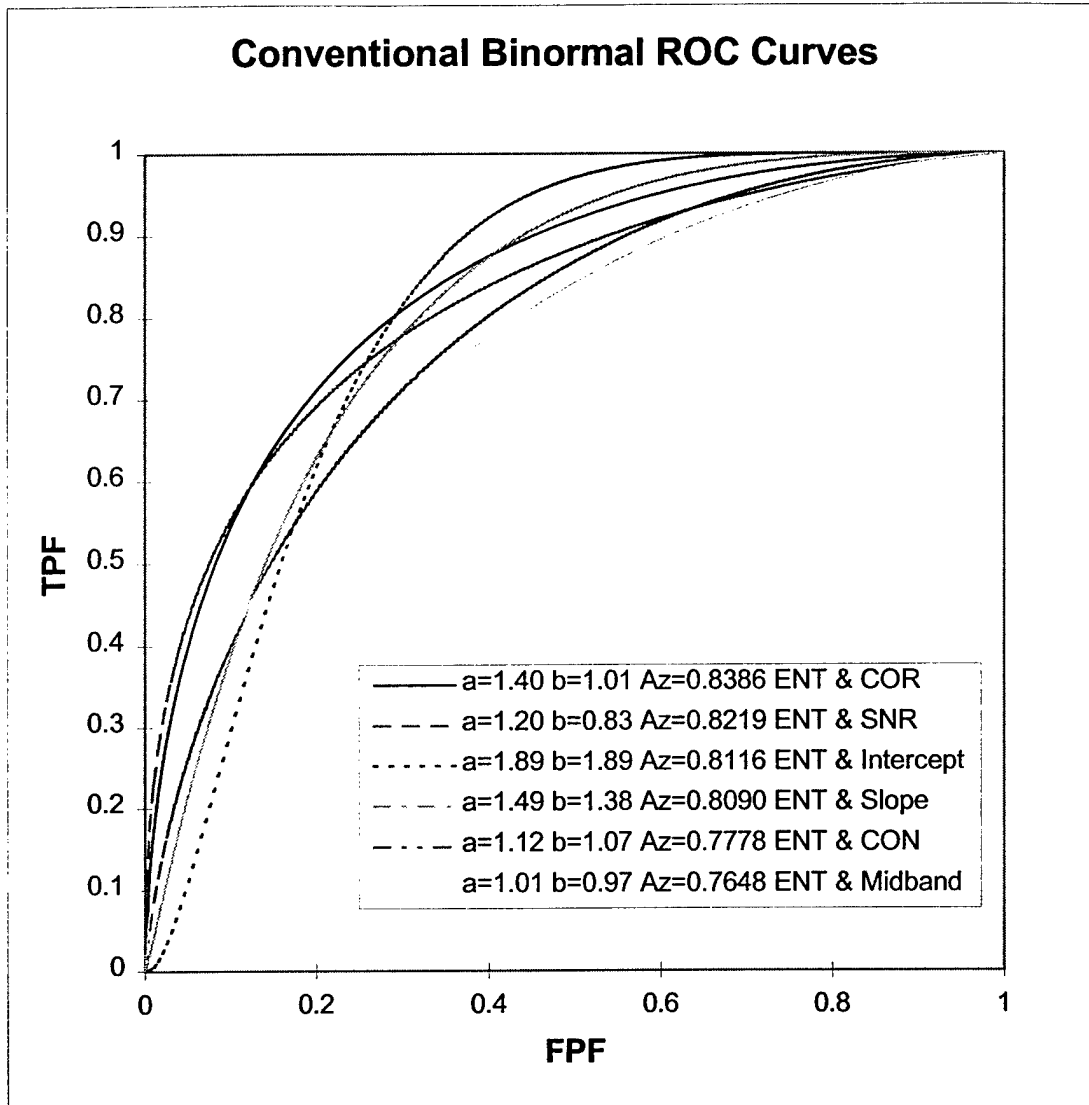


Figure 38: ROC curves of two-feature combination

two-feature combinations that provided classification performance of $A_z \geq 0.82$. They are ENT vs. SNR and ENT vs. COR. The combination of ENT and COR provided the best classification performance among two-feature combinations, which is 0.84 ± 0.06 . The scatter plots of the best two-feature combinations are also shown in Figure 39 and Figure 40 separately.

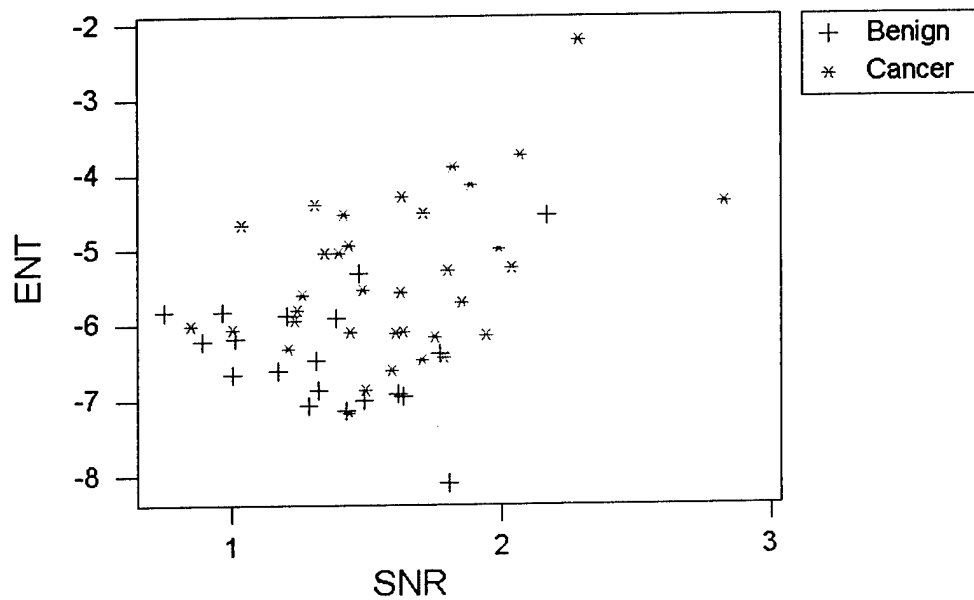


Figure 39: Scatter plot of the ENT and SNR

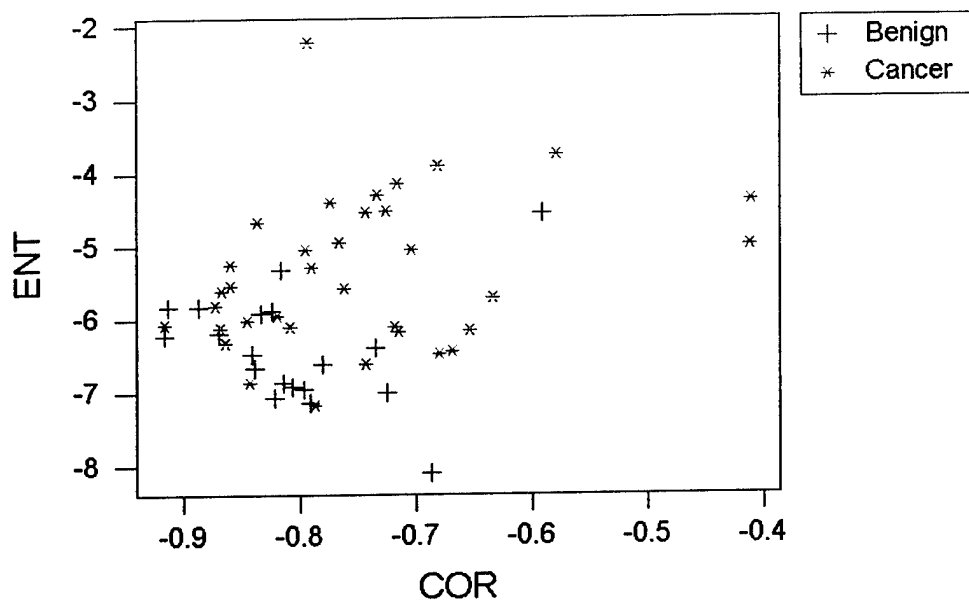


Figure 40: Scatter plot of the ENT and COR

Feature Combination	Performance $A_z \pm \text{s.d.}$
ENT SNR Intercept	0.8256 ± 0.0612
ENT SNR Slope	0.8541 ± 0.0542
ENT SNR Midband	0.7814 ± 0.0628
ENT SNR CON	0.8015 ± 0.0623
ENT Intercept Midband	0.7937 ± 0.0695
ENT Intercept COR	0.7908 ± 0.0646
ENT Intercept CON	0.7796 ± 0.0679
ENT Slope Midband	0.7755 ± 0.0713
ENT Slope COR	0.8144 ± 0.0604
ENT Slope CON	0.7926 ± 0.0693
ENT Midband COR	0.7444 ± 0.0693
ENT Midband CON	0.7476 ± 0.0677
ENT COR CON	0.8071 ± 0.0586

Table 13: Performance of the three-feature combinations

The performance of all the three-feature combinations was shown in Table 13. There are only two three-feature combinations that provided classification performance of $A_z \geq 0.82$. The combination of ENT, SNR and slope provides the best classification performance among three-feature combinations, which is 0.85 ± 0.05 . Notice that this combination also has the largest Mahalanobis distance (Table 11). The scatter plots of the two best three-feature combinations are also shown in Figure 42 and Figure 43 separately.

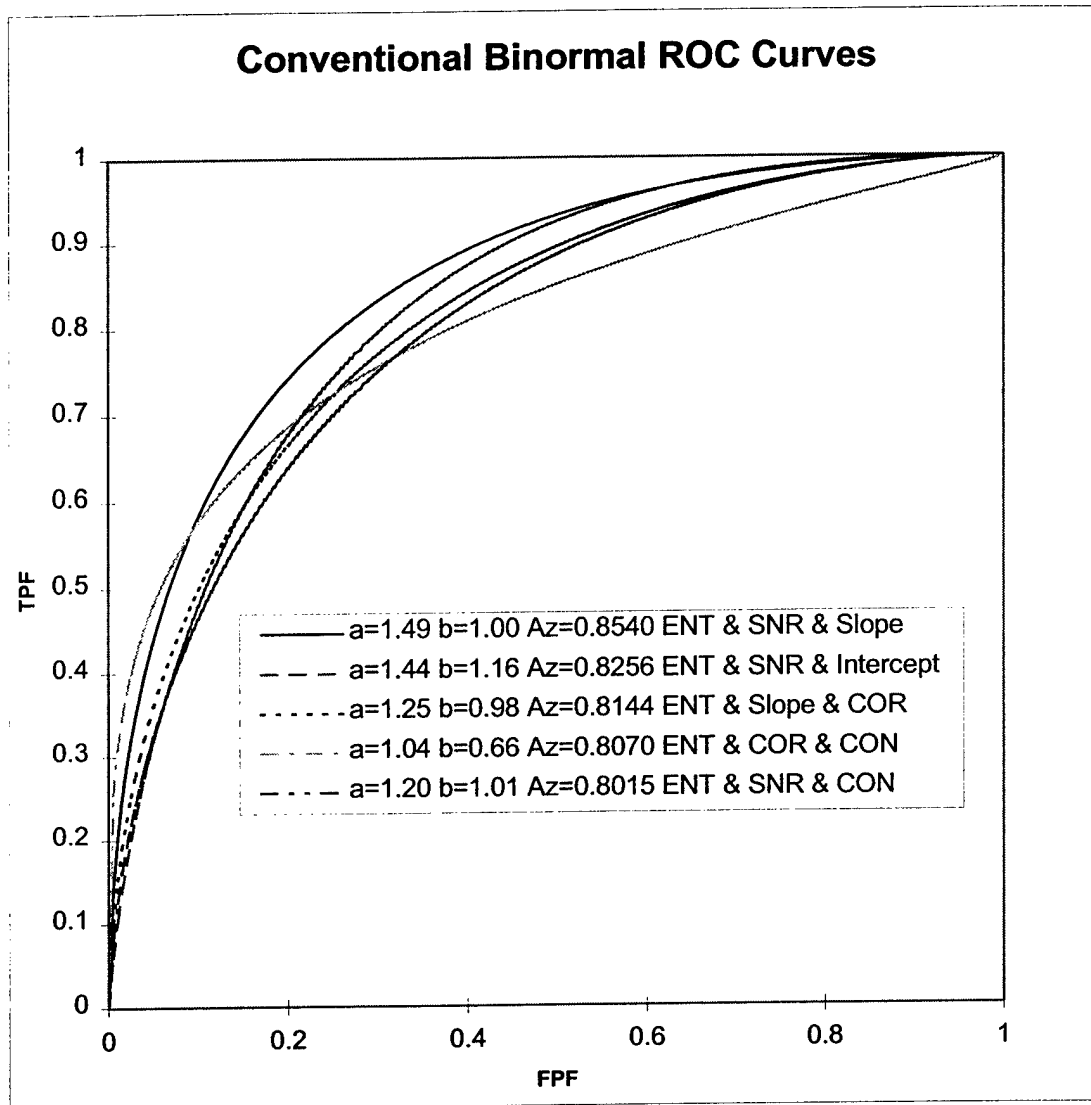


Figure 41: ROC curves of three-feature combination

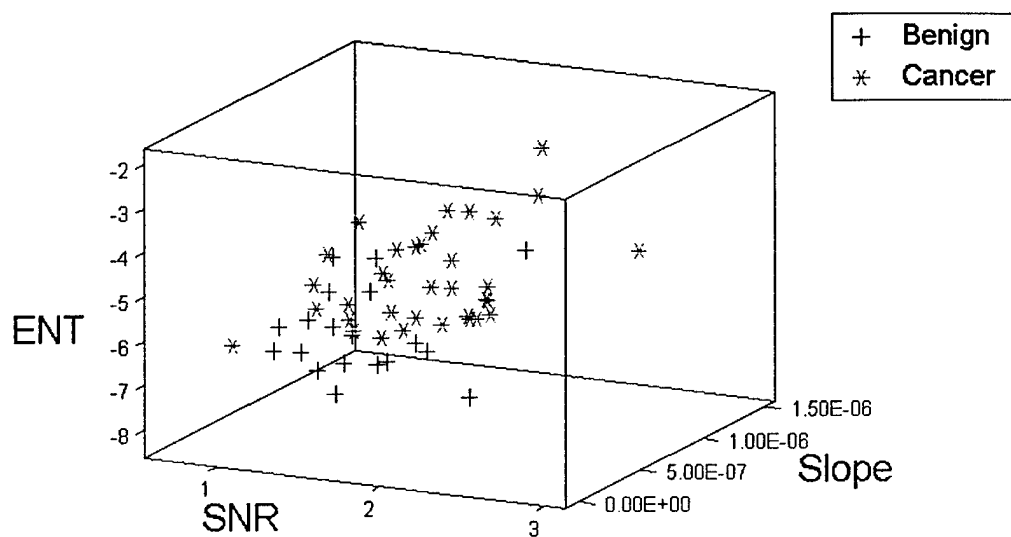


Figure 42: 3D scatter plot of ENT, SNR and slope

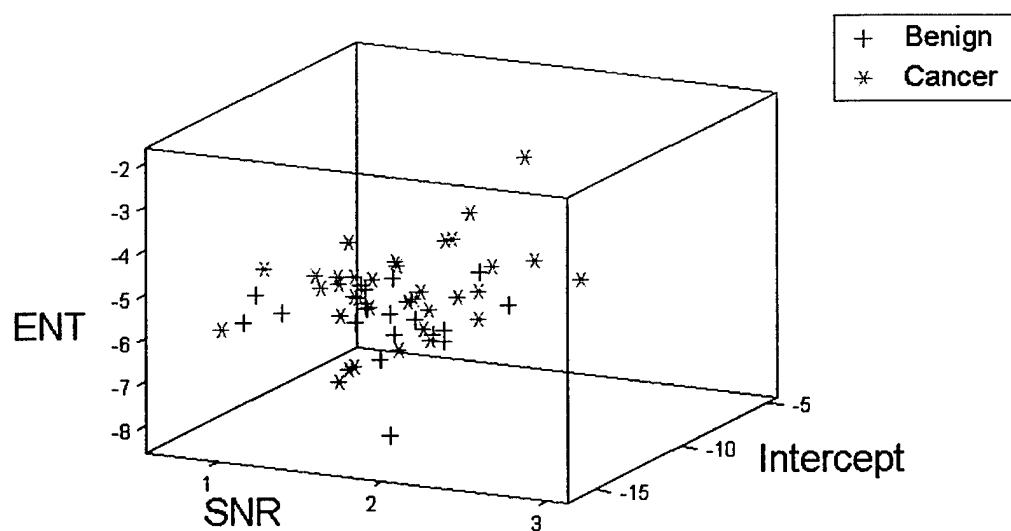


Figure 43: 3D scatter plot of ENT, SNR and intercept

5.5 Parametric Image

In addition to the development of algorithms for the computation of features from a user defined region of interest, some effort has been directed at developing software to automatically calculate features from multiple regions of interest over an entire RF data set (image) in order to produce a parametric image for each slice corresponding to the B-mode image. A preliminary version of the software has been completed and some initial parametric images have been produced (Figure 44).

When we choose the size of the region of interest (ROI), there will be the classical fundamental trade-off between resolution and sensitivity. That is, the small ROIs mean great resolution – but very great noise (no sensitivity). And large ROIs mean very good sensitivity, but very poor resolution. To generate the parametric image, we will scan the ROI throughout each image. This can be done in two ways:

(1) “Scroll” the ROI in an overlapping way – that is, analyze the first ROI starting from one corner; then move over some fraction of an ROI and analyze the new ROI – which will overlap the first one. Continue on until cover the whole image. The advantage is that it leads to nice parametric images.

(2) “Scroll” the ROI in a non-overlapping way. It is the same as above, but without overlapping. This will give independent ROIs. But the disadvantage is: if we want to make a parametric image of the results, it will be “blocky”.

In our situation, relatively large subregions must be used to reduce the variance of the calculated slope values and use of overlapping regions is a method of increasing the apparent spatial resolution of the image when larger subregions are necessary. After choosing the size of the ROI, it is possible to calculate the desired parameters for the ROI and to “scroll” the ROI in a specific overlapping or non-overlapping (0%

overlapping) way to cover the whole image to get a multi-dimensional parametric matrix. Then the parametric matrix is transferred into grayscale by adding an appropriate scaling factor and shown as a grayscale image. The images shown in Figure 44 demonstrate the higher level of detail afforded by using overlapping sub-regions.

The intend is to display parametric images during the development process to confirm proper operation of the software. However, in the end, the parametric data set will be combined with elastographic and clinical probability data to produce a single image in which overall probability of cancer (based on all features) is displayed for clinical use. It is likely that the experience gained in producing these intermediate parametric images will help to better display the final result – a parametric image where cancer probability is the parameter.

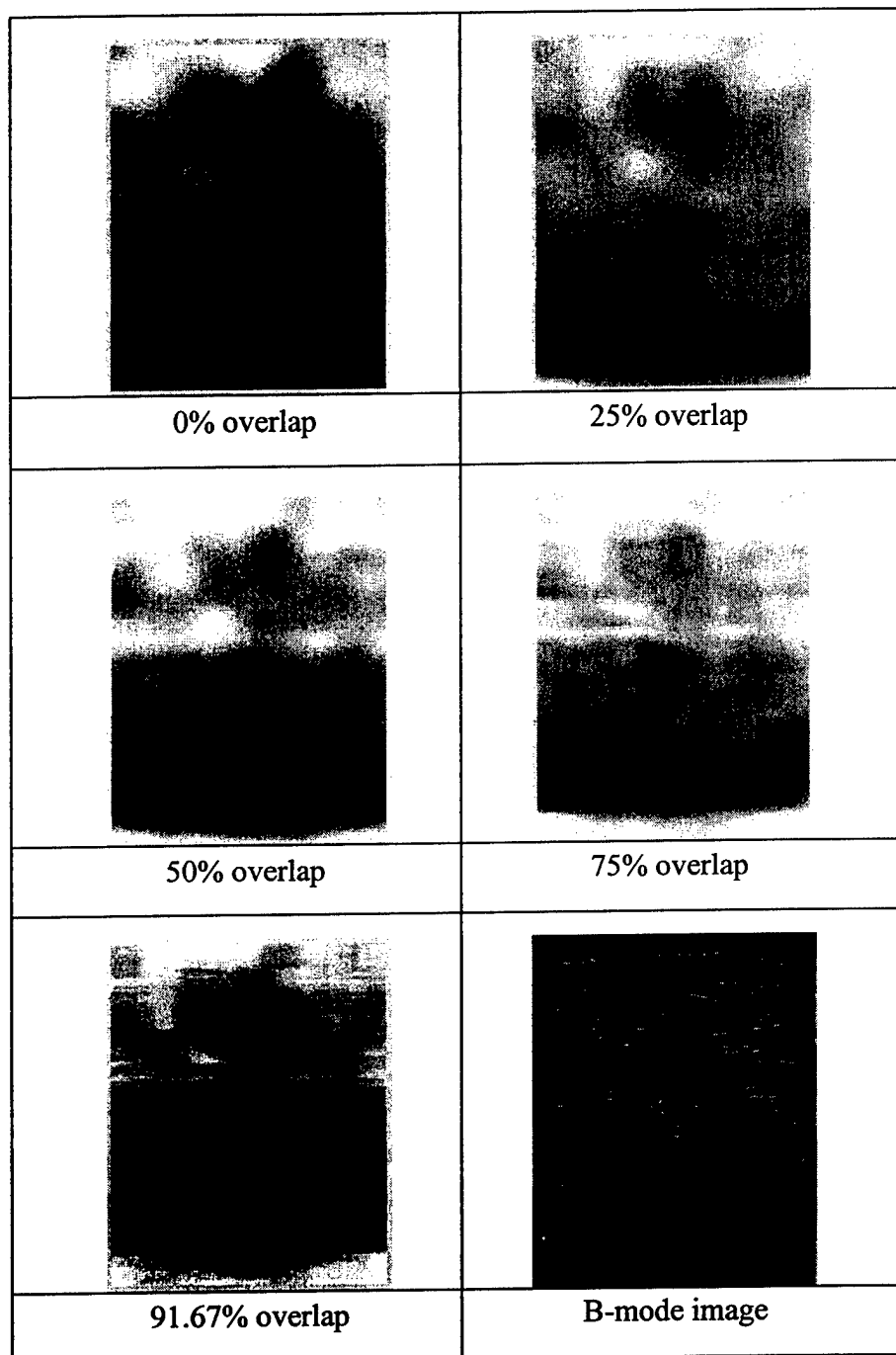


Figure 44: Parametric image of the prostate (case 48, slice 11) using backscatter slope feature with 5 mm x 12 RF vector regions of interest (ROI) with various degrees of overlap of the regions of interest.

Chapter 6 Conclusions

6.1 Summary

This research is part of the project “Combining Clinical, Sonographic, and Elastographic Features to Improve the Detection of Prostate Cancer” (Award Number: DAMD 17-99-1-1007) and focused on the study of quantitative sonographic tissue characterization.

First, the features that will be used to help distinguish cancers from benign tissue are selected. RF based and texture features are chosen because they stand for the microscopic and macroscopic tissue architecture information respectively.

Also, the software for computation of ultrasound based tissue features has been developed. The software allows the user to locate cancers on ultrasound images by comparison with corresponding pathology slices. With the help of this tool, the ROIs are marked and the position information of each ROI is stored in the database. This is an interactive process. Then the texture and RF features are calculated for the ROI (cancer or benign) and the results are saved in database.

Signal to noise ratios have also been calculated for the tissue mimicking phantom. It should exhibit a μ/σ value very close to 1.91. Our result demonstrates that sub-regions calculated from within the phantom do in fact exhibit a μ/σ close to 1.91. The average value is 1.893.

Then the next step is to search for the best individual and best combinations of features for discriminating cancerous from noncancerous tissue based on ROC analysis. Our results show that the best individual feature is entropy. The best two-

feature combination is entropy and correlation. And the best three-feature combination is entropy, slope and signal to noise ratio. The classification performance is 0.84 ± 0.06 and 0.85 ± 0.05 (area under receiver operating characteristic curve) respectively. The preliminary results show RF and envelope-detected signal analyses are diagnostically useful to discriminate prostate tissue.

6.2 Possible Future Work

In the future, this research can be extended in several different directions. First, much more data is needed to enhance the robustness of the techniques and the estimation of their performance. Next, exploration of different features might prove to be more successful. Elastography results and PSA information will be incorporated in the software. It would be interesting to explore the ability of more complex classifiers (such as quadratic, k-nearest neighbor, and neural network classifiers) of distinguishing normal tissues from cases of prostate cancer.

One improvement can be made by using a constant size of ROI to eliminate bias in statistical features due to ROI size. Because the larger ROI sizes lead to a reduction in measured variance. One example is shown in Table 16. It may have affected the clinical results since the size of cancer ROIs tended to be small and that of benign ROIs tended to be larger. The solution to this problem is to divide the larger ROI into several sub-regions and then average the results.

And the possibility would be to scan the prostate specimens with curved array and to develop a classifier for that data.

References

- Bourke, P. (2001), "Distributions," <http://astronomy.swin.edu.au/pbourke/analysis/distributions/>, URL valid as of Sep., 17, 2001.
- CaP (2001), Prostate Cancer Definition, <http://www.cancer-prostate.com/DefinitionsFrame1Source1.thm>, URL valid as of June 12, 2001.
- Feleppa, E.J., Kalisz, A., Sokil-Melgar, J.B., Lizzi, F.L., Liu, T., Rosado, A.L., Shao, M.C., Fair, W.R., Wang, Y., Cookson, M.S., Reuter, V.E., Heston, W.D.W. (1996), "Typing of Prostate Tissue by Ultrasonic Spectrum Analysis," *IEEE Transactions on Ultrasonics, Ferroelectrics, and Frequency Control*, Vol. 43, No.4, pp. 609-619.
- Feleppa, E.J., et al. (1997), "Ultrasonic spectral-parameter imaging of the prostate," *Int. J. of Imaging Syst. & Technol* 8, 11-25.
- Feleppa, E.J., et al. (2001), "Application of spectrum-analysis and neural-network-based imaging to detection and treatment of prostate cancer," *International Symposium on Ultrasonic Imaging and Tissue Characterization 26th*.
- Frederick, E.D. (2000), "Computer Aided Diagnosis of Acute Pulmonary Embolism," A dissertation of Duke University
- Garra, B.S., Insana, M.F. (1989), "Quantitative ultrasonic detection and classification of diffuse liver disease: comparison with human observer performance," *Investigative Radiology* 24:196-203.
- Garra, B.S., Krasner, B.H., Horii, S.C., Ascher S., Mun, S.K., Zeman, R.K. (1993), "Improving the Distinction Between Benign and Malignant Breast Lesions: The Value of Sonographic Texture Analysis," *Ultrasonic Imaging* 15, 267-285.
- Garra, B.S., Insana, M.F. (1994), "Quantitative ultrasonic detection of parenchymal structural change in diffuse renal disease," *Investigative Radiology* 29:134-140.
- Garra, B.S. (1998), "Combining Clinical, Sonographic, and Elastographic Features to Improve The Detection of Prostate Cancer," Revised Statement of Work.
- Garra, B.S. (2000), "Combining Clinical, Sonographic, and Elastographic Features to Improve the Detection of Prostate Cancer," Annual Report of University of Vermont and State Agricultural College.

Hahn, G.J., Shapiro, S.S. (1967), "Statistical Models in Engineering," John Wiley & Sons, Inc., New York.

Huynen, A.L., Giesen, RJB. (1994), "Analysis of ultrasonographic prostate images for the detection of prostatic carcinoma: the automated urologic diagnostic expert system," *Ultrasound Med. Biol.* 20:1-10.

Insana, M.F., Garra, B.S., Brown, D.G., Shawker, T.H. (1986), "Analysis of Ultrasound Image Texture via Generalized Rician Statistics," *Optical Engineering*, Vol. 25, No. 6, pp. 743-748.

Lachenbruch, P.A., Mickey, M.R. (1968), "Estimation of error rates in discriminant analysis," *Technometrics* 10, 1-11.

Lerski, R.A. (1988), "Practical Ultrasound," Oxford University Press, Washington DC.

Lizzi, F.L., Ostromogilsky, M., Feleppa, E.J., Rorke, M.C., Yaremko, M.M. (1986), "Relationship of Ultrasonic Spectral Parameters to Features of Tissue Microstructure," *IEEE Transactions on Ultrasonics. Ferroelectrics. and Frequency Control*. Vol. UFFC-34. No. 3.

MATLAB Online Help (2000), MathWorks, Inc.

Metz, C.E. (1998), ROCKIT Users Guide.

Mia, R.S. (1999), "Classification Performance and Reproducibility of New Parameters for Quantitative Ultrasound Tissue Characterization," A dissertation of Johns Hopkins University.

Minitab User's Guide (1997), Minitab, Inc.

Mohanty, Nirode. (1987), "Signal Processing," Van Nostrand Reinhold Company Inc., New York.

NCSU (2001), Medical Ultrasound Figure,
<http://www5.bae.ncsu.edu/bae/research/blanchard/www/465/textbook/imaging/projects/ultrasound/project/drawing.html>, URL valid as of August 20, 2001.

PROACT (2001), The PSA Test,
<http://www.prostateaction.org/articles/psatesthowdoesitwork.html>, URL valid as of June 12, 2001.

Prostate (2001), Introduction to Prostate Cancer,

<http://website.lineone.net/~prostate/intro.html>, URL valid as of June 12, 2001.

ROC (2001), Handbook of Medical Informatics

http://www.mieur.nl/mihandbook/r_3_3/booktext/booktext_15_04_01_02o.htm, URL valid as of August 20, 2001.

Trochim, W.M. (2001), Research Methods Knowledge Base,

<http://trochim.human.cornell.edu/kb/statsimp.htm>, URL valid as of August 20, 2001.

Wagner, R.F., Smith, S.W., Sandrik, J.M., Lopez, H. (1983), "Statistics of Speckle in Ultrasound B-Scans," *IEEE Transactions on Sonics and Ultrasonics*, Vol. 30, No. 3, pp. 156-163.

Wagner, R.F., et al. (1986), "Analysis of ultrasound image texture via generalized Rician statistics," *Optical Engineering*, Vol.25, No.6, pp. 743-748.

Wagner, R.F., et al. (1987), "Statistical properties of radio-frequency and envelope-detected signals with applications to medical ultrasound," *Optical Society of America*, Vol.4, No. 5, pp. 910-922.

Wear, K.A., Garra, B.S., Hall, T.J. (1995), "Measurements of ultrasonic backscatter coefficients in human liver and kidney in vivo," *Acoustical Society of America*, Vol. 98, No. 4, pp. 1852-1857.

Appendix A: Database Structure

Field Name	Data Type
PatientID	Number
USFileName	Number
USFileNumber	Number
PATHFileName	Number
PATHFileNumber	Number
Phantom	Number
StartingDepth	Number
StoppingDepth	Number

Table 14: Table structure – patient

Field Name	Data Type
Status	Number
USSliceFileName	Number
ROINum	Number
ROICharacter	Text
ROI X	Number
ROI Y	Number
ROIWidth	Number
ROIHeight	Number

Table 15: Table structure – roiInf

Appendix B: Flowchart of GUI Usage

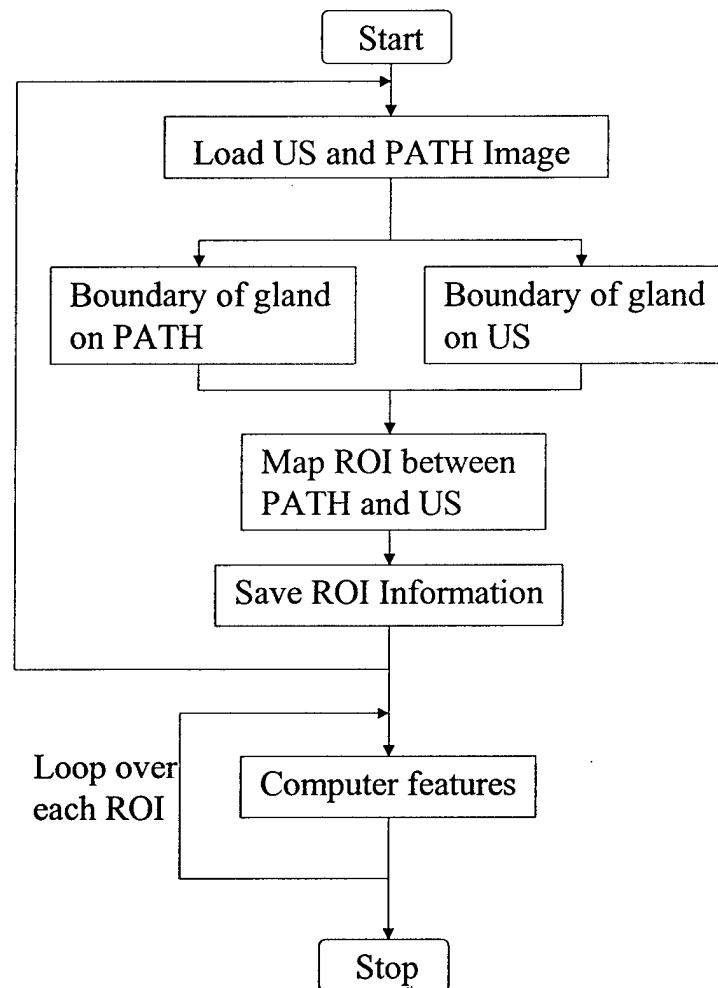


Figure 45: Flowchart of GUI usage

Appendix C: Bias Caused by ROI Size

To demonstrate the bias introduced by ROI size, SNR is calculated for different sizes of ROIs. There are 12 ROIs in each size. Notice that the larger ROIs contain the smaller ones. The result shows that the larger ROI has lower variance.

ROI Size	S.D.
20x25	0.250
30x38	0.132
35x44	0.096
40x50	0.085
45x56	0.084

Table 16: Bias caused by ROI size

Appendix D: Backscatter Coefficient of Reference Phantom

Frequency (Hz)	Backscatter Coefficient
3.125000e06	2.1612715E-04
3.222656e06	2.4848658E-04
3.320313e06	2.7688060E-04
3.417969e06	3.0678869E-04
3.515625e06	3.5969596E-04
3.613281e06	4.3010002E-04
3.710938e06	4.2878010E-04
3.808594e06	4.7800399E-04
3.906250e06	6.4783212E-04
4.003906e06	5.2049971E-04
4.101563e06	7.9972047E-04
4.199219e06	6.8410835E-04
4.296875e06	7.8617007E-04
4.394531e06	1.0446353E-03
4.492188e06	9.0188358E-04
4.589844e06	1.3031829E-03
4.687500e06	1.2099128E-03
4.785156e06	1.1688722E-03
4.882813e06	1.4217630E-03
4.980469e06	1.2657929E-03
5.078125e06	1.5340993E-03
5.175781e06	1.6429626E-03
5.273438e06	1.6357866E-03
5.371094e06	2.2317523E-03
5.468750e06	2.0040637E-03
5.566406e06	2.0739918E-03
5.664063e06	2.3677654E-03
5.761719e06	2.2838814E-03
5.859375e06	2.6224537E-03
5.957031e06	2.8915587E-03
6.054688e06	3.0219131E-03
6.152344e06	3.4578224E-03
6.250000e06	3.2285405E-03
6.347656e06	3.4586722E-03
6.445313e06	4.0386640E-03
6.542969e06	3.9208517E-03
6.640625e06	3.9382731E-03
6.738281e06	4.0659769E-03
6.835938e06	3.9548110E-03
6.933594e06	4.0240278E-03
7.031250e06	4.4389609E-03

Appendix E: Phase Shifting with the Hilbert Transform

$$h(t) = \frac{1}{\pi t}$$

$$H(f) = -j \operatorname{sgn}(f) \quad \text{where} \quad \operatorname{sgn}(f) = \begin{cases} -1, & f < 0 \\ 0, & f = 0 \\ 1, & f > 0 \end{cases}$$

A. A cosine was transformed into a sine:

$$x_1(t) = \cos w_0 t$$

$$\hat{x}_1(t) = x_1(t) \otimes h(t) \Leftrightarrow \hat{X}_1(f) = X_1(f)H(f)$$

$$\hat{X}_1(f) = \pi(\delta(2\pi f - w_0) + \delta(2\pi f + w_0))H(f)$$

$$= \pi(-j\delta(2\pi f - w_0) + j\delta(2\pi f + w_0))$$

$$= \pi j(\delta(2\pi f + w_0) - \delta(2\pi f - w_0))$$

$$= \frac{\pi}{j}(\delta(2\pi f - w_0) - \delta(2\pi f + w_0)) \Leftrightarrow \hat{x}_1(t) = \sin w_0 t$$

B. A sine was transformed into a minus cosine:

$$x_2(t) = \sin w_0 t$$

$$\hat{x}_2(t) = x_2(t) \otimes h(t) \Leftrightarrow \hat{X}_2(f) = X_2(f)H(f)$$

$$\hat{X}_2(f) = \frac{\pi}{j}(\delta(2\pi f - w_0) - \delta(2\pi f + w_0))H(f)$$

$$= \frac{\pi}{j}(-j\delta(2\pi f - w_0) - j\delta(2\pi f + w_0))$$

$$= -\pi(\delta(2\pi f + w_0) + \delta(2\pi f - w_0)) \Leftrightarrow \hat{x}_2(t) = -\cos w_0(t)$$